Title

Engineering Nanoscale Multiferroic Composites for Memory Applications with Atomic Layer Deposition of Pb(ZrxTi1-x)O3 Thin Films

Author

Chien, Diana

Publication Date

2016

Peer reviewed|Thesis/dissertation

UNIVERSITY OF CALIFORNIA

Los Angeles

Engineering Nanoscale Multiferroic Composites for Memory Applications with Atomic Layer Deposition of $Pb(Zr_xTi_{1-x})O_3$ Thin Films

A dissertation submitted in partial satisfaction of the

requirements for the degree Doctor of Philosophy

in Chemical Engineering

by

Diana Chien

2016

ABSTRACT OF THE DISSERTATION

Engineering Nanoscale Multiferroic Composites for Memory Applications with Atomic Layer Deposition of $Pb(Zr_xTi_{1-x})O_3$ Thin Films

by

Diana Chien

Doctor of Philosophy in Chemical Engineering

University of California, Los Angeles, 2016

Professor Jane Pie-Chen Chang, Chair

This work focuses on the development of atomic layer deposition (ALD) for lead zirconate titanate, $Pb(Zr_xTi_{1-x})O_3$ (PZT). Leveraging the surface-reaction controlled process based on alternating self-limiting surface reactions, PZT can be synthesized not only with elemental precision to realize the desired composition (Zr/Ti = 52/48) but also with outstanding conformality. The latter enables the integration of PZT with a ferromagnetic phase to realize multiferroism (MF) and magnetoelectric (ME) effect. Since PZT is one of the best known ferroelectric and piezoelectric materials due the large displacements of the Pb ions at the morphotropic phase boundary, PZT based MF composites could lead to stronger ME coupling through strain coupling at the interface.

Specifically, ALD PZT thin films were synthesized by using beta-diketonate metalorganic precursors $Pb(TMHD)_2$, $Zr(TMHD)_4$, and $Ti(O^{\cdot}i\text{-}Pr)_2(TMHD)_2$ and H_2O. The number of local cycles and global cycles were regulated to achieve the desired stoichiometry and thickness, respectively. ALD of PZT was studied to obtain (100) textured PZT on Pt (111) oriented platinized silicon substrates. In order to attain a highly oriented PZT thin film, a (100) textured $PbTiO_3$ seed layer was required because PZT orientation is governed by nucleation.

MF nanocomposites were engineered using ALD PZT thin films to achieve controlled complex nanoscale structures, enabling porosity to be studied as a new additional parameter for nancomposite architectures to enhance ME effect. Specifically, 3-6 nm-thick ALD PZT thin films were deposited to uniformly coat the walls of mesoporous cobalt ferrite (CFO) template. The PZT/CFO nanocomposites were electrically poled *ex-situ* and the change in magnetic moment was measured. The inverse magnetoelectric coupling coefficient, α, was determined to be 85.6 Oe-cm/mV. The in-plane results show no significant change in magnetization (1–4%) as a function of electric field, which was expected due to the effect of substrate clamping. The out-of-plane magnetization showed that the mesoporous CFO coated with 3-nm-thick PZT film had a greater saturation magnetization change of 15% compared to 10% for the 6-nm-thick PZT film. This indicates that the flexibility in the partially filled pores enhances the ME coupling.

Additionally, ALD PZT films were integrated between MgO and CoFeB layers to fabricate magnetic tunnel junctions (MTJ), which was the first work to demonstrate increased voltage controlled magnetic anisotropy (VCMA) effect in a complete MTJ stack using a high dielectric material within the tunnel barrier and exhibit sizeable tunneling magnetoresistance (TMR) at room temperature. The fabricated PZT MTJs with the MgO/PZT/MgO barrier demonstrated a VCMA coefficient which is ~40% higher (20 fJ/V-m) than MgO MTJs (14 fJ/V-m) and TMR of more than 50% at room temperature, comparable to that of the MgO MTJs. The enhanced VCMA coefficient and sizeable TMR makes PZT MTJs potential candidates for future voltage-controlled, ultralow-power magnetic random access memory devices.

ALD enables the growth of conformal ultra-thin PZT films, which can then be integrated to engineer nanoscale multiferroic composites for various applications.

The dissertation of Diana Chien is approved.

Gregory P. Carman

Selim M. Senkan

Jane Pei-Chen Chang, Committee Chair

University of California, Los Angeles

2016

TABLE OF CONTENTS

LIST OF FIGURES

LIST OF TABLES

ACKNOWLEDGEMENTS

This work and my last five and a half years in the UCLA Chemical Engineering Ph.D. program would not have been possible without the input, support, and caring from countless numbers of people. Unfortunately, although I have tried to include as many people as I could, I will have inevitably left out some people who also deserve to be thanked for which I apologize for not mentioning.

I would first like to thank my newly-wedded husband, Gary Alexander Jury, for the immense support and love he has provided for me. He has been there for me physically, emotionally, and psychologically throughout the most intense, rigorous, roller-coaster, once-in-a-lifetime of an experience, and I absolutely could not have done this without him. No amount of thank you will ever be enough. Also, I would like to acknowledge my families – my Mommy (Judy Chien), my Baba (Jimmy Chien), my brother (Ronald Chien), my sister (Joanna Chien), my Mom (Linda Jury), my Dad (Phil Jury), and my older brothers (Paul and Mark Jury). I could not have done it without you too. A very special thank you to my Mommy and my Baba for all the prayers on my behalf, and to my Dad, Phil Jury, for all the phone calls with great advice about dealing with all the nuances of graduate school.

Next, I would like to thank my doctorate advisor, Professor Jane P. Chang for taking a chance on me and giving me the wonderful opportunity of conducting research in her lab and under TANMS. Her wisdom, professionalism, academic intelligence, and strength are attributes I greatly admire and I hope to model myself after her throughout my professional career. I have learned a lot from her – both in terms of research and personal growth – and have been very fortunate to have her as my advisor. I would also like to thank my dissertation committee,

Professors Greg Carman, Selim Senkan, Tatiana Segura, and Dante Simonetti for their time and imput as well as the funding support from TANMS center which was funded by NSF.

I must thank my collaborators for all the meetings, brain-storming sessions, invaluable discussions, and late nights. Thank you Abraham Buditama, Xiang Li, Pedram Khalili, Scott Keller, Juan Alzate, Guoqiang Yu, Kin Wong, Shauna Robbennolt, Sam Goljahi, Paul Nordeen, Wei Sun, Laura Schelhas, Professor Sarah Tolbert, Professor Kang Wang, Professor Chris Lynch, and other fellow grad students – I could not have done it without you. And helping or teaching me to do various analytical techniques: Doctor Ignacio Martini, Adam Stieg, Mark Zurbuchen, Tom Mates, Noah Bodzin, Wilson Lin, and Sergey Prikhodko. I must also thank Addis Fuhr and Professor Yunfeng Lu from the Chemical and Biomolecular Engineering Department at UCLA for their help and usage of the Microwave Annealing Machine, thanks to Professor Yuanbing Mao in Department of Chemistry at University of Texas – Pan American for his collaboration on the PZT/LNMO and PZT/LCMO nanoparticles research work, and thanks to Professor Susan Trolier-McKinstry in the Materials Research Laboratory at The Pennsylvania State University for her advice and suggestions on synthesizing PZT thin films and help with the wafer flexure technique.

My fellow chemical engineering graduate school companions also deserve mention for their camaraderie over the past five plus years, but I should give special thanks to Allison Yorita, Jennifer Takasumi, Paul Lin, Larry Gao, Michael Nayhouse, Calvin Pham, and countless others for their continued friendship. Also, a very special thanks to Nancy Lin and James Dorman for helping me realize my research interest. My non-UCLA friends who have helped me through this journey and kept me in check also need to be thanked, especially Anna Milcarek, Ally Cao, Dara Epstein, Penny Ishizuka, Kasey Shuda, Hailey Bright, Jenn Brazil, Mark Andre,

Laura Steinmetz, Michelle Drinkmann, and Betsy Lee. I also need to thank UCLA CAPS, specifically Patricia Rodriguez and Doctor Anupuma Kalsi for their advice and help throughout my Ph.D. career.

The members of the Chang Lab group, both past and present, must also be thanked here for their collaboration and input. I must thank Sandy Perng and Dr. Taeseung Kim for their guidance. I would also like to thank my successor Kevin Fitzell for being incredibly helpful with experimental work and my thesis appendix. In addition, the other members of the lab which I have had the privilege of working with and knowing: the former and current grad students Wilson Lin, James Dorman, Sandy Perng, Nathan Marchack, Vladan Jankovic, Calvin Pham, Jay Cho, Jack Chen, Colin Rementer, Cyrus Cheung, Trevor Seegmiller, Jeffrey Chang, Nicholas Altieri, Luke Minardi, Kevin Fitzell, Ernest Chen, and Ryan Sheil; the post-doctorate researchers Doctors Ju Hyeon Choi, Taeseung Kim, and Younghee Kim, and the undergraduate or high school researchers Juan Carlos Casillas Plazola and Caroline Yaeger.

Thank you to all for the love and support that you gave me while I was at UCLA, and it would not have been possible for me to come this far without any of you.

VITA

2006	B.A., Engineering Brown University Providence, RI
2006-2008	Middle and High School Science Teacher Milken Community High School Los Angeles, CA
2008-2009	Associate Instrumentation Engineer WorleyParsons Arcadia, CA
2008-2010	Co-Director and Tutor PJ TestPrep Los Angeles, CA
2010-2016	Ph.D. Candidate Graduate Student Researcher Department of Chemical and Biomolecular Engineering University of California, Los Angeles
Jan-March 2011, Sept-Dec 2011	Teaching Assistant Department of Chemical and Biomolecular Engineering University of California, Los Angeles

AWARDS

2015 Tech Forum Best in Exploring Fundamental Science Poster Prize, Feb 2015

Division of Engineering – Bachelor of Arts Outstanding Student Award, May 2006

PUBLICATIONS

Diana Chien*, Xiang Li*, Kin Wong, Shauna Robbennolt, Guoqiang Yu, Sarah Tolbert, Nicholas Kioussis, Pedram Khalili Amiri, Kang Wang, and Jane Chang, "Enhanced Voltage-Controlled Magnetic Anisotropy in Magnetoelectric Tunnel Junctions with a MgO/PZT/MgO Tunnel Barrier," *In process of writing*, (2015); * Denotes equal contributions

Diana Chien*, Abraham Buditama*, Laura Schelhas, Jane Chang, and Sarah Tolbert,"Magnetoelectric Effect in Multiferroic Nanocomposites of Atomic Layer Deposition $Pb(Zr,Ti)O_3$ Coupled with Templated Mesoporous $CoFe_2O_4$," *In process of writing*, (2015); * Denotes equal contributions

K. Liang, A. Buditama, D. Chien, J. Cui, P.L. Cheung, S. Goljahi, S.H. Tolbert, J.P. Chang, and C.S. Lynch, "The conductivity mechanism and an improved C-V model of ferroelectric PZT thin film," *Journal of Applied Physics*, 117 (2015)

Yoram Cohen, Nancy Lin, Kari J. Varin, Diana Chien, and Robert F. Hicks, "Chapter 5: Membrane Surface Nanostructuring with Terminally Anchored Polymer Chains," *Functional Nanostructured Materials and Membranes for Water Treatment*, Wiley-VCH (2013)

PRESENTATIONS

2015 MRS Fall Meeting
December 1, 2015
Oral Presentation - "Enhanced Voltage-Controlled Magnetic Anisotropy (VCMA) in Magnetic Tunnel Junctions with a MgO/PZT/MgO Tunnel Barrier"

AVS 62nd International Symposium & Exhibition
October 20, 2015
Oral Presentation - "Magnetoelectric Effect in Multiferroic Nanocomposites of Atomic Layer Deposition $Pb(Zr_xTi_{1-x})O_3$ Coupled with Templated Mesoporous $CoFe_2O_4$"

XXIV International Materials Research Congress
August 17, 2015
Oral Presentation - "Enhanced Voltage-Controlled Magnetic Anisotropy (VCMA) in Magnetic Tunnel Junctions with a MgO/PZT/MgO Tunnel Barrier"

Symposium Session Chair – "Symposia 6I: Multiferroic Materials Systems and Multilayer Ferroic Heterostructures: Experiment, Theory, Properties, and Applications"

Center for Translational Applications of Nanoscale Multiferroic Systems (TANMS)
Feb 6, 2015
Oral Presentation - "Atomic Layer Deposition of PZT Thin Films to Engineer Nanoscale Composites for Memory and Multiferroic Applications"

UCLA Engineering Tech Forum
Feb 2, 2015
Poster - "Atomic Layer Deposition of PZT Thin Films to Engineer Nanoscale Composites for Memory and Multiferroic Applications"

AVS 61th International Symposium & Exhibition
Nov 11, 2014
Oral Presentation - "Atomic Layer Deposition of $Pb(Zr_xTi_{1-x})O_3$ Thin Films to Engineer Nanoscale Multiferroic Composites"

CHAPTER 1. INTRODUCTION

1.1 Motivation

Computer technology has made incredible progress since the first general-purpose electronic computer was created in 1946. With rapid advances in technology and innovations for building and designing computers, access to mobile computers have become ubiquitous in our society. However, one of the major challenges is the processor-memory gap, as shown in Figure 1-1 (Hennessy, Patterson et al. 2003).

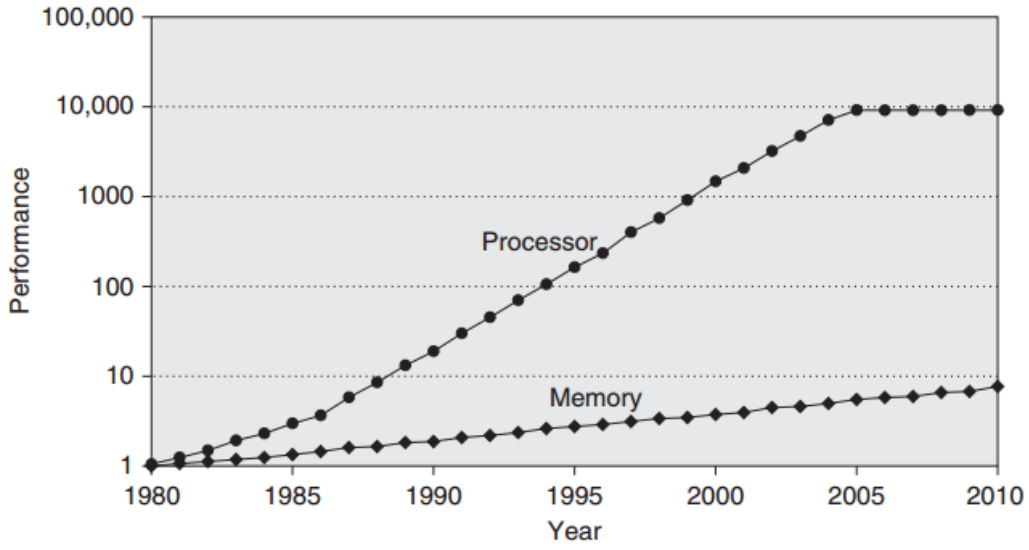

Figure 1-1. Starting with 1980 performance as a baseline, the gap in performance, measured as the difference in the time between processor memory requests (for a single process or core) and the latency of a DRAM access, is plotted over time (Hennessy, Patterson et al. 2003).

Traditionally, a memory hierarchy has been effectively used in order to keep up with the processor while balancing price and performance. It is organized into three major levels, where SRAM is used for on-chip cache memory, DRAM is used for main memory, and Flash and hard disk drives are used for mass storage (Fink 2014), as shown in Figure 1-2.

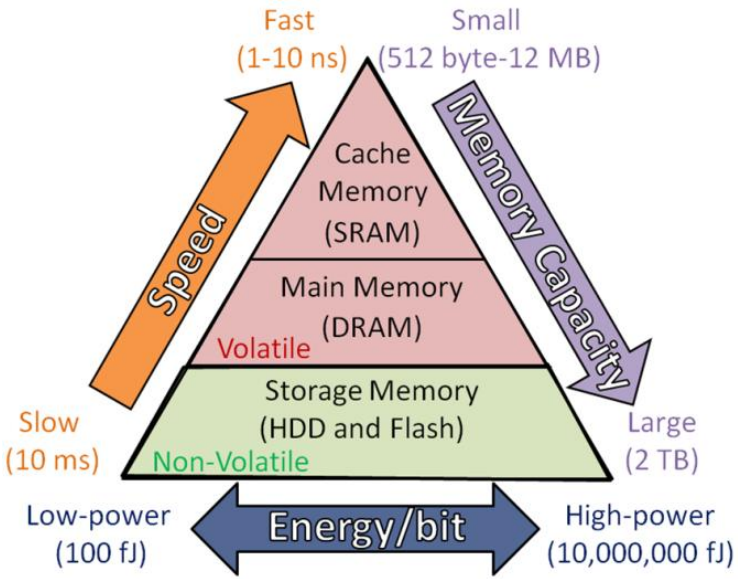

Figure 1-2. Memory hierarchy where different technologies are used to achieve specific tasks in computing systems depending on required speed, memory capacity, and energy per bit (AVNET 1999; Fink 2014).

As one moves down the hierarchy levels, the memory and storage devices reduce in performance and cost, but tend to rise in capacity (AVNET 1999). However, memory power consumption loss has become a major problem recently. For example, volatile memory devices need to be consuming power continuously (Fink 2014). In some cases, the memory caches can account for 25-50% of the total power consumption (Hennessy, Patterson et al. 2003). Therefore, the memory hierarchy is far from an ideal solution and an alternative memory is needed in order to progress computer technology. As a result, new types of memory devices are being developed in hope to create a single "universal memory" that is low-power switching, non-volatile, has high read/write speed, large memory capacity, and is scalable to nanometer-size, cheap, and durable. The most promising candidate is a form of magnetic memory called magnetoelectric random access memory, MeRAM, as shown in Table 1-1 (Khalili and Wang 2015).

Table 1-1. Comparison of existing non-spintronic and emerging spintronic memory technologies, highlighting STT-RAM (current-induced switching) and MeRAM (voltage-controlled switching) (Tang and Lee 2010; Wang, Alzate et al. 2013).

	Production Processes				In Development	
Technology	SRAM	DRAM	NAND Flash	FeRAM	STT-MRAM	MeRAM
Energy/bit (fJ)	100	1000	10^7	54	100	< 10
Write Speed (ns)	1	20	100,000	50	1 – 10	1 – 10
Read Speed (ns)	1	30	10,000	20-80	1 – 10	1 – 10
Density (area in F^2)	>30	6-10	2 – 4	15-35	20 – 40	2 – 8
Endurance (Cycles)	$>10^{16}$	$>10^{16}$	10^5	$10^{9\text{-}12}$	10^{15}	10^{15}
Non-volatile	No	No	Yes	Yes	Yes	Yes
Standby power	Leakage Current	Refresh Current	None	None	None	None

The minimum energy barrier that needs to be overcome to write a magnetic bit is 0.17 aJ, which is calculated from $E_b = 40\ k_BT$, where k_B is the Boltzmann constant (1.38×10^{-23} J/K) and T is the operating temperature (room temperature of 300 K). However, as can been seen in Table 1-1, the current memory technologies generally use 50-1000 fJ of energy per bit, which is a highly inefficient process. The limitation in energy efficiency is a fundamental issue – since the memory devices are current-driven, the energy is lost in the form of heat dissipation. As the memory bits are scaled to smaller dimensions, there would be more power loss due to an increase in resistance. In addition, there would be less memory capacity due to an increase in aerial density as a transistor is needed to drive the current through each memory bit (Khalili and Wang 2015). Therefore, the limitations can be avoided by designing a memory device that uses voltage or electric-field (instead of current) to control the magnetization in the bits. MeRAM enables devices to be ultra-low power (as low as 10-100 aJ/bit), scalable down to nanometer-size dimensions with increasing memory capacity (Khalili Amiri, Alzate et al. 2015). In order to develop MeRAMs, a group of materials called multiferroic materials is showing promise.

Therefore, there is a large interest in synthesizing and integrating multiferroic materials that possesses a strong ferroelectric and ferromagnetic coupling in order to control the magnetization by an electric field or the polarization by a magnetic field at room temperature for the next-generation memory applications (Martin, Chu et al. 2010).

1.2 Multiferroic Materials

The advent of the magnetoelectric effect and multiferroics field began in 1894 when Pierre Curie proposed a strong coupling between magnetic and electric energies and Debye coined the term "magnetoelectric" a few years later (Fiebig 2005). In 1959, Landau and Lifshitz predicted a linear coupling between electric polarization and magnetization and Dzyaloshinskii and Astrov were the first to experimentally observe the linear magnetoelectric effect in chromium oxide, Cr_2O_3 (Astrov 1961). However, the field slowed down in the 1970s when the observed magnetoelectric effect was too weak for memory or switching device applications as the Curie and Néel temperature of most multiferroics was far below room temperature. Then, Schmid coined the term "multiferroics" in 1994 (Schmid 1994) and the field was revived in 2003 when Wang *et al.* observed the magnetoelectric effect in room-temperature multiferroic $BiFeO_3$ (Wang, Neaton et al. 2003), Kimura et al. discovered coexistence of magnetism and ferroelectricity in $TbMnO_3$ (Kimura, Goto et al. 2003), and Hur et al. found similar effect in $TbMn_2O_5$ (Hur, Park et al. 2004), as Spaldin had predicted (Spaldin and Fiebig 2005). With new experimental techniques to synthesize multiferroic materials and composites and theories to understand the magnetoelectric effect, a great interest in the multiferroics field has taken place, as evident in Figure 1-3 by the increase in number of research publications (Fiebig 2005).

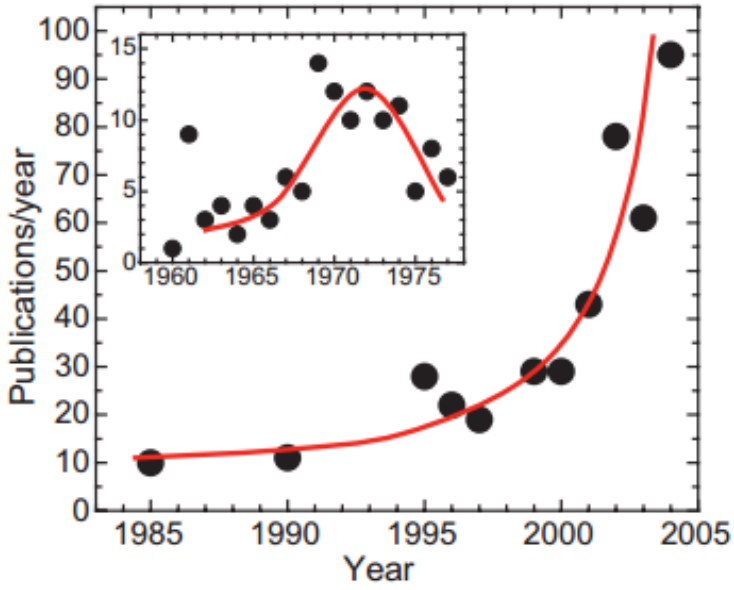

Figure 1-3. Publications per year with "magnetoelectric" as a keyword according to the *Web of Science* (Fiebig 2005).

Multiferroics is a subgroup of magnetoelectric materials that are able to be polarized both magnetically and electrically (Martin, Chu et al. 2010). Multiferroic materials possess at least two of the following properties: ferroelectricity, ferromagnetism, ferroelasticity, antiferroelectricity, and antiferromagnetism, as shown in Figure 1-4 (Eerenstein, Mathur et al. 2006; Martin, Chu et al. 2010).

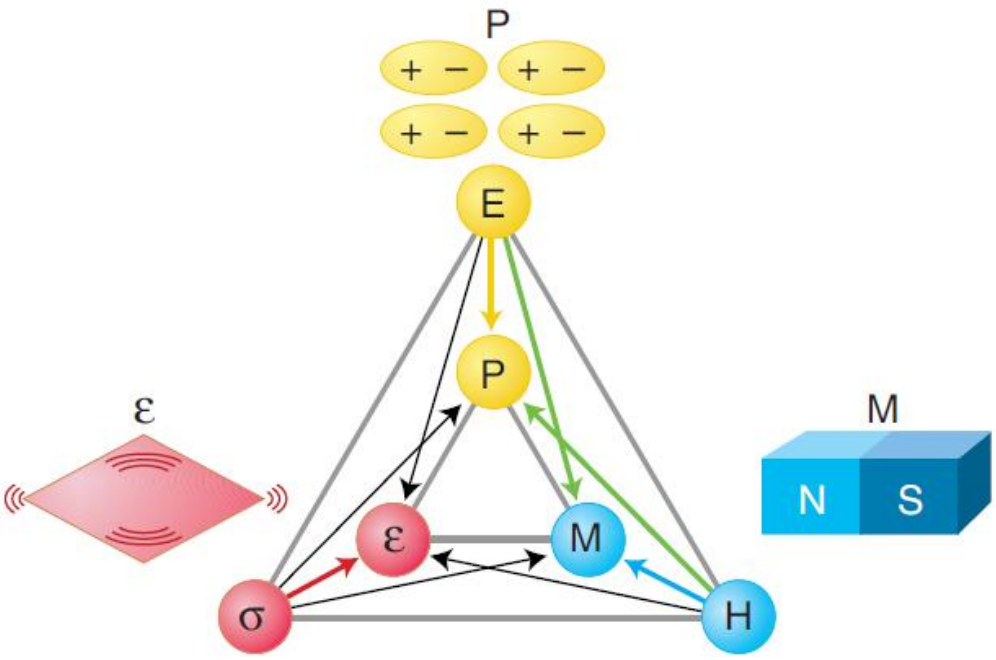

Figure 1-4. Phase control in ferroics and multiferroics. The electric field *E*, magnetic field *H*, and stress σ control the electric polarization *P*, magnetization *M*, and strain ε, respectively. In a ferroic material, *P*, *M*, or ε are spontaneously formed to produce ferromagnetism, ferroelectricity, or ferroelasticity, respectively. In a multiferroic, the coexistence of at least two ferroic forms of ordering leads to additional interactions. In a magnetoelectric multiferroic, a magnetic field may control *P* or an electric field may control *M* (green arrows) (Spaldin and Fiebig 2005).

1.2.1 Ferroelectric Materials

By definition, ferroelectric materials have a spontaneous polarization that can be reversed in its direction by an application of electric field below the Curie temperature. Ferroelectric materials have domains and exhibit a hysteretic response of polarization when electric field is applied, as shown in Figure 1-5 (Hill 2000).

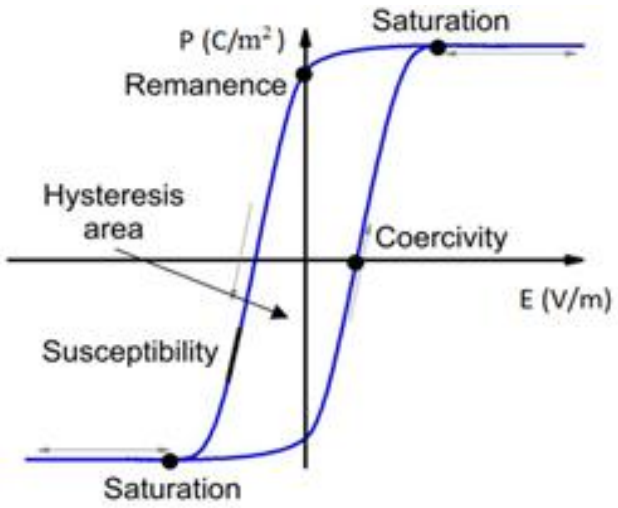

Figure 1-5. Typical polarization-electric field (P-E) hysteresis loop of a ferroelectric material (TANMS 2014).

The remnant polarization, $+P_r$ and $-P_r$, is the polarization in the absence of electric field. The saturation polarization, $+P_s$ and $-P_s$, is the maximum polarization value for the material and indicates that all the dipole moments in the material are aligned in the same direction with the electric field. The coercive field, $+E_c$ and $-E_c$, is the electric field at zero-net polarization and is the amount of electric field needed to switch the polarization negative to positive and positive to negative, respectively (TANMS 2014). Due to the P-E hysteresis, ferroelectric materials have been used in data storage and memory function, such as in ferroelectric RAM (FeRAM). They are also used in electromechanical transducers and actuators for sensor or medical applications (Hill 2000).

Perovskite-structure oxides are the most widely studied and used ferroelectric materials to date. These oxides have the formula ABO_3, where *A* is the large cation at the unit cell corners and *B* is the small cation at the center of an octahedron of oxygen anions, as shown in Figure 1-6.

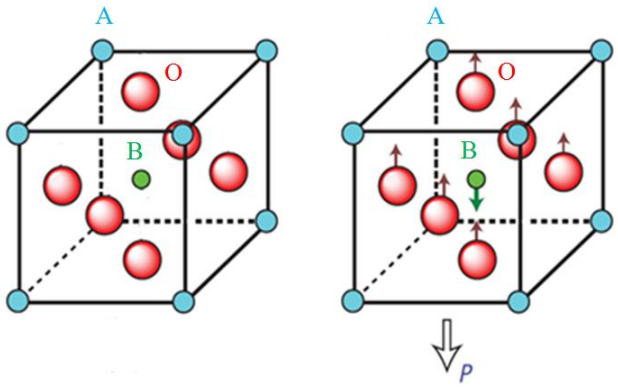

Figure 1-6. Perovskite-structure oxide ABO_3 and the origin of their polarization P (Horiuchi and Tokura 2008).

Ferroelectricity is determined by a balance between short-range repulsions and bonding considerations to stabilize the ferroelectric phase. At high temperatures, the short-range repulsive ion-ion interactions dominate to favor a symmetric unpolarized structure called the paraelectric phase. At temperatures below the Curie temperature, T_C, the polarized state becomes stable even in the absence of an applied field. The small cation *B* shifts off-center relative to the oxygen octahedron, as seen in Figure 1-7, and causes a structural distortion.

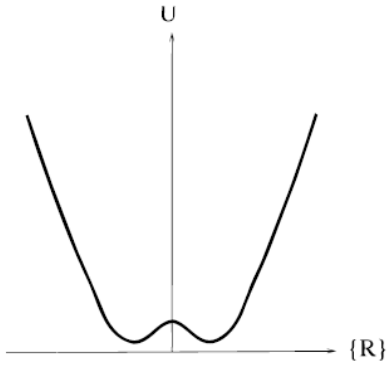

Figure 1-7. Characteristic double-well potential energy as a function of the position of the *B* cation between the oxygen anions in perovskite ferroelectrics (Hill 2000).

An electric dipole moment is created by this shift, thus inducing a spontaneous polarization in the ferroelectric material. Density functional theory found that the hybridization

between the cation *B* and oxygen interaction was essential in stabilizing the ferroelectric distortion in the perovskite-structures (Hill 2000).

1.2.1.1 Piezoelectric Coefficients

The equations of state for piezoelectric materials describe the relationship between the elastic (i.e. strain, *S*, and stress, *T*) and electric (i.e. electric field, *E*, and electric displacement, *D*) variables by:

$$D_i = d_{i\alpha} T_\alpha + \varepsilon_{ij}^T E_j \tag{1-1}$$

$$S_\alpha = s_{\alpha\beta}^E T_\beta + d_{i\alpha} E_i \tag{1-2}$$

where α, β = 1, 2, 3, 4, 5, 6 and i, j = 1, 2, 3 (Lefki and Dormans 1994). The tensors $s^E_{\alpha\beta}$ is the elastic compliances at a constant electric field, $d_{i\alpha}$ is the piezoelectric coefficient, and ε^T_{ij} is the permittivity at constant stress. Equation (1-1) and (1-2) describes the direct and converse piezoelectric effect, respectively. The subscripts α, β, i, j represent the different directions as given by Figure 1-8.

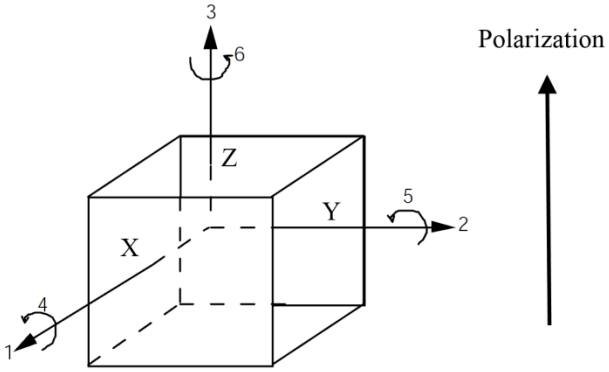

Figure 1-8. Reference axes of polarization, revised from (Jordan, Ounaies et al. 2001).

Typically the direction of polarization is defined as the 3-axis or the Z-axis of a rectangular system. Direction X, Y, and Z are represented as 1, 2, and 3, respectively.

Perpendicular to 1, 2, and 3-axis, the corresponding shear planes are represented as 4, 5, and 6. In general, the first subscript gives the direction of the electric variable and the second subscript gives the direction of the elastic variable.

Piezoelectric materials are characterized by piezoelectric coefficients which relate the mechanical and electrical properties. They are independent of the material's geometry, but dependent on the degree of polarization (Jordan, Ounaies et al. 2001). For strain or motion dependent applications, such as actuators and sonar transducers, a large piezoelectric coefficient d is an essential factor in determining the material's suitability because a greater d value indicates that more stress and strain can be achieved for the same amount of charge (Sakata, Wakabayashi et al. 1996). Direct piezoelectric effect is the creation of charges when stress is applied and may be represented as:

$$D = \frac{Q}{A} = dT \tag{1-3}$$

where D is the electric displacement (charge Q per unit area), T is the stress, and d is the piezoelectric coefficient in units of [C/N] (Jaffe, Cook et al. 1971). The sign of the charge is dependent on direction of the force (i.e. compressive or tensile), as shown in Figure 1-9.

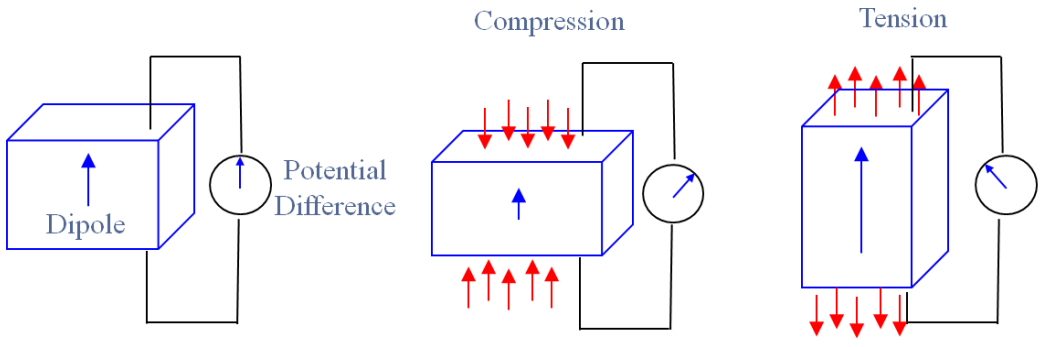

Figure 1-9. Illustration of the direct piezoelectric effect for compressive and tensile forces.

Converse piezoelectric effect is the occurrence of strain when an electric field is applied and may be represented as:

$$S = dE \tag{1-4}$$

where S is the strain, E is the electric field, and d is the piezoelectric coefficient in units of [m/V] (Jaffe, Cook et al. 1971). The contraction or expansion of the material is dependent on direction of the applied field relative to the polarization (i.e. anti-parallel or parallel), shown in Figure 1-10.

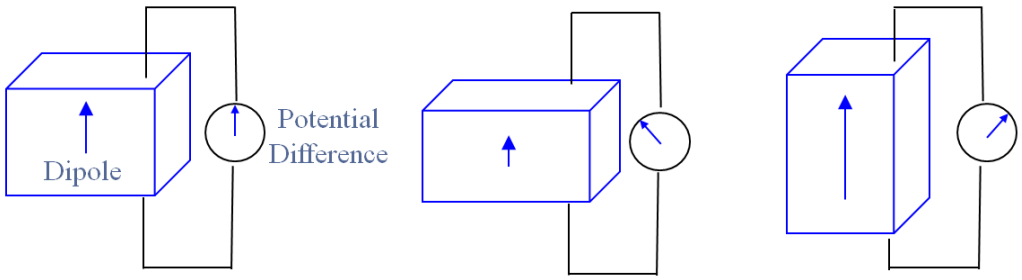

Figure 1-10. Illustration of the converse piezoelectric effect for anti-parallel and parallel applied electric fields.

As depicted in Figure 1-11, the piezoelectric material has a shear motion if the applied field is perpendicular to the polarization.

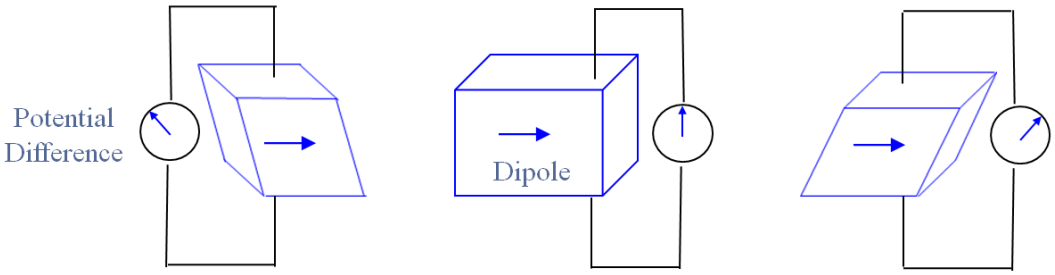

Figure 1-11. Illustration of induced shear motion for perpendicular applied electric fields.

In the same piezoelectric material, values of the piezoelectric constants differ depending on the chosen direction combination for the measurement. In addition to d, other coefficients

include *g* which relates the produced electric field to the applied stress, *e* which relates the produced stress to the applied electric field, and *h* which relates the produced electric field to the applied strain, and are defined as:

$$d = \left(\frac{\partial S}{\partial E}\right)_T = \left(\frac{\partial D}{\partial T}\right)_E \tag{1-5}$$

$$g = -\left(\frac{\partial E}{\partial T}\right)_D = \left(\frac{\partial S}{\partial D}\right)_T \tag{1-6}$$

$$e = -\left(\frac{\partial T}{\partial E}\right)_S = \left(\frac{\partial D}{\partial S}\right)_E \tag{1-7}$$

$$h = -\left(\frac{\partial T}{\partial D}\right)_S = -\left(\frac{\partial E}{\partial S}\right)_D \tag{1-8}$$

where the first and second set of terms correspond to the converse and direct piezoelectric effect, respectively (Jaffe, Cook et al. 1971). The piezoelectric coefficients are partial derivates and calculated at constant stress (subscript *T*), constant electric field (subscript *E*), constant electric displacement (subscript *D*), or constant strain (subscript *S*).

For sensor applications, a material with a large *g* value is desired to produce a voltage due to an applied stress (Jordan, Ounaies et al. 2001). The piezoelectric coefficient *g* and *d* are related through the following expression:

$$g = \frac{d}{K\varepsilon_o} \tag{1-9}$$

where *K* is the relative dielectric constant, ε_o is the permittivity of free space, and *g* is in units of [m-V/N] (Jaffe, Roth et al. 1955).

The piezoelectric properties of thin films and corresponding bulk materials are not the same due to the clamping effects between film and substrate (Lefki and Dormans 1994).

Although the thin film is clamped to the substrate in the in-plane direction (x and y-axis), it can move freely in the out-of-plane direction (z-axis). For perfect clamping between thin film and substrate, S_1 and S_2 are equal to zero and S_3 is non-zero. T_1 and T_2 are equal due to symmetry and T_3 is zero because the surface is free to move (Lefki and Dormans 1994). Therefore, the piezoelectric coefficients of thin films are known as effective coefficients and denoted by *f* subscripts:

$$d_{33,f} = \frac{e_{33}}{c_{33}^E} = d_{33} - \frac{2s_{13}^E}{s_{11}^E + s_{12}^E} d_{31} \tag{1-10}$$

$$e_{31,f} = \frac{d_{31}}{s_{11}^E + s_{12}^E} = e_{31} - \frac{c_{13}^E}{c_{33}^E} e_{33} \tag{1-11}$$

where c^E_{ij} are the stiffness constants, $d_{33,f}$ is the effective longitudinal piezoelectric coefficient, and $e_{31,f}$ is the effective transverse piezoelectric stress coefficient (Muralt 1997).

Another commonly used measurement is the electromechanical coupling factor, *k*, which evaluates the efficiency of the piezoelectric effect and defined as:

$$k^2 = \frac{\text{electrical to mechanical energy}}{\text{input electrical energy}} = \frac{\text{mechanical to electric energy}}{\text{input mechanical energy}} \tag{1-12}$$

where k is always less than 1 due to the partial conversion of energy (Jaffe, Cook et al. 1971). Values of *k* have been found to range from 0.1 for quartz to 0.5-0.7 for $Pb(Zr,Ti)O_3$ ceramics to 0.9 for Rochelle salt (Jaffe, Cook et al. 1971).

Dielectric properties are also important to consider for high dielectric material applications. The dimensionless relative dielectric constant, *K*, is the ratio of permittivity (ε) to that of free space (ε_o), where $\varepsilon_o = 8.85 \times 10^{-12}$ F/m. At a certain voltage, it is the ratio of the stored charge in the same set of electrodes separated by the material and vacuum as the dielectric (Jaffe, Cook et al. 1971). While *K* is less than 5 for organic materials and less than 20 for most

inorganic solids, it is usually several hundreds or thousands for piezoelectric ceramics (Jaffe, Cook et al. 1971).

The loss tangent, tan δ, is also called the dissipation factor or the dielectric loss. A unitless numeric, it is the ratio of the imaginary (out of phase) to the real (in phase) component of the complex permittivity, as shown in the following equation (Jaffe, Cook et al. 1971):

$$\tan\delta = \frac{\varepsilon''}{\varepsilon'} = \frac{\varepsilon_{\mathrm{Im}}}{\varepsilon_{\mathrm{Re}}} \tag{1-13}$$

The relative dielectric constant is related to the piezoelectric property via electromechanical coupling factor, *k*, through the equation:

$$K^S = K^T(1-k^2) \tag{1-14}$$

where K^S is the "clamped" dielectric constant when measured at constant stress, and K^T is the "free" dielectric constant when measured at constant stress (Jaffe, Cook et al. 1971).

The transverse piezoelectric coefficient, $e_{31,f}$, is typically determined by measuring the generated piezoelectric charge perpendicular to the sample (direction 3, as shown in Figure 1-8) as a function of in-plane strain (direction 1, as shown in Figure 1-8). Based on literature, it has been directly measured with one of the following three methods: *(1)* bending a cantilever (Cattan, Haccart et al. 1999), *(2)* laser interferometers, and *(3)* wafer flexure technique (Shepard, Moses et al. 1998).

In the cantilever method, the PZT thin film sample is first processed into small beams (length of 40 mm, width of 10 mm, and thickness of 0.38 mm) and then clamped at one end to the stage, as shown schematically in Figure 1-12 (Cattan, Haccart et al. 1999).

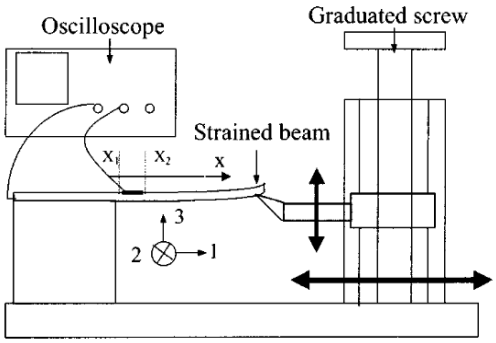

Figure 1-12. Cantilever method setup for measuring transverse piezoelectric coefficient, $e_{31,f}$ (Cattan, Haccart et al. 1999).

PZT films were sputtered over the entire cantilever surface and a platinum top electrode (area of 1 mm^2) was deposited on the top of it. A beam was used to flex the unclamped end of the cantilever perpendicular to the film plane, thus applying an in-plane strain to the film. By suddenly releasing the strained beam, electric charges were generated and the $e_{31,f}$ was directly measured (Cattan, Haccart et al. 1999). However, this technique is difficult to implement on thin film materials and a popular alternative technique is the usage of laser interferometers in either single- or double-beam set-ups. The monochromatic laser light results in a change of its optical path as a response to a piezoelectrically induced strain. However, this technique is limited by displacement unrelated to piezoelectricity (such as sample flexure and drift) and ambient noise (Shepard, Moses et al. 1998).

In comparison to other methods of characterizing the transverse piezoelectric coefficient, the wafer flexure technique is preferable because it does not require much sample preparation for measurement. An advantage to the wafer flexure technique is that a wide variety of substrate and sample geometry can be characterized. Small samples of ≤ 1 cm^2 can be characterized by bonding the small substrate to a Si wafer and relying on the strain transferring through the bonding layer (Maria, Shepard et al. 2005).

A high power audio speaker produces an oscillating air pressure inside the housing which flexes the wafer to apply strain to the sample. The pressure transducer is a Wheatstone bridge configuration where the output voltage across the bridge is proportional to the change in pressure in the chamber. As the film is displaced as a function of mechanical stress, the generated charge from the piezoelectric film is collected by an amplifier integrator. A voltage that is proportional to the amount of charge collected is read as the output signal, which is used to obtain the transverse piezoelectric coefficient value of $e_{31,f}$ (Shepard, Moses et al. 1998; Wilke, Moses et al. 2012). The strain and transverse piezoelectric coefficient can be accurately measured within 3 cm from the center of a 4-inch wafer for a 1.3 µm thick PZT film, as shown in Figure 1-13.

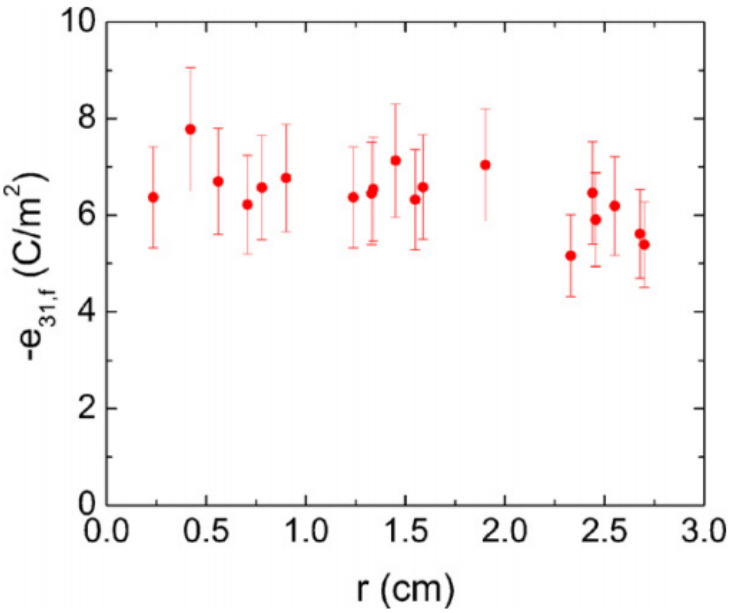

Figure 1-13. Radial dependence of transverse piezoelectric coefficient, $e_{31,f}$, for a 1.3 µm PZT film deposited by the sol-gel method. Error bars represent variation due to uncertainty in the gauge factor (Wilke, Moses et al. 2012).

1.2.1.2 Lead Zirconate Titanate

Lead zirconate titanate, i.e. $Pb(Zr_xTi_{1-x})O_3$ or PZT, is a solid solution of $PbTiO_3$ and $PbZrO_3$. Lead titanate, $PbTiO_3$, is ferroelectric with a tetragonal structure below its Curie point

of 490°C and becomes a cubic structure above the Curie point. Lead zirconate, $PbZrO_3$, is antiferroelectric below its Curie point of 230°C with an orthorhombic structure and becomes a cubic structure above the Curie point (Jaffe, Cook et al. 1971). Previous research has shown that $PbZrO_3$ has antiparallel displacements in the *a*-*b* plane, but has an irreversible net polarity along the *c* direction due to unbalanced antiparallel shifts resulting in a small piezoelectric effect (Jona, Shirane et al. 1957).

In the 1950s, PZT was first recognized as a ferroelectric material in Japan. Since then, extensive research has been performed to understand and utilize the excellent properties of PZT. It has been widely used in various applications because of its superior piezoelectric and ferroelectric properties (Jaffe, Cook et al. 1971). In comparison to non-ferroelectric materials (e.g. ZnO and AlN), PZT near its morphotropic phase boundary composition of Zr/Ti = 52/48 exhibits a higher dielectric constant and more than an order of magnitude larger piezoelectric coefficient and electromechanical coupling factor (Pulskamp, Polcawich et al. 2012), as shown in Table 1-2.

Table 1-2. Thin film piezoelectric and dielectric properties of ZnO, AlN, and PZT with references [1](Trolier-McKinstry and Muralt 2004), [2](Gupta and Mansingh 1998), [3](Tsubouchi and Mikoshiba 1985), and [4](Moazzami, Chenming et al. 1992).

Coefficients/Figures of Merit	ZnO (1-17 μm)	AlN (0.4-1 μm)	PZT (1-3 μm)
$-e_{31,f}$ (C/m^2)	1.0[1]	1.05[1]	8-12[1]
$d_{33,f}$ (pm/V)	5.9[1]	3.9[1]	60-130[1]
ε_{33} (dielectric constant)	10.9[1]	10.5[1]	300-1300[1]
tan δ (at 1-10 kHz, 10^5 V/m)	0.01-0.1[1]	0.003[1]	0.01-0.03[1]
Breakdown strength (kV/cm)	8[2]	1000[3]	62.5[4]

PZT has a perovskite structure and the formula ABO_3, where *A* is the Pb^{2+} ion and *B* is the Zr^{4+} and Ti^{4+} ion. As shown in Figure 1-14, the perovskite structure is a simple cubic unit

cell with the larger cation (*A*) in the corners, the smaller cation (*B*) in the body center, and the six oxygen (*O*) in the face centers forming an oxygen octahedra which may or may not be distorted (Jaffe, Cook et al. 1971).

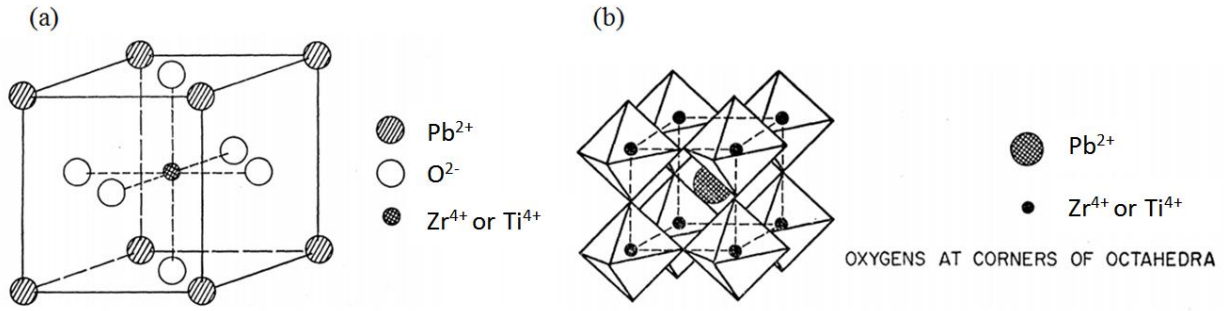

Figure 1-14. (a) Cubic perovskite-type structure ABO_3, (b) Perovskite structure ABO_3 considered as a three-dimensional framework of BO_6 octahedra (Jona, Shirane et al. 1957).

If the position of ion A is designated as the origin, the coordinates of the atoms would then be: *A* (Pb^{2+}) at 0, 0, 0; *B* (Zr^{4+} and Ti^{4+}) at ½, ½, ½; and *O* at ½, ½, 0 and ½, 0, ½, and 0, ½, ½ (Jona, Shirane et al. 1957).

Depending on the temperature and composition, lead zirconate titanate has several crystal structures, as shown in Figure 1-15 (Yang, Bao et al. 2010).

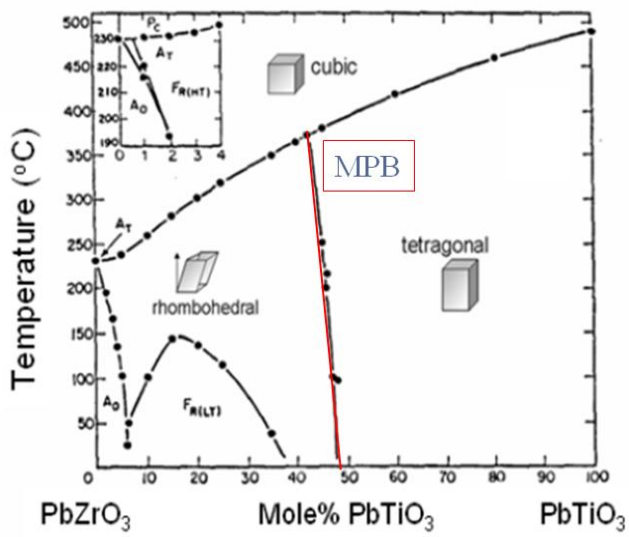

Figure 1-15. Morphotropic phase boundary (MPB) in the PZT system, revised from (Zhang, Xia et al. 2007).

As more Ti^{4+} in $PbTiO_3$ are replaced with Zr^{4+}, the crystal structure of PZT seems to abruptly change from tetragonal to rhombohedral, which is another ferroelectric phase, at the morphotropic phase boundary (MPB) (Jaffe, Cook et al. 1971). However, a ferroelectric monoclinic phase has been discovered in the PZT system at and below 300 K, providing a bridge between the rhombohedral and tetragonal phase transition near MPB (Noheda, Cox et al. 1999; Noheda, Gonzalo et al. 2000). It has been shown that the "rhombohedral" region consists of mixed monoclinic and rhombohedral phases, with the fraction of the monoclinic phase increasing towards the MPB. But, compositions of $0 < 1\text{-}x < 0.1$, where $1\text{-}x$ represents the fraction of $PbTiO_3$, were distinctly rhombohedral phase (Yokota, Zhang et al. 2009). With more Zr^{4+} substitutions, the antiferroelectric orthorhombic $PbZrO_3$ phase appears (Jaffe, Cook et al. 1971). Above the Curie point, which varies with composition, PZT has a cubic structure and is paraelectric.

The MPB of $Pb(Zr_xTi_{1-x})O_3$ is nearly independent of temperature and occurs at a specific composition that is considered where the two phases, rhombohedral and tetragonal, are present in equal quantity (Jaffe, Cook et al. 1971). Although this phase boundary has not been well defined

due to its dependence on the homogeneity of compositions and conditions during sample processing, it has been generally accepted to occur when fraction of $PbZrO_3$, *x*, is approximately 0.52 and fraction of $PbTiO_3$, *1-x*, is approximately 0.48 (Noheda, Cox et al. 1999; Yokota, Zhang et al. 2009). Compositions with rhombohedral symmetry has 8 polar [111] directions and with tetragonal symmetry has 6 polar [001] directions. The polar axis for the monoclinic phase was found to be at an angle of 24^o from the [001] axis towards the [111] axis (Noheda, Gonzalo et al. 2000).

PZT have attracted much interest because of the material's superior piezoelectric properties at the morphotropic phase boundary. The high piezoelectric response is a result of the greater freedom of movement the Pb ions have in the monoclinic structure compared to the ordered structures of rhombohedral and tetragonal (Izyumskaya, Alivov et al. 2007; Yokota, Zhang et al. 2009). It was discovered that as the polar axis rotates in the monoclinic plane, the unit cell would deform in the directions associated with the monoclinic distortion and not along the polar axis of the tetragonal or rhombohedral. In addition, compositions that are near MPB result in large atomic displacements, thus, accounting for the large electromechanical responses attributed to PZT (Guo, Cross et al. 2000).

In general, properties of piezoelectric films cannot be directly compared to ones found in bulk material. This is because the film is a component of the film/substrate composite structure and the film is clamped in-plane at the interface while it is free to move perpendicular to interface (Muralt 2000).

The material properties of PZT are found to be strongly dependent on the composition (Jordan, Ounaies et al. 2001). As shown in Figure 1-16 for the $Pb(Zr,Ti)O_3$ system, the dielectric constant and piezoelectric coefficients are enhanced at compositions near the morphotropic

phase boundary (MPB) of a 1 μm thick (111) textured PZT thin film grown by sol-gel, as shown by the vertical dashed line (Muralt 2000).

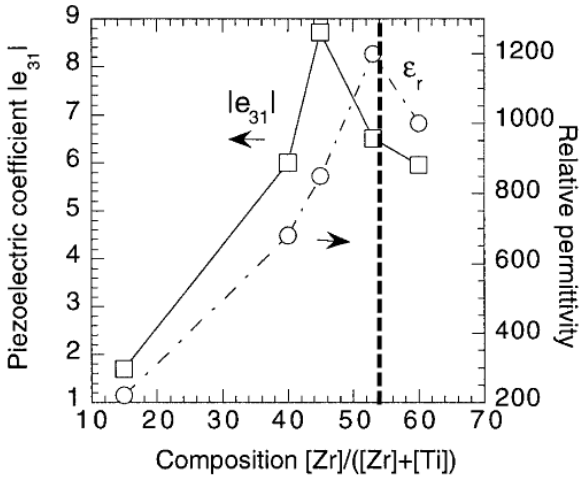

Figure 1-16. Transverse piezoelectric coefficient and dielectric constant of 1 μm thick PZT thin film (Muralt 2000).

Ferroelectric properties are also affected by PZT composition, as shown by P-E hysteresis loops in Figure 1-17 (Gerber, Bottger et al. 2006). It seems that although the positive and negative saturation polarization is independent of composition, the positive and negative remnant polarization and coercive field are dependent on the Zr/Ti ratio for a 130 nm thick PZT film deposited using chemical solution deposition on platinized silicon substrate (Gerber, Bottger et al. 2006).

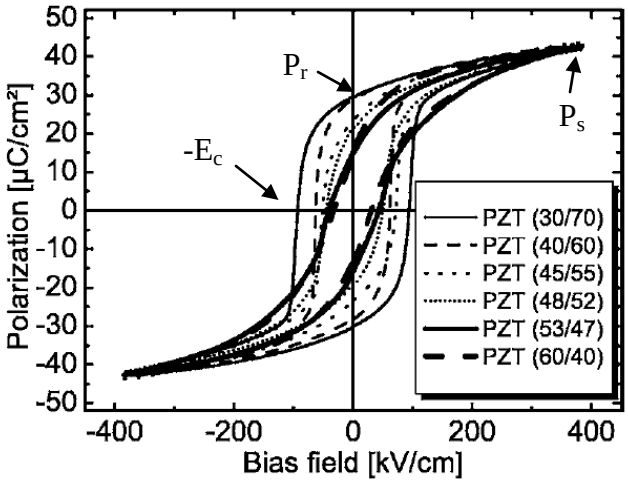

Figure 1-17. P-E hysteresis loop of 130 nm thick PZT thin films with increasing Zr content (Gerber, Bottger et al. 2006).

Besides composition, the orientation of the crystallized PZT thin films has found to affect their material properties (Ledermann, Muralt et al. 2003). Previous research has shown that 1 μm thick (100) textured PZT thin films exhibit higher transverse piezoelectric coefficient than (111) oriented films, as shown in Figure 1-18.

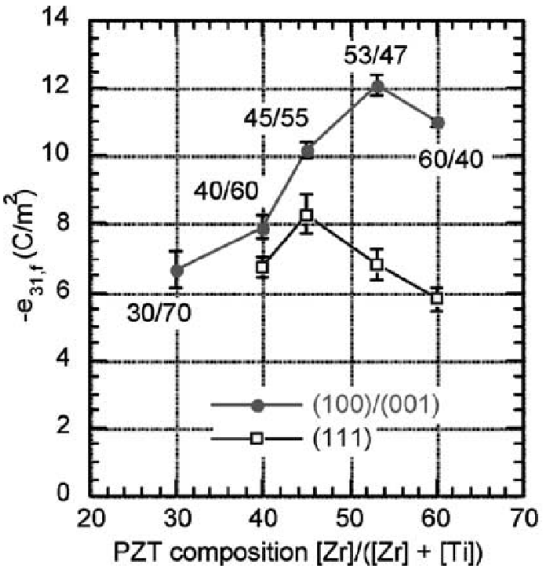

Figure 1-18.Transverse piezoelectric response in (111) and (100) textured 1 μm thick PZT films as a function of composition (Ledermann, Muralt et al. 2003).

Therefore, control of the texture in the crystallized PZT film is essential in obtaining optimal properties. However, the enhanced piezoelectric response is related to the quality (i.e. percentage) of the correctly oriented phase (Trolier-McKinstry and Muralt 2004).

It has also been observed that thickness of PZT thin films can change the piezoelectric properties, as shown in Figure 1-19, in which a 2 µm thick (100) textured $Pb(Zr_{0.53}Ti_{0.47})O_3$ film was compared with Berlincourt's PZT bulk ceramics and doped PZT 3203 HD from Motorola (Ledermann, Muralt et al. 2003).

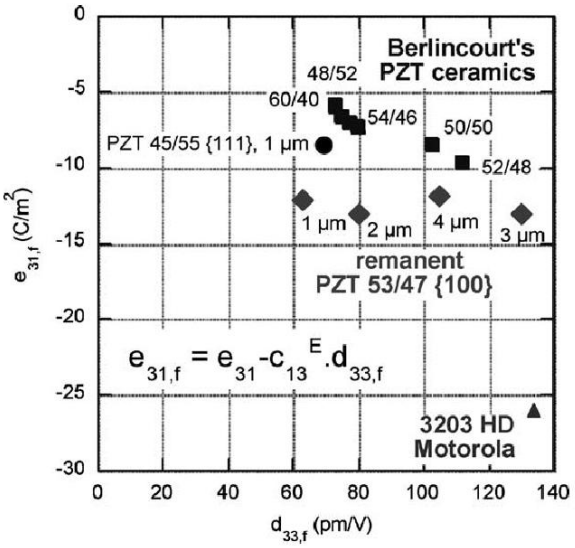

Figure 1-19. PZT thin films compared to bulk ceramic values: $e_{31,f}$ vs. $d_{33,f}$ (Ledermann, Muralt et al. 2003).

For the textured PZT thin film, it was observed that the $e_{31,f}$ was superior to PZT ceramics data and independent of thickness, while the $d_{33,f}$ became larger with increasing thicknesses (1-4 µm) (Ledermann, Muralt et al. 2003). Previous research has also seen an increase in the piezoelectric coefficient, $d_{33,f}$, and the dielectric constant as films are deposited with larger thicknesses from 1-12 µm (Chen, Udayakumar et al. 1996).

As a piezoelectric material, PZT couples electrical and mechanical energies. For example, applying an electrical field produces a deformation and applying a strain produces an

electrical signal. Because of this phenomenon, there is a large interest in utilizing piezoelectric thin films in piezoelectric microelectromechanical systems (piezoMEMS) as it allows small size devices to function at lower voltages and power (Muralt, Polcawich et al. 2009). An important property for the utilization of these thin films is a large piezoelectric coefficient (Eom and Trolier-McKinstry 2012). Because PZT has excellent piezoelectric properties, it has been primarily used in a variety of MEMS applications, including sensors, actuators, motors, switches, and energy harvesting (Muralt, Polcawich et al. 2009; Smith, Pulskamp et al. 2012).

As a ferroelectric material, PZT has two orientation states for polarization when zero external electric field is applied and can be switched by applying an electric field (Damjanovic 1998). With this unique property, PZT can be utilized in semiconductor devices for non-volatile random access memory (Mikolajick, Dehm et al. 2001). There is also interest in coupling ferroelectrics with ferromagnetic materials for various applications, with a focus on memory storage. By creating a multiferroic composite structure, it combines the best qualities of ferroelectric random access memory and magnetic data storage by allowing the data to be written electrically and read magnetically (Eerenstein, Mathur et al. 2006).

The primary goal of any deposition process is to be able to control and reproduce the growth of a thin film with the desired characteristics (Crowell 2003). Since the deposition process strongly affects the material properties of the grown thin film, it is essential for the processing conditions and chemistry to be carefully controlled. Unrelated to deposition method, there are a few main growth phenomena which PZT thin film experiences which need to be overcome (Muralt 2000). First, in order to achieve perovskite nucleation and phase, the correct stoichiometry must be attained otherwise competing pyrochlore structures occurs (Muralt 2000). Second, PbO not fully incorporated into the crystal lattice diffuses and evaporates at

temperatures above 500^{o}C (Muralt 2000), which can cause lead-depleted zones at the surface, leading to pyrochlore phase formation which degrades the material properties of PZT (Trolier-McKinstry 2008). Third, nucleation of perovskite structure is difficult to achieve because its activation energy is higher compared that of the growth process (Muralt 2000).

Over the years, PZT thin film has been successfully deposited with numerous physical and chemical methods, including chemical solution deposition (CSD) (Ledermann, Muralt et al. 2003; Prume, Muralt et al. 2007), physical vapor deposition (PVD) (Kalpat and Uchino 2001; Bharadwaja, Griggio et al. 2011), and chemical vapor deposition (CVD) (Yamazaki, Tsuyama et al. 1992; Lee, Ku et al. 2002).

CSD involves spin-coating or dip-coating the thin film onto the substrate, followed by heat treatments for drying and crystallization. These processes can quickly cover large surface areas, are relatively cheap, and can be easily scalable, but more research need to be done to make high quality and oriented films (Martin, Chu et al. 2010).

PVD involves the deposition of the precursors onto the substrate through a physical process, such as sputtering, evaporation, or sublimation (Crowell 2003). Sputtering has several advantages, such as its capability of depositing a variety of materials and it is easy to control and reproduce the composition of the thin film (Ghandhi 1994). Sputter deposition involves applying an electric field across an inert gas, producing ions to bombard the target material, ejecting sputtering atoms that then deposit onto the surface of the substrate, and producing the desired thin film (Ghandhi 1994). Another PVD process is pulsed laser deposition (PLD), in which a high intensity pulsed-laser beam is used to evaporate the target material that is to be deposited on a surface (Izyumskaya, Alivov et al. 2007). Although PLD is a simple process and a variety of materials can be used, it cannot cover large surface areas and can eject large particles onto the

substrate resulting in a non-uniform film (Martin, Chu et al. 2010). Molecular beam epitaxy (MBE) is another PVD process that has been heavily studied in the growth of thin films and involves evaporating the target material through heat or an electron beam to deposit on the heated substrate surface (Izyumskaya, Alivov et al. 2007). Because MBE depends on the evaporating species to travel from the effusion cell to the substrate without colliding or interacting with other molecules, this method requires to be performed under an ultra-high vacuum environment (Ghandhi 1994). Although MBE grows high quality thin films, it is an expensive technique and is difficult to scale-up for industrial usage (Martin, Chu et al. 2010).

Unlike PVD, metal-organic chemical vapor deposition (MOCVD) involves flowing the volatile species of elements or compounds to deposit on the substrate through a vapor phase chemical reaction (Ghandhi 1994). CVD deposition includes surface reaction and mass transport phenomenon, which are both temperature dependent. The process is surface reaction-rate limited at low temperatures and mass-transport limited at high temperatures (Crowell 2003). MOCVD can deposit uniform thin films over a large surface area, but appropriate precursors and operating temperature first need to be determined (Martin, Chu et al. 2010).

In the current trend, most PZT thin films are synthesized via CSD or MOCVD due to low-cost and coverage abilities (Muralt 2000). However, device applications are moving towards three-dimensional (3-D) structures and MOCVD technique exhibits poor step coverage (Lee, Ku et al. 2002). To obtain conformal films on 3-D configurations, a low temperature deposition method operating in the surface reaction-limited regime is required, such as atomic layer deposition (ALD) (Lee, Ku et al. 2002). Previous research has shown that liquid injection ALD of PZT thin films can be utilized to achieve conformal films varying in thickness between 43-54 nm over small aspect ratio (1.2:1) 3-D hole structures with diameter of 0.25 μm and depth

of 0.30 μm (Watanabe, Hoffmann-Eifert et al. 2008). Table 1-3 summarizes the reported dielectric, ferroelectric, and piezoelectric property values for PZT thin films deposited via various synthesis methods.

Table 1-3. Reported values of dielectric, piezoelectric, and ferroelectric properties of PZT thin films synthesized by various techniques with references [1](Nguyen, Nazeer et al. 2010), [2](Ledermann, Muralt et al. 2003), [3](Muralt, Dubois et al. 1999), [4](Bastani, Schmitz-Kempen et al. 2011), [5](Wolf and Trolier-McKinstry 2004), [6](Kim, Eom et al. 2006), [7](Foster, Bai et al. 1997), and [8](Zhang, Perng et al. 2011).

Synthesis Method	PLD[1]	Sol-Gel[2]	Sol-Gel[3]	Sol-Gel[4]	Sol-Gel[5]	Sputtering[6]	CVD[7]	ALD[8]
Thickness (μm)	1	1-2	1	0.160	2	3.8	0.250	0.014
Substrate	SRO/ YSZ/ Si	Pt(111)/ TiO_2/Si O_2/Si	Pt(111)/ TiO_2/Si O_2/Si	Pt(111)/ Ti/SiO_2 /Si	Pt(111)/ Ti/SiO_2 /Si	$SrRuO_3$/ (001) $SrTiO_3$/Si	$SrRuO_3$ /(001) $SrTiO_3$	Al_2O_3 /SiC
Zr/Ti	52/48	53/47	40/60	53/47	53/47	52/48	49/51	44/56
Orientation	(110)	(100)/ (001)	(111)	(100)	--	(001)	(001)	002
k	1360	935	680	~580	~840	--	~480	50
P_r ($\mu C/cm^2$)	20.4	--	--	~16	~21.8	~30	~44	4.6
E_c (kV/cm)	36	--	--	~140	~42	--	~60	1300
$d_{33,f}$ (pm/V)	--	85	--	~54	--	~330	--	--
$e_{31,f}$ (C/m^2)	--	12.1	6.73	--	5.85	--	--	--

1.2.2 Ferromagnetic Materials

Analogous to ferroelectrics, ferromagnetic materials have a spontaneous magnetization in the absence of an applied magnetic field and are characterized by the magnetization and flux density-magnetic field hysteresis loop, as shown in Figure 1-20.

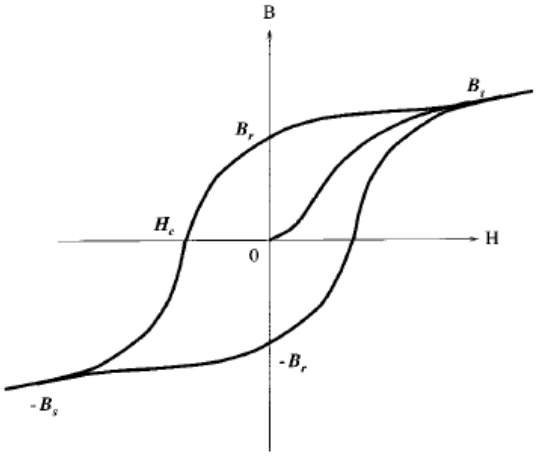

Figure 1-20. Hysteresis loop for a ferro- or ferrimagnet material (Hill 2000).

The ferromagnetic material starts in an unmagnetized state, and as magnetic field is applied in the positive direction, the magnetization increases until saturation at B_s. When the magnetic field is removed, the magnetization decreases from B_s to B_r, the remnant magnetization. The coercivity, H_C, is the magnetic field that has to be applied for the magnetization to reach zero again (Hill 2000).

The driving force behind ferromagnetism is exchange energy, which is minimized when all electrons have the same spin. The opposing force is the increased band energy when electrons transfer from lowest to higher energy band states, which prevents simple metals from being ferromagnetic (Spaldin 2003). For example, the Fermi energy of ferromagnetic transitions metals Fe, Ni, and Co is in a region where the 3d and 4s bands overlap, as shown in Figure 1-21.

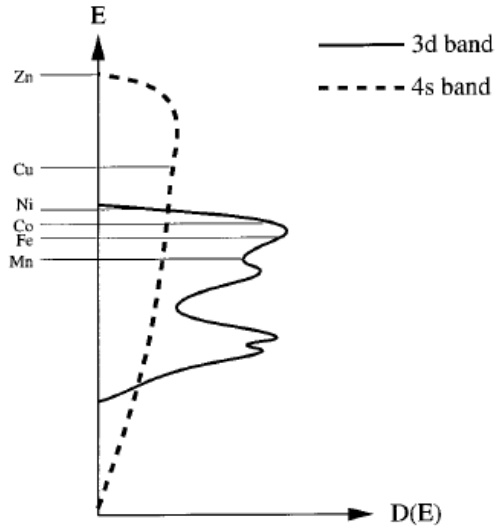

Figure 1-21. Schematic 3d and 4s densities of states in transition metals. The positions of the Fermi levels in Zn, Cu, Ni, Co, Fe, and Mn are shown (Spaldin 2003).

If the Fermi energy lies within the 3d band, such as in Ni, then a spontaneous magnetic moment exists in the ground state because the exchange interaction dominates and an external field is not needed to induce the magnetization. Cu is not ferromagnetic because its Fermi level lies above the 3d bands and the 4s band has no exchange splitting, which means that there is an equal number of electrons with up- and down- spins. Zn is not ferromagnetic because both the 3d and 4s bands are filled, so they do not contribute a magnetic moment (Hill 2000; Spaldin 2003).

1.2.2.1 Magnetostriction Coefficient

When a magnetic field is applied to a ferromagnetic material, it undergoes a change in length known as its magnetostriction coefficient, λ:

$$\lambda = \frac{\Delta l}{l} \tag{1-15}$$

When the magnetostriction coefficient is measured at magnetic saturation, it is called the saturation magnetostriction coefficient, λ_S (Cullity and Graham 2009). Some materials (e.g. iron) have a positive magnetostriction coefficient, which means that the material elongates along the direction of magnetization, while other materials (e.g. nickel) have a negative magnetostriction coefficient, which means that the material contracts along the direction of magnetization. The change in length are usually small and are in the tens of parts per million, typically of the order of 10^{-5} (Spaldin 2003). The magnetostriction coefficients at room temperature for several materials are listed in Table 1-4.

Table 1-4. Magnetostriction constants λ_{100}, λ_{111}, and polycrystalline λ_S ($x10^6$) at room temperature for several materials (O'Handley 2000).

Materials	λ_{100}	λ_{111}	Polycrystalline λ_S
3d Metals			
Fe	21.0	-21.0	-7.0
Ni	-46.0	-24.0	-34.0
FeCo	140.0	30.0	–.0
$Fe_{80}B_{20}$	–.0	–.0	32.0
$Fe_{40}Ni_{40}B_{20}$	–.0	–.0	14.0
4f Metals/Alloys			
$TbFe_2$	–.0	2600.0	1753.0
$Tb_{0.3}Dy_{0.7}Fe_2$ (Terfenol-D)	–.0	1600.0	1200.0
Spinel Ferrites			
Fe_3O_4	-15.0	56.0	40.0
$CoFe_2O_4$	-670.0	120.0	-110.0
Garnets			
$Y_3Fe_5O_{12}$ (YIG)	-1.4	-1.6	-2.0

1.2.2.2 Magnetostriction Measurement Techniques

In order to measure the magnetostriction, there are two common measurement techniques. Strain gages are typically used to measure magnetostriction in bulk samples, while the bending technique is typically used for measuring thin films.

For bulk samples, an electrical-resistance strain gauge made from an alloy wire or foil grid is cemented to the sample. When the sample changes shape, the grid also changes, which causes a change in the electrical resistance of the gauge (Cullity and Graham 2009). Based on the gauge factor, the ratio of resistance change to length change, the strain of the sample can be calculated (O'Handley 2000).

For thin film samples, the bending technique is usually used. The direct method is to apply a magnetic field to induce a magnetoelastic stress causing the substrate to bend. Capacitance or optical techniques can then be used to detect the substrate's deflection, allowing the magnetostriction coefficient to be quantified (O'Handley 2000). The inverse method is to apply a known stress to the sample and measure the resulting change in the magnetic anisotropy, thus giving the magnetostriction coefficient (Cullity and Graham 2009).

1.2.3 Single-phase Multiferroics

The largest challenge in multiferroics is the scarcity of a single-phase multiferroic, a material that exhibit both ferroelectric and ferromagnetic properties, at room temperature (Martin, Chu et al. 2010). This is largely due to the competing electron configuration where ferroelectric materials correspond to d^0 on the cation and ferromagnetic materials require partially filled transition metal orbitals (Hill 2000; Spaldin and Fiebig 2005). A variety of thin film single-phase multiferroic material systems have been studied (e.g. rare-earth manganites

such as $YMnO_3$ and $BiMnO_3$, $BiCoO_3$, $PbVO_3$, and Bi_2NiMnO_6) with $BiFeO_3$ (BFO) being the most promising multiferroic material (Martin, Crane et al. 2008; Martin, Chu et al. 2010). BFO is a ferroelectric (from 4-1103K) and antiferromagnetic (Néel temperature of 673K) multiferroic at room temperature. Previous research has measured BFO thin films to have spontaneous polarization of 90 $\mu C/cm^2$ and magnetoelectric coupling coefficient of 3 V/cm-Oe at zero field (Martin, Crane et al. 2008). However, the magnetoelectric coupling of single-phase materials are generally too weak for potential device applications (Szepieniec 2012).

1.2.4 Nanoscale Composite Multiferroics

With the development of new experimental techniques, composite multiferroics have been observed to have stronger magnetoelectric coupling than single-phase multiferroics (Lawes and Srinivasan 2011), as shown in Figure 1-22.

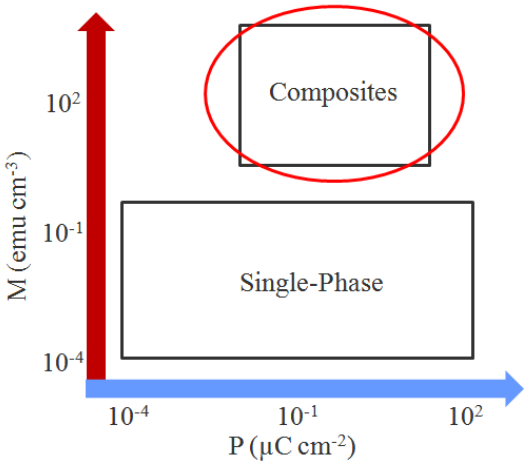

Figure 1-22. Schematic representation of the approximate magnitudes of the magnetization and polarization in composite multiferroics and single-phase multiferroics. While the properties of some materials fall outside these boundaries, this figure is intended to provide an illustration of the relative differences among the different classes of multiferroic materials, revised from (Lawes and Srinivasan 2011).

Multiferroic composites, which are materials that simultaneously exhibit at least two ferroic order parameters, are of particular interest due to their potential application in nanoscale devices (Spaldin and Fiebig 2005; Nan, Bichurin et al. 2008; Vaz, Hoffman et al. 2010; Wang, Hu et al. 2010; Bibes, Villegas et al. 2011; Hwang, Iwasa et al. 2012). One path to magnetoelectric materials is through strain-coupling a piezoelectric and a magnetostrictive material (Eerenstein, Mathur et al. 2006; Ramesh and Spaldin 2007; Martin, Crane et al. 2008; Martin, Chu et al. 2010; Lawes and Srinivasan 2011). The ME coupling refers to the resulting polarization from an applied magnetic field (i.e. direct magnetoelectric effect) or the resulting magnetization from an applied electric field (i.e. converse magnetoelectric effect). In composites, the ME effect occurs indirectly through strain or stress at interface of the ferroelectric and ferromagnetic layers, as shown in Figure 1-23 (Wang, Hu et al. 2010).

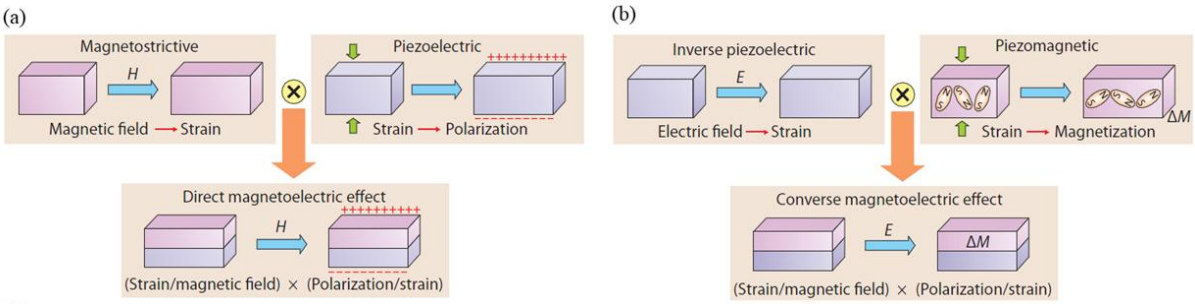

Figure 1-23. Schematic illustration of strain-mediated ME effect in a composite system consisting of a magnetic layer (purple) and ferroelectric layer (pink): (a) direct ME effect and (b) converse ME effect (Wang, Hu et al. 2010).

When an external electric field is applied to such a composite, the ferroelectric is strained, and this strain is transferred to the magnetostrictive and induces a change in magnetization. Thus, magnetization can be controlled using an electric field, and conversely, electric polarization using a magnetic field. This structure relies on strain transfer at the interface

of the two materials and has been demonstrated to show a higher magnetoelectric coupling effect than single-phase magnetoelectrics (Lawes and Srinivasan 2011).

The direct (converse) ME effect occurs when a magnetic (electric) field induces strain in the magnetic (ferroelectric) layer, which is transferred to the ferroelectric (magnetic) layer to produce polarization (magnetization). The magnitude of ME coupling for composites can be described by the effective magnetoelectric coefficient, α:

$$P = \alpha H \tag{1-16}$$

where P is the induced polarization, H is the applied magnetic field, and α is expressed in s/m. However, the ferroelectric polarization is hard to determine so the ME voltage coefficient, α_E, (units of mV/cm-Oe) is used instead to compare composite systems. It is defined as:

$$\alpha_E = \frac{\delta E}{\delta H} \tag{1-17}$$

The ME voltage coefficient is related to α by:

$$\alpha_E = \frac{\alpha}{\varepsilon_0 \varepsilon_r} \tag{1-18}$$

where ε_r is the relative permittivity of the material. For converse ME effect, the inverse ME coefficient (units of Oe-cm/mV) is used and defined as (Vaz, Hoffman et al. 2010; Szepieniec 2012):

$$\alpha_H = \frac{\delta M}{\delta E} \tag{1-19}$$

To maximize strain-coupling, a large interface area is desirable, and popular techniques for achieving this include, but are not limited to, spontaneous self-assembly phase-separated gas-phase or sol-gel deposition to create columnar-like structures in a matrix (Zheng, Wang et al. 2004; Aimon, Choi et al. 2014) or nanoparticles embedded in a matrix (Wan, Wang et al. 2005; Ryu, Murugavel et al. 2006; Zhong, Wang et al. 2007), respectively, and multilayer depositions

to create flat sheets (Wu, Zurbuchen et al. 2006; Ma, Cheng et al. 2007). Primarily, there are three types of nanostructures for ME composites denoted as 0-3, 2-2, and 1-3, in which the number represents the dimension of each phase, as shown in Figure 1-24 (Wang, Hu et al. 2010).

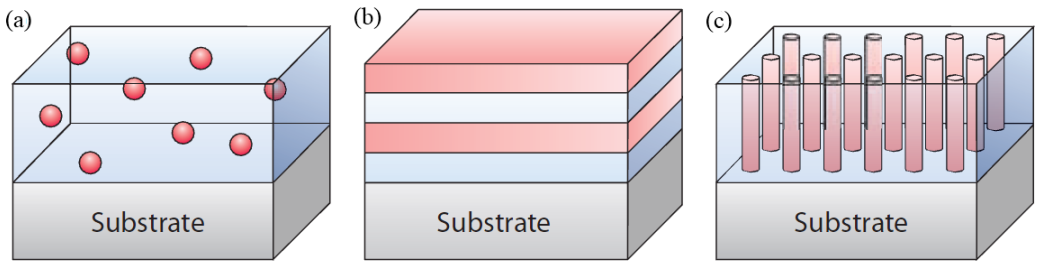

Figure 1-24. Schematic illustration of ME composite nanostructures: (a) 0-3 particle nanocomposite, (b) 2-2 horizontal heterostructure, and (c) 1-3 vertical heterostructure (Wang, Hu et al. 2010).

In the 0-3 particle nanocomposite, the single-phase particles (represented by 0) are embedded in another single-phase matrix (represented by 3). In the 2-2 horizontal heterostructure, the single-phase films (represented by 2) are either bilayer or multilayer composites. In the 1-3 vertical heterostructure, one-phase nanopillars (represented by 1) are embedded in another phase matrix (represented by 3) (Wang, Hu et al. 2010). Previous studies have been performed on coupling PZT with various magnetic layers, which the results for several material systems are shown in Table 1-5. Factors affecting the magnetoelectric coupling include temperature, synthesis process, and nanostructure geometry.

Table 1-5. Reported results of PZT magnetoelectric composites with references [1](Ryu, Park et al. 2007), [2](Ma, Cheng et al. 2007), [3](Wu, Zurbuchen et al. 2006), [4](Ryu, Murugavel et al. 2006), and [5](Liu, Li et al. 2007).

Zr/Ti of PZT	40/60[1]	52/48[2]	30/70[3]	52/48[4]	52/48[5]
Magnetic Layer	$Ni_{0.8}Zn_{0.2}Fe_2O_4$ (NZFO)	$La_{0.7}Sr_{0.3}MnO_3$ (LSMO)	$La_{1.2}Sr_{1.8}Mn_2O_7$ (LSMO crystal)	$NiFe_2O_4$ (NFO)	$CoFe_2O_4$ (CFO)
Nanostructure Geometry	2D-2D (alternating)	2D-2D (bilayer)	2D-2D (bilayer)	0D-3D	0D-3D
Synthesis Technique	PLD	PLD	CSD	PLD	CSD
Total Thickness	450 nm	860 nm	110 nm	--	100 nm
α_E (mV/cm-Oe)	15-30	4.2	522	16	P_r reduced by 22% at 1200 Oe
P_r ($\mu C/cm^2$)	26	27.5 (PZT layer)	44	45	8.3
E_c (kV/cm)	500	30	--	275	--
M_s (emu/cm^3)	46	8 (LSMO layer)	--	35	118
H_c (Oe)	300	75	--	70	--

The high coupling coefficient, α_E, reported by Wu et al. was most likely due to the in-plane epitaxial relationship between the PZT film and the LSMO bulk crystal substrate (Wu, Zurbuchen et al. 2006).

1.2.4.1 Atomic Layer Deposition

Atomic layer deposition (ALD), also known as atomic layer epitaxy (ALE), possesses the unique ability to conformally coat complex structures with high quality thin films compared to other deposition techniques, making it the ideal method to synthesize multiferroic nanocomposites. For this reason, this technique recently has attracted much attention, especially as microelectronic devices are being continuously scaled down to smaller sizes (Puurunen 2005). Although ALD offers great control over stoichiometry and sub-nm thicknesses, it is limited by its low throughput and small deposition rate (Crowell 2003).

ALD is a surface-reaction controlled process and a type of chemical vapor deposition technique (Puurunen 2005). It is based on alternating, self-limiting surface reactions to obtain a layer-by-layer atomic control deposition, as shown in Figure 1-25 (Crowell 2003).

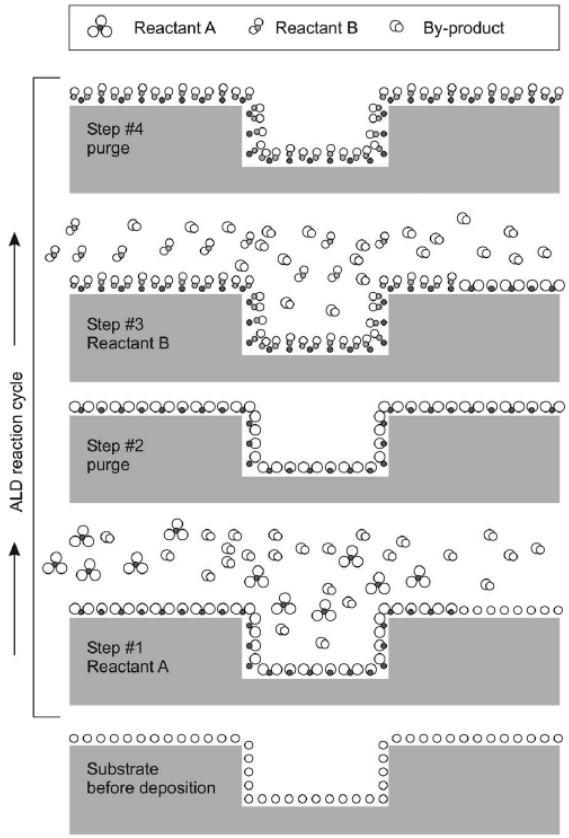

Figure 1-25. Schematic illustration of one ALD reaction cycle (Puurunen 2005).

By alternating the gas pulses, the precursors react with all the active surface sites until saturation is reached. Due to the self-limiting reactions, only a monolayer of material is formed during a pulse which allows great control over the stoichiometry (Crowell 2003). Between the precursor pulses, a purging step with an inert gas (e.g. nitrogen or argon) or a pumping step is required to inhibit gas phase reactions and remove any by-products (Crowell 2003).

Several experimental parameters that need to be considered for processing include temperature, pressure, type of substrate, and time of ALD reactions (Puurunen 2005). Uniform

substrate temperature is necessary to achieve a thin film with uniform thickness because ALD is a surface adsorption and reaction controlled process (Crowell 2003). If the substrate temperature varies across the surface, the thickness, uniformity, purity, stoichiometry, and interface quality of the deposited thin film are affected (Crowell 2003). The partial pressure of the reactants should be considered because it can affect the amount of adsorbed species (Puurunen 2005). Using different types of substrates does not result in the same film even if all other experimental conditions remain constant because of the varying number and type of active surface sites (Puurunen 2005). It is normal to observe an incubation period, where the first few ALD cycles have a lower deposition rate than after tens of cycles have been performed, when depositing films on different substrates (Choi, Zhang et al. 2013). ALD is based on self-limiting half-reactions in which the surface needs to be saturated with adsorbed species, so the time needed to saturate the surface, complete the reaction, and purge/pump down the system in between precursor pulses need to be carefully considered (Puurunen 2005).

1.2.4.2 PZT/CFO Multiferroic Nanocomposites

It is difficult find intrinsic multiferroic materials due to the opposite mechanisms – ferroelectric require empty *d* orbitals while magnetic moments result from partially filled *d* orbitals (Ramesh and Spaldin 2007). The magnetoelectric (ME) coupling is small or non-existent at room temperature for most intrinsic multiferroic materials. Therefore, it is necessary to engineer a two-phase nanostructured multiferroic composite by combining a ferroelectric constituent (i.e. $PbZr_xTi_{1-x}O_3$, PZT) with a ferromagnetic constituent (i.e. $CoFe_2O_4$, CFO) to obtain a strong magnetoelectric coupling. The two materials chosen to engineer multiferroic nanocomposites are piezoelectric lead zirconate titanate ($PbZr_{0.52}Ti_{0.48}O_3$ or PZT) and negative

magnetostrictive cobalt ferrite ($CoFe_2O_4$ or CFO). By making a composite material with PZT and CFO, the ferroelectric and ferrimagnetic properties can be taken advantage of to make a new class of engineered multiferroic nanocomposite. When an electric field is applied to the composite, magnetization is induced via strain at the PZT/CFO interface, and vice versa. Table 1-6 shows reported remnant polarization, coercive electric field, saturation magnetization, and coercive magnetic field results for PZT/CFO multiferroic nanocomposites.

Table 1-6. Reported results of PZT-CFO multiferroic nanocomposites with references [1](Ortega, Bhattacharya et al. 2006), [2](Ding, Wu et al. 2011), [3](Chen, Zhu et al. 2010), [4](Tahmasebi, Barzegar et al. 2013), and [5](Zhang, Dai et al. 2010).

Zr/Ti of PZT	53/47[1]	53/47[2]	53/47[3]	95/5[4]	53/47[5]
Nanostructure Geometry	0D-3D	2D-2D	2D-2D	2D-2D	0D-3D
Synthesis Technique	PLD	PLD	CSD	PLD	PLD
CFO Total Thickness	40 nm	4000 nm	1775 nm	40 nm	164 nm
Total Thickness	350 nm	580 nm	3550 nm	295 nm	360 nm
P_r ($\mu C/cm^2$)	25	4.5	17.22	P_s = 64	8.5
E_c (kV/cm)	68	15	73	106	200
M_s (emu/cm^3)	80	71	10	100	276
H_c (Oe)	960	1.3	2	1885	1065

However, these composites are still dense structures, and like all dense thin films they suffer from substrate clamping, which hinders in-plane strain and thus limits magnetoelectric coupling. To alleviate this, mechanical flexibility is introduced by creating a composite with nanoscale porosity.

The composite is composed of a mesoporous CFO framework on which a thin layer of PZT is deposited. The CFO framework is fabricated using evaporation-induced self-assembly (EISA), which has been used to produce many metal oxides with a variety of three-dimensional

nanoarchitectures (Ogawa 1994; Yang, Deng et al. 1998; Brinker, Lu et al. 1999; Mamak, Coombs et al. 2000; Brezesinski, Groenewolt et al. 2006; Fattakhova-Rohfing, Brezesinski et al. 2006; Quickel, Schelhas et al. 2015). This control over morphology is of particular interest to ferroic materials, as the effects on mechanical flexibility can drastically alter the strain states in the material, and thus the overall ferroic properties as well (Quickel, Le et al. 2010; Quickel, Schelhas et al. 2015). A CFO precursor solution is templated with an amphiphilic diblock copolymer template which self-assembles into micelles upon sol-gel deposition. Pyrolysis of the polymer template leaves behind a network of interconnected pores that can subsequently be filled by atomic layer deposition (ALD).

Atomic layer deposition, a type of chemical vapor deposition based on alternating, self-limiting surface reactions to obtain a layer-by-layer growth, is required because a controlled, precise deposition is ideal for the structure of the porous CFO framework. In ALD, alternating pulses of gaseous precursors react with all active surface sites until saturation is reached, and due to the self-limiting nature of the reactions, only a monolayer of material is formed during a pulse which allows great control over the stoichiometry and thickness (George 2010). This technique allows a conformal, ultra-thin deposition of PZT onto a surface of any shape, creating a PZT/CFO composite with high interface area. Depending on how much PZT is deposited, the porous network can either be completely or partially filled, providing fine control over the final porosity of the material.

In this work, the structure of porous magnetoelectric composites was examined by partially or fully coating the CFO framework in order to determine the effect of porosity on magnetoelectric coupling between PZT film and CFO template. By controlling the degree to which the pores are filled, the mechanical flexibility of the films could be tuned, thus, directly

affecting the amount of strain changes that can be expressed in the material. The strain effects on magnetoelectric coupling were measured by observing the change in magnetization of the composite films upon *ex situ* application of an electric field.

1.3 Magnetoelectric Random Access Memory (MeRAM) and Voltage-Controlled Magnetic Anisotropy (VCMA) Effect

There is a fast-growing need in the semiconductor industry for alternative memory technologies which can combine nonvolatile operation, high speed, endurance, and high density in a single silicon-compatible device. Magnetic random access memory (MRAM) is an emerging candidate providing potential advantages in a range of standalone and embedded memory applications. MRAM uses magnetic tunnel junctions (MTJs) due to their large tunneling magnetoresistance (TMR) ratio, thus allowing a large read-out signal, and capability of integration with conventional semiconductor processes (Alzate 2014). An MTJ is composed of two ferromagnetic layers, one with a magnetization fixed in a given direction (called "fixed layer") and the other layer with a magnetization that can be switched parallel or antiparallel to the fixed layer (called "free layer"), with the ferromagnetic layers separated by a non-magnetic dielectric oxide (called "tunnel barrier"), as shown in Figure 1-26.

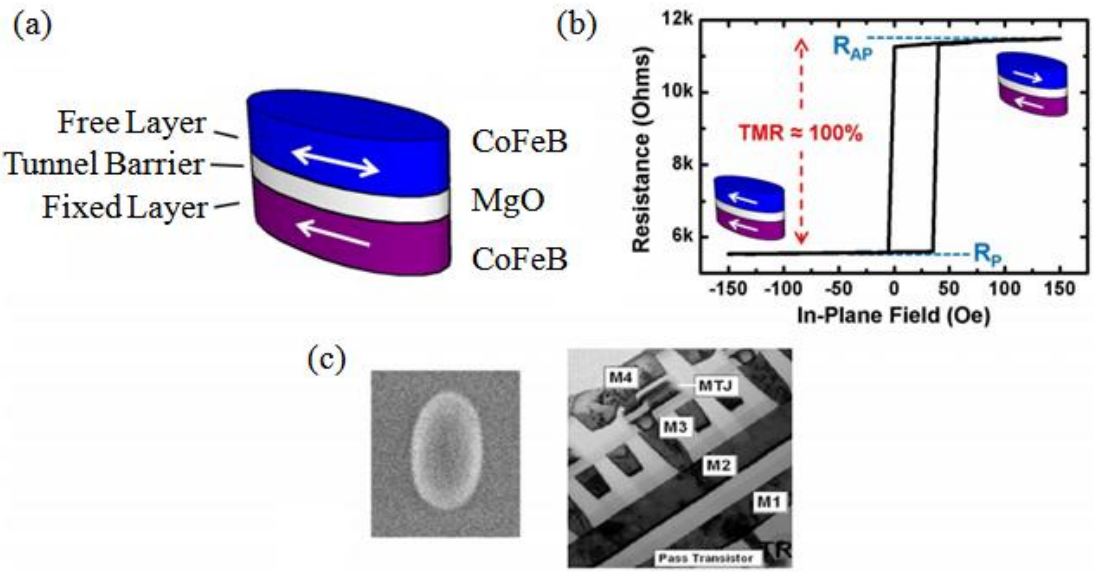

Figure 1-26. (a) Schematic of an MTJ device composed by two ferromagnetic materials (free and fixed layers) separated by a tunneling barrier. The most common combination so far is the CoFeB/MgO/CoFeB stack. (b) The TMR effect serves as the read-out mechanism in MTJ devices. The resistance changes from a minimum (R_P) to a maximum value (R_{AP}) when the free layer changes from being parallel to antiparallel to the fixed layer. This figure shows a typical experimental R-H curve with a TMR ratio close to 100% for a 150 × 70 nm^2 MTJ device. (c) MTJ can be integrated to conventional semiconductor electronics as part of the BEOL processes (Alzate 2014).

For memory application, the "0" and "1" information is stored as the relative magnetization alignment of the free layer with respect to the fixed layer in MTJ devices. There are two common configurations of the ferromagnetic layers: in-plane and perpendicular MTJ devices, as shown in Figure 1-27.

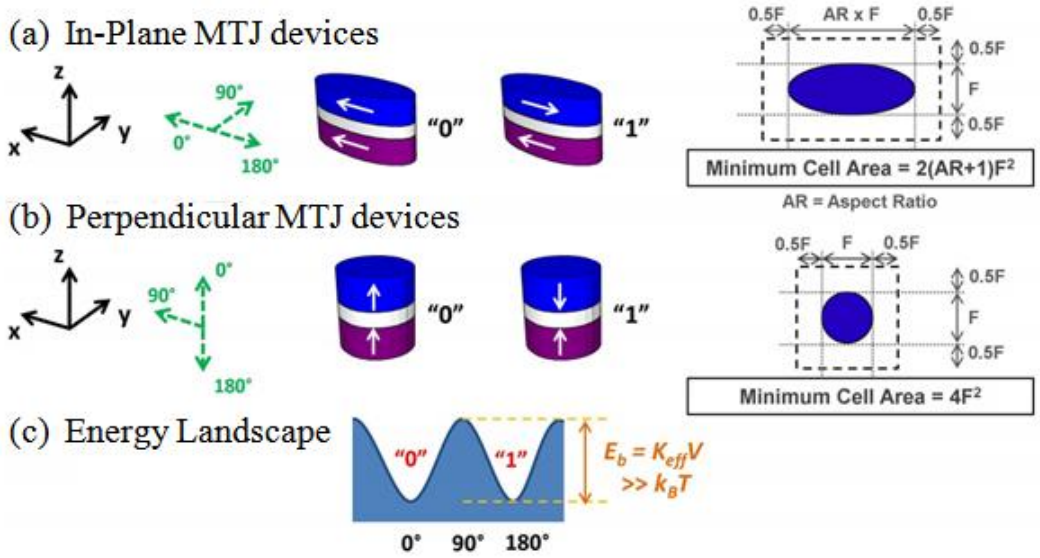

Figure 1-27. Schematic of the equilibrium conditions of the free layer of (a) in-plane and (b) perpendicular MTJ devices. (c) In each case, the magnetization has two in-plane or perpendicular equilibrium states at 0° and 180°, separated by an energy barrier at the hard-axis of 90° (Alzate 2014).

The in-plane MTJ devices exploit the ellipsoidal shape in order to create the two equilibrium states, which also results in a larger area (i.e. larger memory density area) because it is dependent on the aspect ratio (AR) of the ellipse (Alzate 2014). Therefore, to further scale the devices and increase the integration density, the perpendicular MTJ devices are required.

Present MRAM devices typically utilize current-controlled switching of magnetization via the spin transfer torque (STT) (Slonczewski 1996; Myers, Ralph et al. 1999) or spin-orbit torque (SOT) (Miron, Garello et al. 2011; Liu, Lee et al. 2012) effects to write information into magnetic bits. However, a fundamental challenge of STT-MRAM is scalability with respect to memory density and energy efficiency, as shown in Figure 1-28.

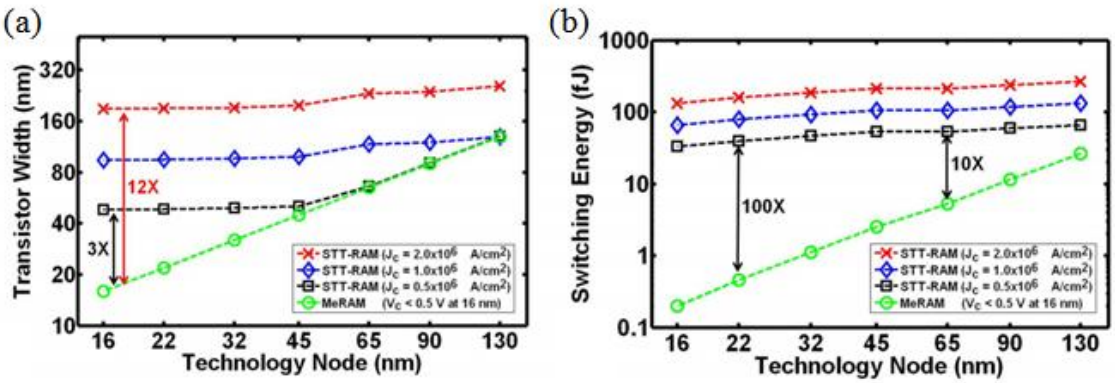

Figure 1-28. Comparison of (a) transistor width scaling and (b) switching energy per bit for 1-transistor/1-MTJ STT-MRAM and MeRAM cells across technology nodes down to 16 nm, for three different values of STT-MRAM switching current densities (J_C) (Alzate 2014).

The use of currents results in a memory cell size (i.e. bit density) limitation due to the large size of the required access transistors (Dorrance, Alzate et al. 2013; Khalili and Wang 2015), and large dynamic switching energy due to Ohmic power dissipation. Therefore, there has been a great interest in using an applied voltage (instead of current) to manipulate magnetization of nanoscale MTJs, called magnetoelectric random access memory devices (MeRAMs). The electric-field effect, or the voltage-controlled magnetic anisotropy (VCMA) effect, is utilized to temporarily lower the interfacial perpendicular magnetic anisotropy (PMA) of the free layer during the writing operation, thus reducing the writing energy required to overcome the energy barrier between the two stable magnetization states (WANG and AMIRI 2012; Wang, Alzate et al. 2013).

A promising type of electric-field-controlled memory device has been realized in perpendicular magnetic tunnel junctions using the Ta/CoFeB/MgO material system, where both high tunneling magnetoresistance (Ikeda, Miura et al. 2010; Khalili Amiri, Zeng et al. 2011) and VCMA-induced magnetization switching (Alzate, Amiri et al. 2012; Kanai, Yamanouchi et al.

2012; Shiota, Nozaki et al. 2012; Wang, Li et al. 2012) have been demonstrated. A summary of reported theoretical and experimental VCMA coefficients in literature is shown in Figure 1-29.

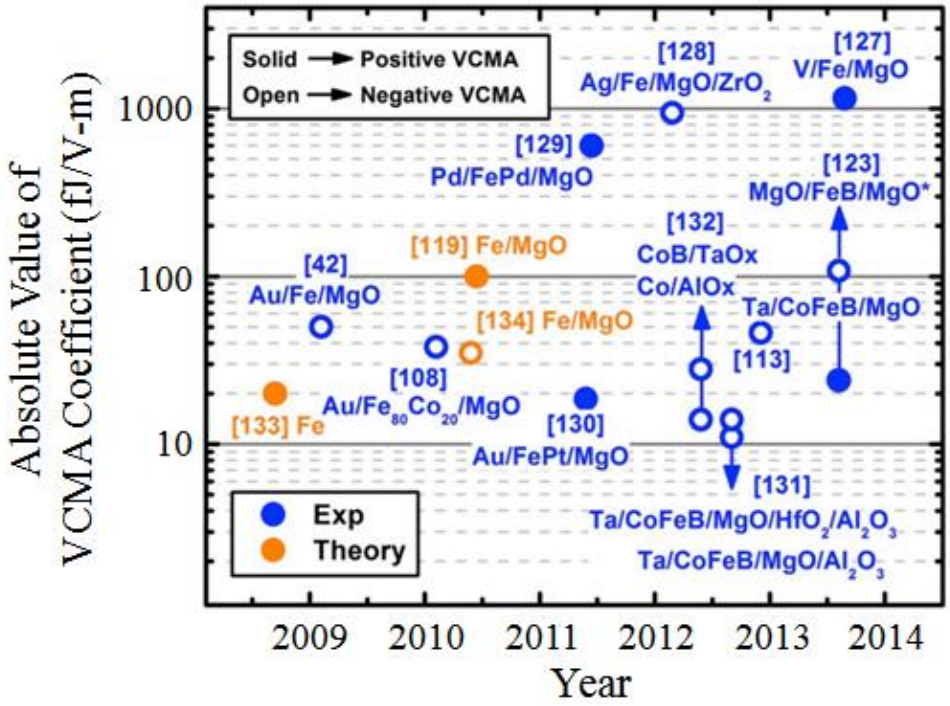

Figure 1-29. Summary of theoretical and experimental value of the VCMA coefficients ξ reported in literature for different material systems. "Positive VCMA" is defined as when the accumulation of negative charges near the ferromagnetic/oxide interface increases the perpendicular anisotropy; meanwhile a "negative VCMA" requires a depletion of negative charges to increase the perpendicular anisotropy (Alzate 2014).

For memory devices suitable for scaling below 32 nm, VCMA coefficients larger than 200 fJ/V-m are needed, as shown in Figure 1-30 for thermal stability factor of $\Delta = 40$ of retention time of 10 years (Alzate 2014; Khalili Amiri, Alzate et al. 2015). The thermal stability factor, Δ, is proportional to the energy barrier between the free ferromagnetic layer states and depends on the required retention time.

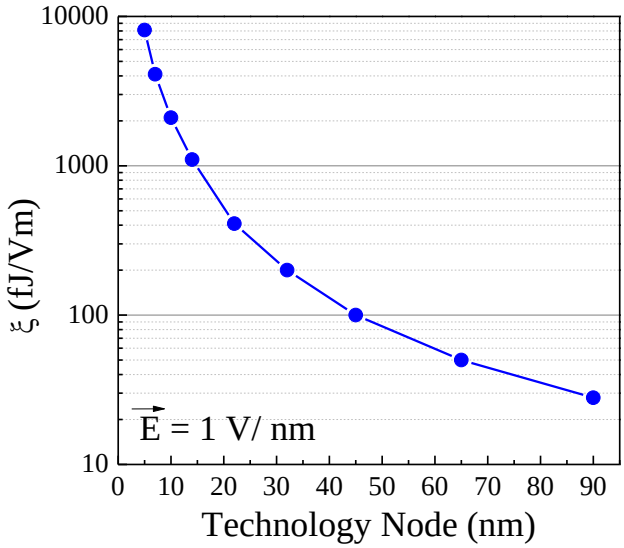

Figure 1-30. Scaling of the VCMA coefficient ξ across technology nodes for thermal stability factor, Δ = 40, of retention time of 10 years, revised from (Khalili Amiri, Alzate et al. 2015).

However, the traditional Ta/MgO/CoFeB system offers limited VCMA in the range of 10-60 fJ/V-m (Endo, Kanai et al. 2010; Liu, Pai et al. 2012; Zhu, Katine et al. 2012; Shiota, Bonell et al. 2013; Alzate, Amiri et al. 2014; Okada, Kanai et al. 2014). Therefore, it is essential to synthesize perpendicular MTJ devices with larger VCMA coefficients for future ultra-low power, non-volatile MeRAM devices.

1.3.1 Enhanced VCMA Effect with High-K Tunnel Barrier

To achieve a larger VCMA effect, multiple approaches have been explored, such as using different seed and cap layers adjacent to the ferromagnetic layer (Kubota, Ishibashi et al. 2012; Rajanikanth, Hauet et al. 2013; Shiota, Bonell et al. 2013; Skowroński, Nozaki et al. 2015). *Ab initio* electronic structure calculations have revealed that epitaxial strain has a dramatic effect on VCMA leading to giant magnetoelectric coefficient coefficients (Ong, Kioussis et al. 2015).

Another promising method to enhance the VCMA effect is by utilizing different dielectrics. As the VCMA effect originates from the charge accumulated at the CoFeB/oxide interface when voltage is applied (Maruyama, Shiota et al. 2009), using a single oxide or multiple layers of oxides with higher dielectric constant(s) (*K*) can induce a higher VCMA coefficient, thus a reduction of voltage for magnetization switching. Indeed, an enhanced VCMA effect has been measured in CoFeB/oxide structures using MgO/Al_2O_3 and $MgO/HfO_2/Al_2O_3$ as the gate oxide, as shown in Figure 1-31 (Kita, Abraham et al. 2012).

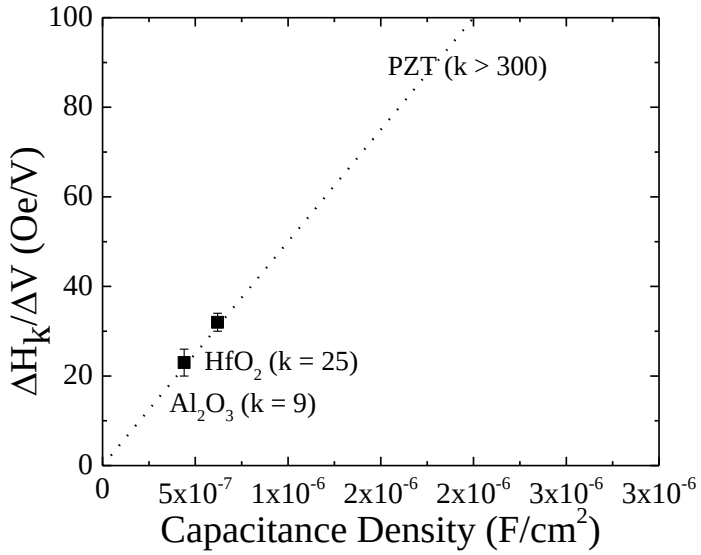

Figure 1-31. Relationship between the voltage dependence of the saturation field ($\Delta H_k/\Delta V$) and the electrical capacitance density for two kinds of stacks: $Co_{0.6}Fe_{0.2}B_{0.2}$ (12 Å)/MgO (10 Å)/Al_2O_3 (100 Å) and $Co_{0.6}Fe_{0.2}B_{0.2}$ (12 Å)/MgO (10 Å)/HfO_2 (70 Å)/Al_2O_3 (20 Å), and projection of PZT, revised from (Kita, Abraham et al. 2012).

However, in the work published by Kita *et al.*, the VCMA effect was measured from polar Kerr effect without fabrication of a full MTJ (Kita, Abraham et al. 2012), thus lacking a reliable electrical readout. There has been intensive research on MTJs using a high-*K* tunnel barrier other than MgO. However, MTJs using $SrTiO_3$ with CoFe electrodes possess rather low

TMR around 10% (Hassen, Viala et al. 2012), while multiferroic tunnel junctions with ferroelectric barriers such as PZT and $BaTiO_3$ with Co/Fe and LSMO electrodes only demonstrate TMR below room temperature (Garcia, Bibes et al. 2010; Pantel, Goetze et al. 2012). Therefore, to achieve better writing efficiency with reliable readout for voltage-controlled MRAM, it is critical to ensure a sizeable room temperature TMR after integration of oxide(s) with high-*K* into the tunnel barrier.

In this work, a novel method is used to integrate an ultra-thin layer of high-dielectric constant lead zirconate titanate (PZT or $Pb(Zr_xTi_{1-x})O_3$) thin film into the MgO tunnel barrier to enhance the VCMA effect while maintaining a sizeable TMR. Due to the fact that TMR can be greatly affected by the MTJ thin film roughness (Shen, Mazumdar et al. 2006), it is essential to have conformality and control over the roughness of the ultra-thin film; additionally, the film material need to have a higher dielectric constant than MgO that is 10 at bulk value (Robertson 2004). Therefore, PZT was chosen as the ultra-thin film (with thickness of 1.5 nm) to be integrated into the MTJ because it has one of the largest dielectric constant (300-1300 for 1-3 μm PZT thin films) (Ledermann, Muralt et al. 2003; Trolier-McKinstry and Muralt 2004) and it has been demonstrated that it can be deposited via atomic layer deposition (Zhang, Perng et al. 2011; Choi, Zhang et al. 2013), providing the capability to grow a conformal ultra-thin film with precise control over composition and thickness (George 2010).

1.4 Scope and Organization

The motivation to study ALD PZT thin film and multiferroic nanocomposites, and the various factors that affect the thin film properties are explained. Understanding these factors is important because it allows one to tune the processing parameters to optimize the film's

performance for specified applications. In Chapter 2, the experimental setups used in the proposed work are described. The chemistries required to synthesis ALD PZT films and multiferroic nanocomposites are defined. The various measurement techniques to characterize the material, dielectric, ferroelectric, and piezoelectric properties of the PZT thin film and the multiferroic nanocomposites are also detailed. In Chapter 3, results are shown and discussed for ALD PZT thin films on various substrates. In Chapter 4, the magnetoelectric effect is observed in multiferroic nanocomposites of ALD PZT coupled with templated mesoporous cobalt ferrite. In Chapter 5, an enhanced voltage-controlled magnetic anisotropy is measured in magnetic tunnel junctions with an MgO/PZT/MgO tunnel barrier. In Chapter 6, the overall thesis is summarized.

CHAPTER 2. EXPERIMENTAL SET-UP

In this chapter, the experimental setup that was used in this work are detailed. First, the reactor for ALD PZT film growth is described, followed by the synthesis of the PZT thin films and multiferroic nanocomposites. Second, the various measurement techniques that are to be utilized for characterizing the PZT thin films and multiferroic nanocomposites are described.

2.1 ALD PZT Reactor

Atomic layer deposition of PZT on small sample sizes of 1 cm × 1 cm were synthesized in the ALD PZT reactor with a sample temperature of 250°C using a substrate heater, shown in Figure 2-1, a low-vacuum reactor with a mechanical pump to maintain a base pressure of 100 mTorr.

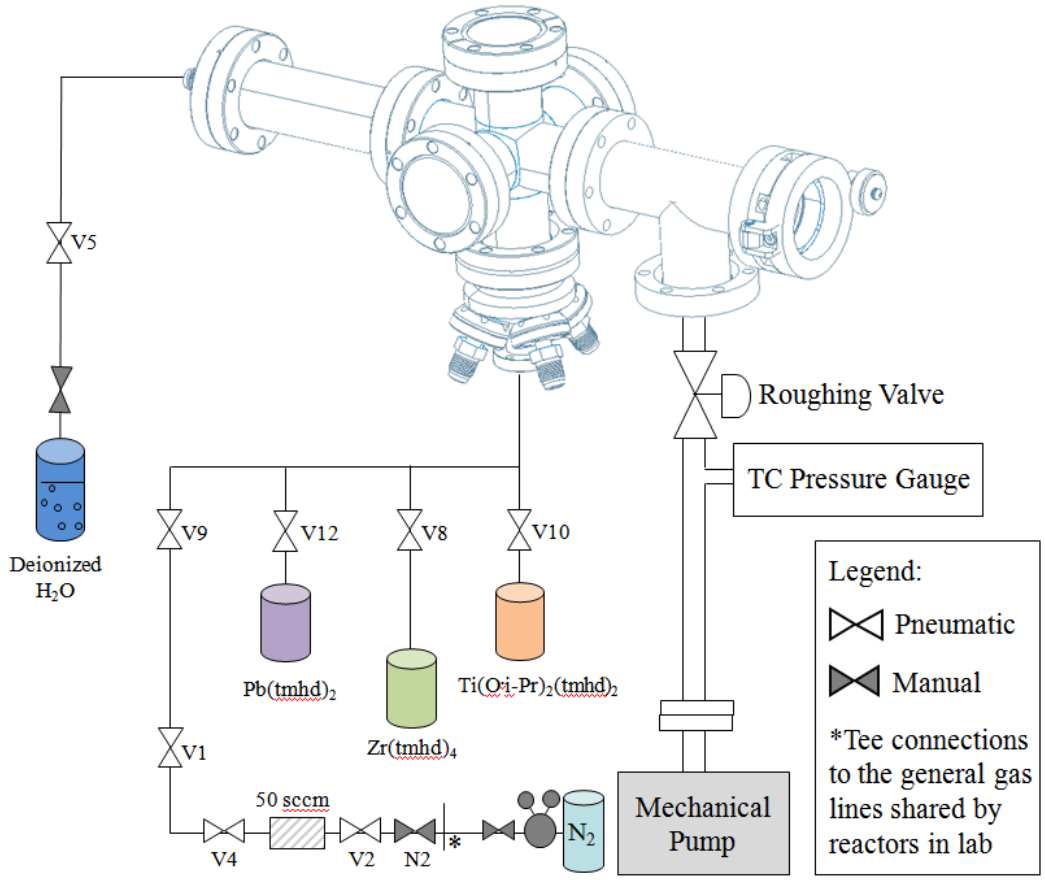

Figure 2-1. Schematic of a customized ALD PZT reactor.

The ALD PZT reactor consisted of a 2.75" six-way cross as the chamber in which the deposition process was performed. The front 2.75" conflat flange had a tee, which had the load lock door attached to one end and the manual angle valve to the mechanical pump attached to the other end. The reactor was wrapped with heating wires to maintain a chamber wall temperature of 100^{o}C. Superwool blankets and aluminum foil were used to insulate the chamber to minimize heat loss during processing. The lead, zirconium, and titanium precursors were attached to the bottom of the six-way cross through a multiport flange containing five of 1.33" ports. Similar to the chamber, the precursors were heated by a couple of heating wires for each source and wrapped in superwool blankets and aluminum foil for insulation. The temperature of the heating wires for the chamber and precursors were controlled by temperature controllers, which ensureed that the temperature set point was reached and maintained during deposition. An inert nitrogen gas line was attached to the bottom of the chamber through one of the 1.33" ports. A deionized water source, the oxidizing agent, was attached to the conflat flange in the back of the six-way cross chamber through a VCR adaptor. The ALD PZT deposition was fully automated and the deposition sequence was programmed and ran in Labview. By automating the systems, films with different thicknesses were synthesized and processing conditions were ensured to be kept consistent from one deposition to another.

To study the scalability of ALD PZT deposition onto large area wafers, the PZT small scale reactor was modified to accommodate the PZT large scale reactor, as shown in Figure 2-2.

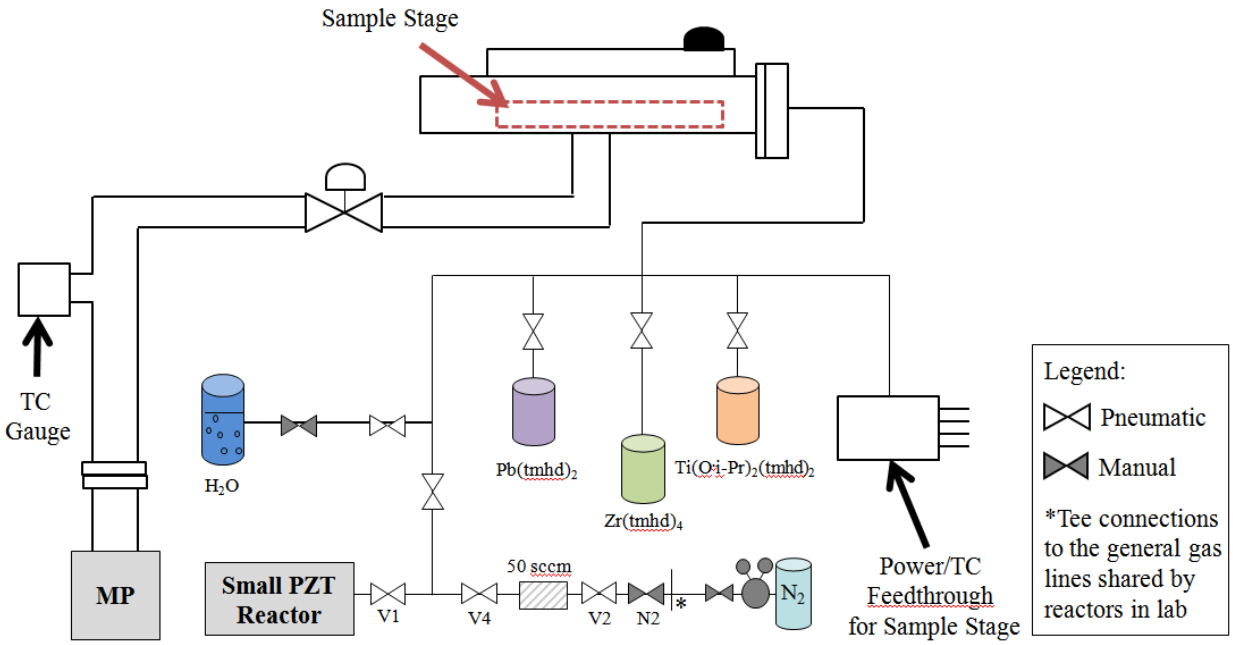

Figure 2-2. Schematic of modified PZT large scale reactor with multiport precursor delivery system.

In order to scale the PZT reactor to process large wafers, a customized rectangular entry load lock was attached to the top 2.75" conflat flange of the 6 way cross of the PZT small scale reactor. The large scale load lock had two 2.75" conflat ports – one on the side and the other on the bottom. The port on the side of the load lock was used to attach the load lock to the PZT small scale chamber by a 90 degree elbow. The port on the bottom of the load lock was used for pumping in order to keep the rectangular entry load lock under vacuum during deposition and to remove any reactive by-products in between the precursor pulses. The rectangular port of the load lock was fitted with a customized flange with a multiple precursor delivery system to ensure more efficient supply and control of the precursor delivery. This allowed the precursors to flow across the wafer surface for uniform deposition. The rectangular flange had five 1.33" half nipple ports on the center line. Each of the miniports was connected to one precursor, for a maximum of five sources. The wafer was mounted on a customized 8-inch diameter resistive-

wire heating heater and heating stage which sat on the bottom of the large scale load lock, as shown in Figure 2-3.

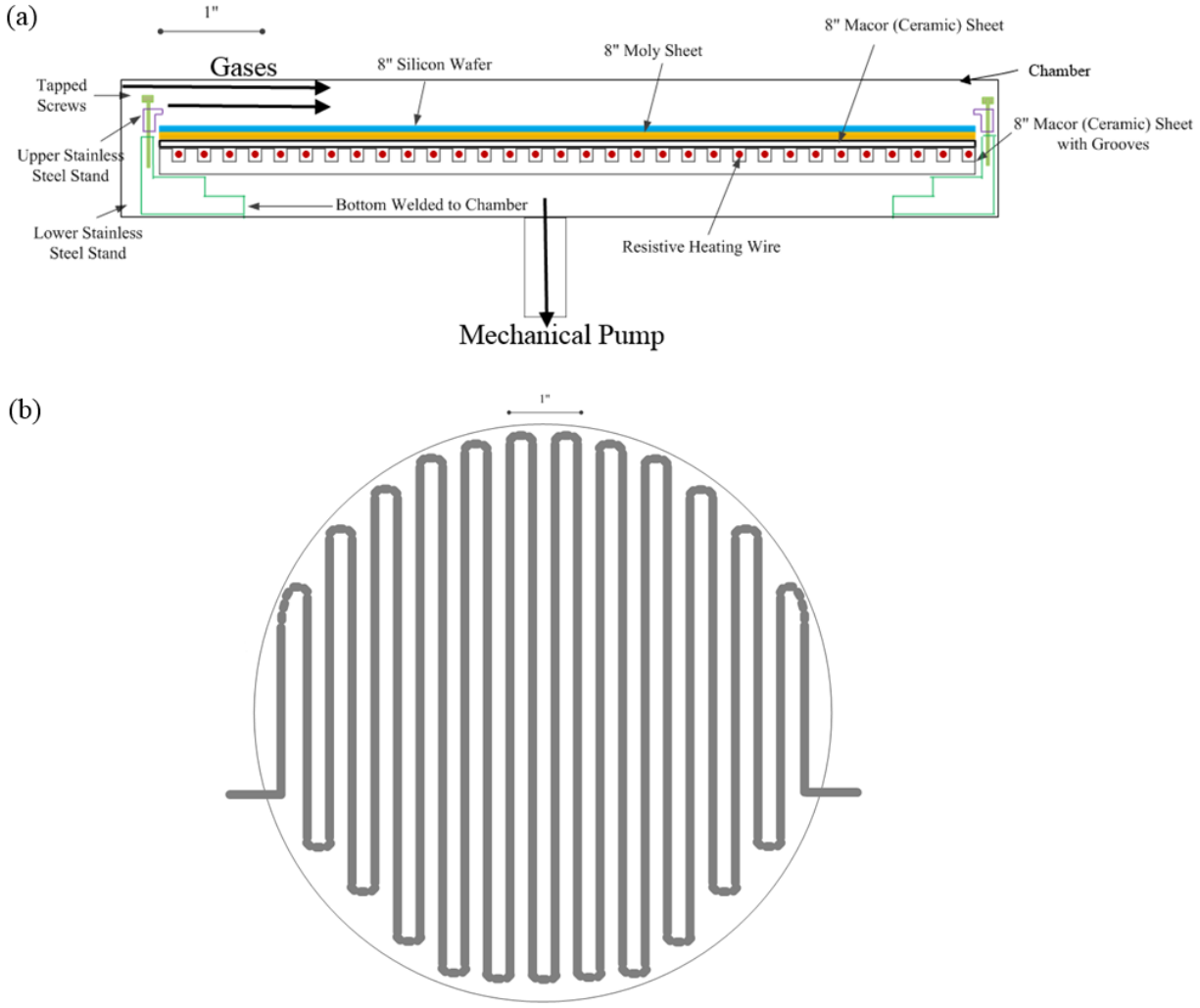

Figure 2-3. Customized 8-inch diameter heater and stage: (a) cross-sectional view and (b) 8" Macor sheet with grooves for the resistive heating wire.

The deposition sequence was programmed in Labview. By automating the systems, thicker films were obtained while ensuring conditions were kept consistent from one deposition to another.

2.2 ALD PZT Thin Film Growth and Processing Conditions

For PZT thin film growths in this work, the substrate surface was heated to ~250^{o}C (Zhang, Perng et al. 2011) and all the metal precursors are beta-diketonates (Choi, Zhang et al. 2013). Lead bis (2,2,6,6-tetramethyl-3,5-heptanedionato) [$Pb(C_{11}H_{19}O_2)_2$, $Pb(TMHD)_2$], titanium diisopropoxidebis (2,2,6,6-tetramethyl-3,5-heptanedionato) [$Ti(O{\cdot}i\text{-}C_3H_7)_2(C_{11}H_{19}O_2)_2$, $Ti(O{\cdot}i\text{-}Pr)_2(TMHD)_2$], and zirconium tetrakis (2,2,6,6-tetramethyl-3, 5-heptanedionato) [$Zr(C_{11}H_{19}O_2)_4$, $Zr(TMHD)_4$] were used as the Pb, Ti, and Zr precursors, respectively, as listed in Table 2-1. The lead, zirconium, and titanium solid precursors were stored in individual stainless steel housings and heated to its vapor phase for atomic layer deposition (ALD). Deionized water vapor was used as the oxygen source for the oxide.

Table 2-1. Main parameters of precursors used in this work, [1](Yamazaki, Tsuyama et al. 1992).

Chemical	Supplier	Vapor pressure	Thermal decomposition temperature	Melting temperature	Housing temperature
Deionized Water	UCLA	17.5 mm Hg (20^{o}C)	2000^{o}C	0^{o}C	20^{o}C
$Pb(TMHD)_2$	Strem Chemicals	0.1 mm Hg (134^{o}C)	280^{o}C[1]	126-128^{o}C	120^{o}C
$Zr(TMHD)_4$	Strem Chemicals	0.1 mm Hg (180^{o}C)	300^{o}C[1]	318-320^{o}C	190^{o}C
$Ti(O{\cdot}i\text{-}Pr)_2(TMHD)_2$	Sigma-Aldrich	1 mm Hg (150^{o}C)	248^{o}C[1]	171.1-184.6^{o}C	130^{o}C

In this work, one local cycle is defined as a pulse of metalorganic precursor, a pulse of nitrogen gas, pump-down time, a pulse of water, a pulse of nitrogen gas, and pump-down time. The number of local cycles for Pb, Ti, and Zr are denoted by *a*, *b*, and *c*, respectively, so the ratio of *a:b:a:c* represents the number and sequence of local cycles for each binary ALD process.

One global cycle of PZT was deposited in the sequence of *a*(Pb-O):*b*(Ti-O):*a*(Pb-O):*c*(Zr-O), as shown in Figure 2-4.

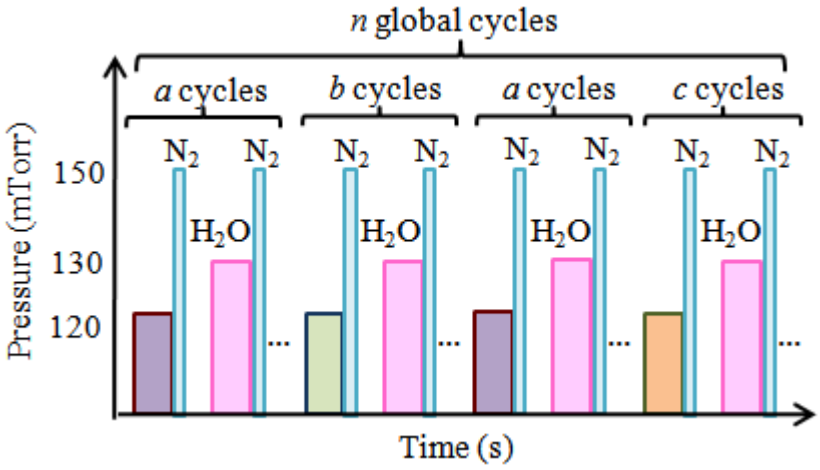

Figure 2-4. ALD sequence for PZT thin film growth that was used in this work.

The Pb-O, Ti-O, and Zr-O binary oxide growths were performed by alternating the organometallic precursor pulse and water vapor pulse separated by a nitrogen purge and pump-down steps to avoid vapor phase reactions and remove any remaining precursors, water, and/or by-products. For one global cycle of ALD $PbTiO_3$, the same binary Ti-O and Pb-O growths used for depositing PZT film were applied in the sequence of *a*(Ti-O):*b*(Pb-O) where the ratio of *a:b* represents the number of local cycles. The Ti-O was chosen to deposit first on platinized silicon substrate in order to avoid the temporary formation of a Pt_3Pb layer at the interface which has been found to promote (111) orientation (Trolier-McKinstry and Muralt 2004).

For ALD processes, the initial deposition rate of a material on a dissimilar surface is much slower than on itself. Termed as the incubation period, desired functional groups must be generated on the substrate surface to support the half reactions and reactions are mainly affected by the surface's conditions. Choi *et al.* quantified the incubation time of depositing one PZT constituent oxide on another by *in-situ* Fourier transform infrared spectroscopy (FTIR). First,

one constituent metal oxide film with thickness of 3 nm, to remove the substrate effect, was deposited on a KBr substrate as the starting surface. The IR absorption spectrum was acquired and served as the baseline for analysis. Next, another metal oxide was deposited and FTIR absorption spectra were collected after each ALD cycle until stretching vibration mode of the target metal oxide was observed. This indicated the required incubation time to initiate the target oxide growth. The results, as shown in Table 2-2, showed that the incubation period is 2 ALD cycles for TiO_2 on PbO, 3 cycles for PbO on TiO_2, 4 cycles for ZrO_2 on PbO, and 2 cycles for PbO on ZrO_2 (Choi, Zhang et al. 2013). By identifying the incubation time, the number of local cycles was known and was used as a guide to design and synthesize ALD PZT films with precise composition control.

Table 2-2. Incubation time of growing each PZT constituent oxide on another (Choi, Zhang et al. 2013).

Incubation cycle	On PbO	On TiO_2	On ZrO_2
PbO	1	3	2
TiO_2	2	1	2
ZrO_2	4	3	1

Because PZT and $PbTiO_3$ thin films were amorphous after ALD, they needed to be annealed to form crystalline films. PbO is generally volatile at high annealing temperatures so it is common to deposit films with excess lead content (Trolier-McKinstry 2008). For best performance, post-annealed PZT film should have composition of Zr/Ti = 52/48 and be (001) oriented (Trolier-McKinstry 2008). Therefore, optimization of deposition conditions (e.g. housing temperatures, ratio of local cycles) and annealing conditions (e.g. temperature, time, environment, ramp rate) for $PbTiO_3$ and PZT thin film growth were essential.

Due to diffusion problems, high quality PZT thin films could not be grown on silicon wafers without a buffer layer. For many applications, PZT must be deposited on an electrode which neither oxidizes nor insulates (Muralt 2000). Therefore, platinized silicon wafers ($Pt/TiO_2/SiO_2/Si$) from MEMS Exchange were used as substrates for ALD PZT thin films. A layer of 100 nm thick Pt (111) was sputtered on a layer of 35 nm thick TiO_2 that was sputtered and oxidized on a layer of 300 nm thick thermally grown SiO_2 on a Si wafer (Potrepka, Fox et al. 2011). Because PZT is controlled by nucleation growth and typically follows the substrate's orientation, a (001) textured $PbTiO_3$ seed layer was needed (Muralt 2000).

ALD PZT thin films were also grown on large 6-inch platinized silicon wafers to demonstrate the scalability of the ALD PZT process. Additionally, ALD PZT thin films were deposited on other substrates, which include La_2NiMnO_6 and La_2CoMnO_6 nanoparticles to synthesize core-shell multiferroic nanoparticles and silicon substrates for capacitance-voltage measurements.

2.3 Synthesis of PZT/CFO Multiferroic Nanocomposites

In order to engineer PZT/CFO nanostructured multiferroic composite with a 0D-3D geometry, the mesoporous CFO matrix was made dip-coating into a solution of CFO precursors with diblock copolymers that formed micelles in order to create pores, as shown in Figure 2-5.

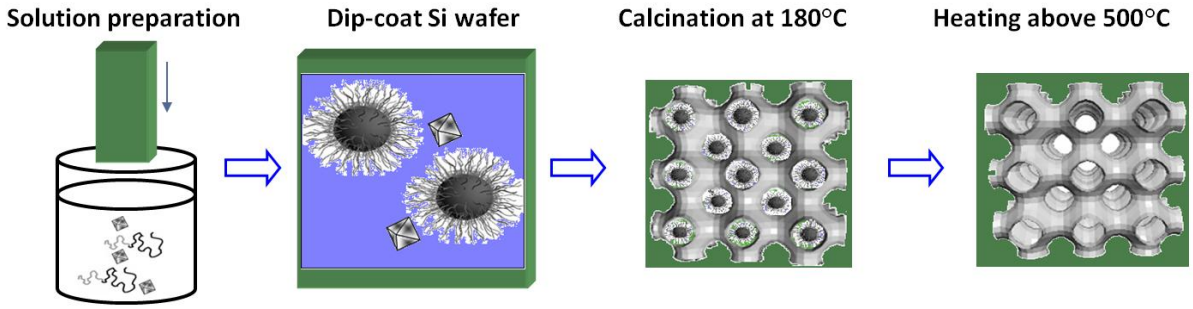

Figure 2-5. Schematic of mesoporous $CoFe_2O_4$ (CFO) matrix synthesis process.

The size and structure of the pores were dependent on the type of diblock copolymer used. The films were calcinated at 180°C and crystallized above 500°C. For this work, the diblock copolymer that was used to template the mesoporous CFO was PEP (PEP-PEO, poly(ethylene propylene)) and was annealed at 550°C with a slow cool rate (Quickel, Le et al. 2010), thus resulting in 100 nm thick mesoporous CFO with porosity of 30.42% with neck radius of 6 nm and pore radius of 9 nm.

ALD PZT thin films with varying thicknesses were deposited as an amorphous layer onto dense CFO films and into the mesoporous CFO matrix, then the samples were crystallized by rapid thermal annealing (RTA) at 700°C for 1 minute in an oxygen environment.

2.4 Synthesis of PZT Magnetic Tunnel Junctions

To form a PZT magnetic tunnel junction, a reference device with an MgO-only tunnel barrier must be fabricated and compared to devices with PZT incorporated into the tunnel barrier. The MTJ with the MgO tunnel barrier was used as the reference sample and compared to the MTJ with the MgO/PZT/MgO tunnel barrier (hereafter called MgO MTJ and PZT MTJ, respectively). Sample structures are schematically illustrated in Figure 2-6.

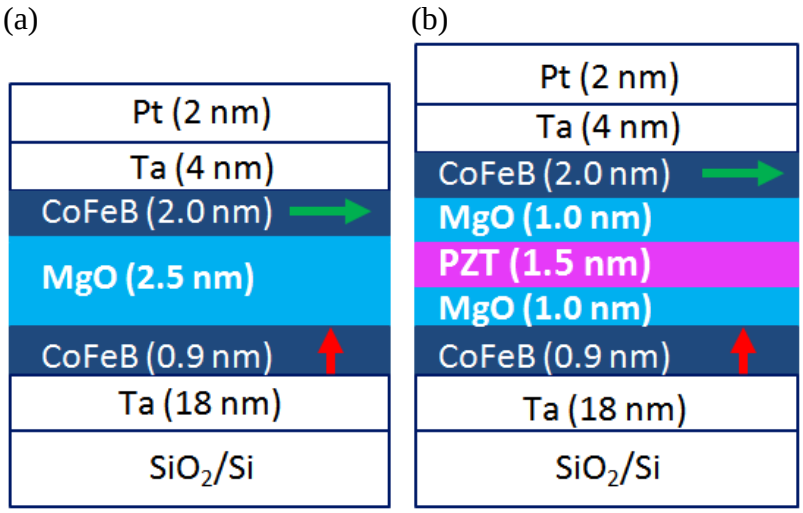

Figure 2-6. Magnetoelectric tunnel junction schematics of (a) MgO MTJ as the reference, and (b) PZT MTJ with MgO/PZT/MgO tunnel barrier. Devices measured had elliptical dimensions of 4 μm × 16 μm and 4 μm × 12 μm. Arrows show the magnetic anisotropy of the CoFeB top fixed layer (in-plane) and bottom free layer (perpendicular).

The stacks were deposited on thermally oxidized Si substrates using an AJA magnetron sputtering system and thermal atomic layer deposition. All metallic layers were DC sputtered under a pressure of 2 mTorr. First, an 18 nm thick Ta layer was deposited as the MTJ bottom electrode. A $Co_{20}Fe_{60}B_{20}$ free layer with thickness of 0.9 nm, chosen to be out-of-plane (i.e. perpendicular to the substrate plane) magnetically anisotropic, was then sputtered on the Ta layer (Ikeda, Miura et al. 2010). For the MgO MTJ, a 2.5 nm thick MgO tunnel barrier was grown by RF sputtering from an insulating MgO target at 2 mTorr. While for the PZT MTJ, a 1.0 nm thick MgO layer was first sputtered, then a 1.5 nm thick PZT film was deposited via ALD at substrate temperature of 250°C, and finally a 1.0 nm thick MgO was sputtered to form the MgO/PZT/MgO tunnel barrier. A 2.0 nm thick $Co_{20}Fe_{60}B_{20}$ fixed layer, chosen to be in-plane (i.e. parallel to the substrate plane) magnetically anisotropic, and capping layers of 4 nm thick Ta and 2 nm thick Pt were then sputtered on top of the tunnel barrier for both MTJs. The PZT MTJ film stack was annealed at 200°C for 30 minutes under vacuum (< 10^{-7} Torr) before the PZT

deposition and after depositing the entire film stack. Note that the PZT MTJ film stack was also *in situ* annealed during the ALD process under 250°C for 1 hour, hence, we annealed the MgO MTJs at 250°C for 30 minutes for a fair comparison. MTJ devices with elliptical diameters of 4 μm × 16 μm and 4 μm × 12 μm were subsequently fabricated using standard photolithography and reactive ion etching (RIE) techniques.

2.5 Thin Film Characterization and Experimental Techniques

ALD-deposited PZT thin films and multiferroic nanocomposites were characterized with respect to their morphology, surface chemistry, electric, and magnetic properties by various techniques that are detailed below.

2.5.1 Ellipsometry

The morphology of the thin film was characterized in terms of its thickness and surface roughness. Ellipsometry is a noninvasive, nondestructive, and very sensitive surface and thin film measurement technique that uses the difference in polarization between the incident and reflected polarized light at the interface to determine the thickness of a material, as shown in Figure 2-7.

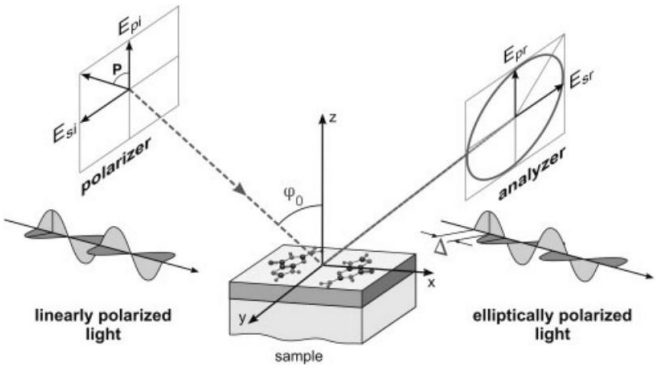

Figure 2-7. Schematic representation of the ellipsometric principle. The incident light is linearly polarized; the elliptically polarized reflected light is described by the relation between the measured quantities of amplitude ratio, ψ, and phase change, Δ (Gruska and Hinrichs 2011).

The sample must be uniformly smooth in order to reflect the linearly polarized incident light and become elliptically polarized light due to the sample's properties. The change in polarization (p) is defined as:

$$p = \tan(\psi)e^{i\Delta} \tag{2-1}$$

where ψ is the amplitude ratio and Δ is the phase change. Ellipsometry is an optical technique requiring an accurate model to analyze the measured data, which means that optical constants of the substrate and sample layers and the thickness of the layers are critical in obtaining precise measurements. The optical constants are represented by a complex refractive index, $\tilde{n}$:

$$\tilde{n} = n + ik = \sqrt{\tilde{\varepsilon}} \tag{2-2}$$

where n is the index of refraction, k is the extinction coefficient, and $\tilde{\varepsilon}$ is the complex dielectric function (Woollam Co.). Although there are published optical constant sets for various materials available for usage, some materials have been found to exhibit a range of optical constants depending on the deposition process. Therefore, the models used in this work for the platinized silicon substrate and the ALD $PbTiO_3$ seed layer were first experimentally obtained with

assistance from J.A. Woollam Co. For example, the ALD $PbTiO_3$ seed layer is fitted by a Cauchy dispersion model of:

$$n(\lambda) = A + \frac{B}{\lambda^2} + \frac{C}{\lambda^4} \tag{2-3}$$

where the fitting parameters are A = 2.66, B = 0.01, and C = 0.00 (Woollam Co.).

An ex-situ spectroscopic ellipsometer, the J.A. Woollam M-88 rotation analyzer spectroscopic ellipsometer, was used to measure ψ and Δ over the wavelength range of 280.5-766.1 nm at a fixed angle of 75^o, which was then fitted by models using the WVASE 32 software to determine the thickness of deposited thin films. The optical constants and models are shown in Table 2-3.

Table 2-3. Optical constants of models used for the PZT, $PbTiO_3$, and Pt films, where *n* are the index of refraction and *k* is the extinction coefficient.

	n_{min}	n_{max}	k_{min}	k_{max}	Model name
PZT	2.4792	3.03	0.0035	0.0867	pzt_film.mat
$PbTiO_3$	2.67	2.7416	0	0	pbtio3_cauchy_130127.mat
Pt	1.2828	3.7189	2.8906	7.6495	pt_memsexchange.mat

A typical set of experimental data and fitted model measured by the ellipsometer for a sample with ALD PZT thin film deposited on Pt is shown in Figure 2-8.

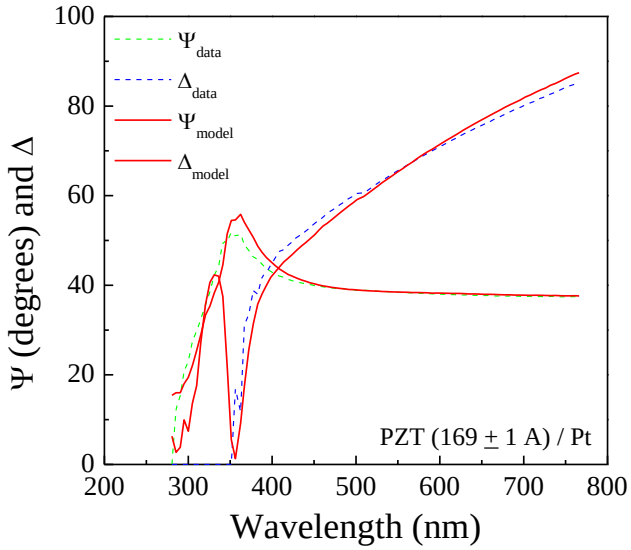

Figure 2-8. Data and model fit for ψ and Δ of 17 nm thick PZT on Pt sample measured via ellipsometer.

2.5.2 X-ray Photoelectron Spectroscopy

The composition of ALD PZT thin film was determined by X-ray photoelectron spectroscopy (XPS). XPS is a surface analysis technique and measurements are taken by irradiating the surface with an X-ray beam and assessing the kinetic energy and number of escaping electrons from the top ~10 nm of the surface. The kinetic energies of the atomic orbital from which the ejected electron originates (*KE*) are measured, and the counts per second (CPS)-binding energy (*BE*) curve is plotted based on the following equation:

$$BE = h\nu - KE - \phi_s \tag{2-4}$$

where the x-ray energy ($h\nu$) and spectrometer work function (ϕ_s) are known. By analyzing the binding energy and comparing it to literature, the specific atom and orbital can be determined for each peak. In order to correct for surface charges, the C *1s* peak at 284.6 eV was used as the

reference. The stoichiometry of the PZT film can also be calculated through XPS data by using the following expression:

$$C_x(\%) = \frac{I_x / S_x}{\sum I_i / S_i} \times 100\% \tag{2-5}$$

where C_x, I_x, and S_x are atomic percentage, integrated area of CPS-BE curve, and atomic sensitivity factor of element *x*. Table 2-4 summarizes the atomic sensitivity factors used in the work for analyzing XPS data.

Table 2-4. List of atomic sensitivity factors used in this work for Kratos XPS equipment.

Element	Level	S_i
Pb	4f	8.329
Zr	3d	2.576
Ti	2p	2.001
C	1s	0.278
O	1s	0.780

Typical survey and detail scans are obtained by the Kratos XPS Axis Ultra DLD and analyzed with CasaXPS software, as shown in Figure 2-9.

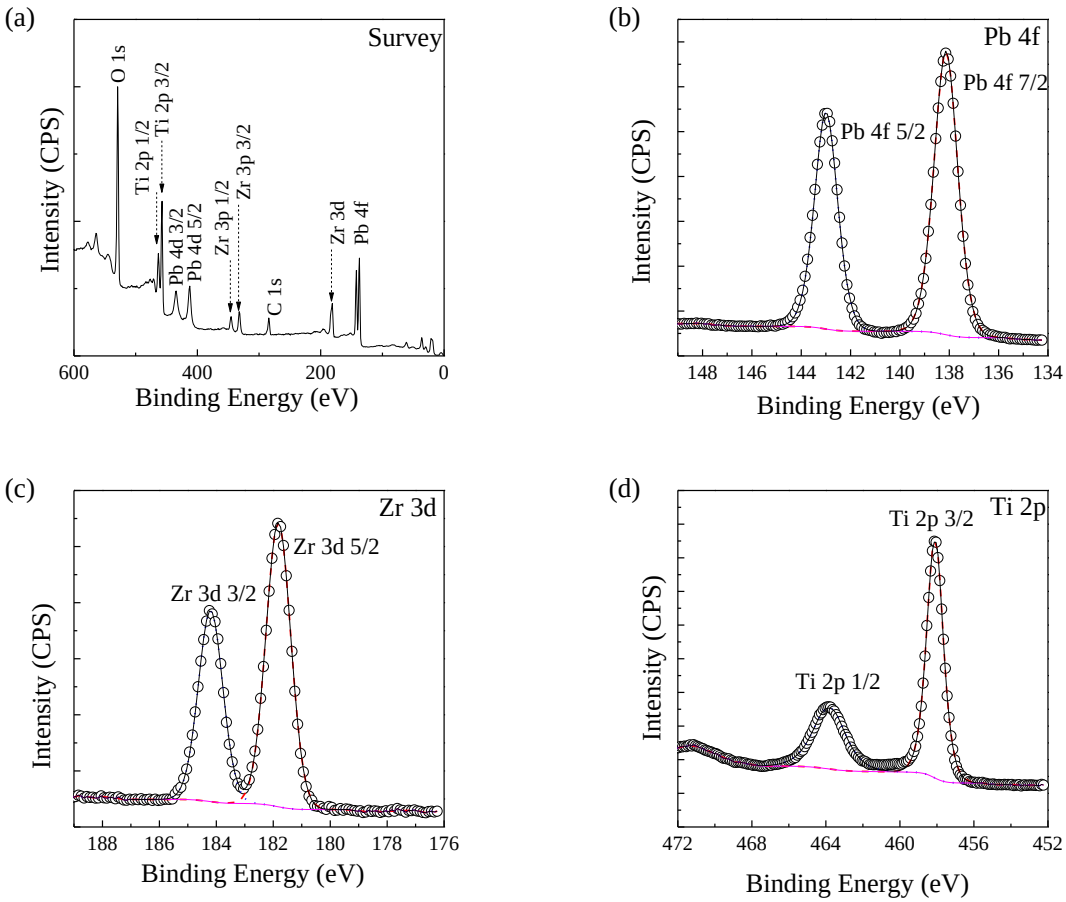

Figure 2-9. Experimental and analyzed XPS scans of 46.4 nm thick PZT film on a Si substrate: (a) survey scan from 600-0 eV, (b) Pb 4f scan from 149-134 eV, (c) Zr 3d scan from 189-176 eV, and (d) Ti 2p scan from 472-452 eV.

For data analysis, the first step was to calibrate all survey and detail peaks to the reference peak of C *1s* at 284.6 eV. Next, the background was fitted using the Shirley algorithm, which uses an iterative procedure to use information provided by the spectrum to construct a background sensitive to the data. The peaks were then fitted using the Gaussian Lorentzian function in order to determine the integrated intensity area of each peak. As shown in Equation (2-5), the integrated intensity area was then divided by the atomic sensitivy factor, as listed in Table 2-4, to find the atomic percentage of each peak in order to determine the stoichiometry of the film. While fitting the peaks, it was important to constrain the area of the relative intensities

from the doublet states, thus for *p* electrons the relative intensities were 1:2, while for *d* electrons the doublet pairs were in the proportion 2:3, and for *f* electrons the ratio was 3:4 (Ltd. 2006).

2.5.3 X-ray Diffraction

After annealing the amorphous thin films, the crystallinity was assessed via X-ray diffraction (XRD) by comparing the peaks found in the 2-theta scan to Joint Committee on Powder Diffraction Standards (JCPDS) files, as listed in Table 2-5.

Table 2-5. List of materials and the JCPDS reference codes that were used in this work.

Materials	JCPDS Reference Code
PZT	00-033-0784
$PbTiO_3$	01-070-0746
$PbZrO_3$	00-035-0739
PbO	00-038-1477
ZrO_2	00-037-1484
TiO_2	00-021-1276
Pt	00-004-0802
SiO_2	00-005-0490
Si	00-027-1402
CFO	00-001-1121

Diffraction is a scattering phenomenon. Atoms scatter x-rays in all directions, but when the atoms are in a lattice the x-rays in certain directions undergo constructive interference and form diffracted beams. Therefore, a unique diffraction pattern is created due to the interaction between the entering x-ray beam and the periodically arranged atoms in the material. Relation between the transmitted x-ray beam and crystal structure is known as Bragg's Law:

$$n\lambda = 2d\sin\theta \tag{2-6}$$

where n is an integer representing the order of diffraction, λ is the incoming x-ray wavelength, d is the distance between adjacent planes, and θ is the Bragg angle and measured between the incident beam and a crystal plane. Therefore, by knowing the x-ray wavelength, the crystal

planes can be identified by the measured value of θ for first-order reflection when $n = 1$ (Cullity and Stock 2001). A typical XRD spectrum of an 8.1 nm thick ALD PZT deposited on platinized silicon substrate that was rapidly thermally annealed at 700^{o}C for 1 minute in oxygen ambient is shown in Figure 2-10.

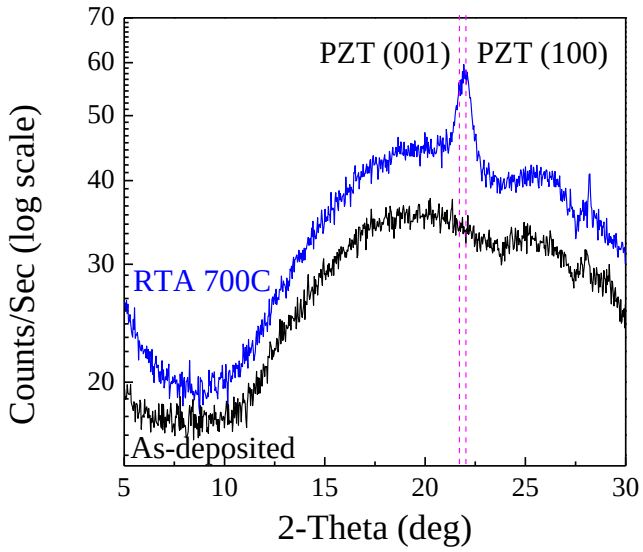

Figure 2-10. XRD of 8.1 nm thick ALD PZT/Pt, as-deposited (amorphous film) versus annealed film (crystallized film and observed PZT (001) and (100) peaks).

By fitting the XRD peak with the Pseudo-Voigt function, the peak center is determined to be at 21.92° and the full-width-half-maximum (FWHM) is 0.87°, which corresponds to the PZT (100) peak at 22.01° given by the JCPDS reference code. For XRD measurements, the Bruker D8 Discover Powder X-ray Diffractometer, Panalytical X'Pert Pro X-ray Powder Diffractometer, and Stanford Synchrotron Radiation Lightsource (SSRL) beamline 11-3 and 7-2 were used to determine the crystallinity of ALD PZT thin films. A typical XRD spectra taken at SSRL beamline 11-3 of an ALD PZT film sample is shown in Figure 2-11.

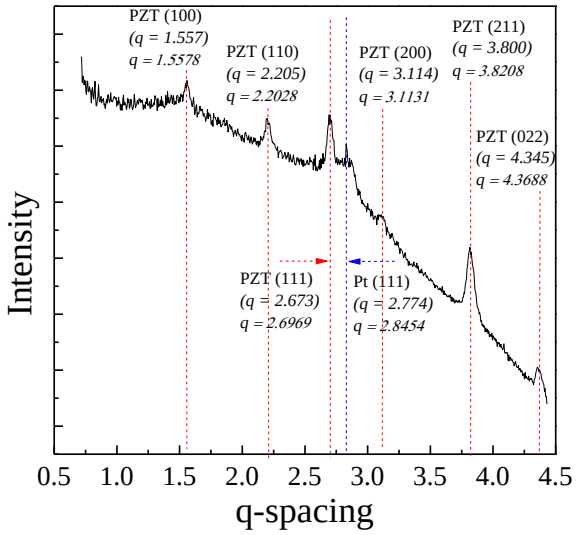

Figure 2-11. XRD spectra measured at SSRL beamline 11-3 of 6.4 nm thick ALD PZT thin film on Pt (111) substrate.

The XRD data taken at SSRL beamline 11-3 is taken as a function of q-spacing, instead of 2-theta, and is related to d-spacing by the following equation:

$$q = \frac{2\pi}{d} \tag{2-7}$$

where q is the q-spacing with the units of 1/Å and d is the d-spacing with the units of Å. The q-spacing is used because it is a convenient way to plot diffraction data independent of the wavelength used by the particular instrument.

2.5.4 SQUID

The ferromagnetic property of PZT/CFO thin film heterostructure was characterized by superconducting quantum interference devices (SQUID) magnetometer, as shown in Figure 2-12.

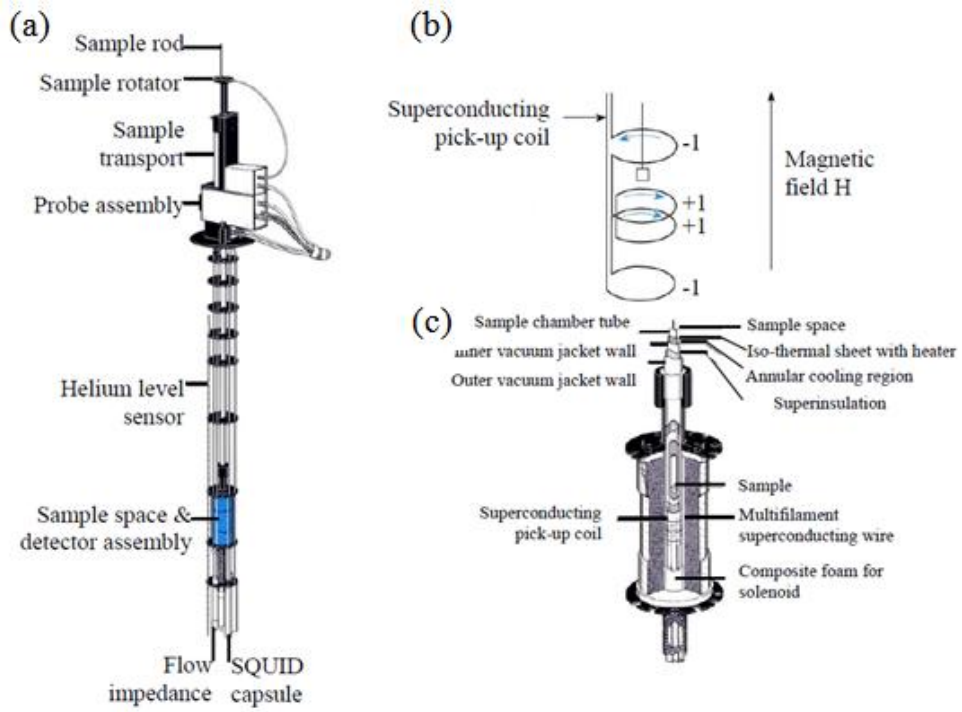

Figure 2-12. Schematic drawing of (a) a SQUID magnetometer, (b) a superconducting detection coil, and (c) SQUID detector (McElfresh 1994).

First observed by Heike Kamerlingh-Onnes in 1911, superconductivity describes the phenomenon when a material's electrical resistance decreases to zero below a critical temperature. To provide the necessary low temperature, a vacuum chamber cooled with liquid helium or liquid hydrogen is used. As a magnetic field is applied, maximum applied magnetic field being 5 Tesla (T) or 50,000 Oe, the sample is vertically moved through superconducting detection coils which are connected to the SQUID with superconducting wires. When there is a change of magnetic moment in the sample, the resulting change of magnetic flux in the detection coils is proportional to the change of current in the detection coil which is proportional to the change of output voltage in the SQUID. Therefore, the SQUID detector is an extremely sensitive current-to-voltage converter and provides a highly accurate measurement of the sample's magnetic moment (McElfresh 1994).

The 5 × 5 mm^2 sample is either placed vertically (parallel) or horizontal (perpendicular) in a diamagnetic straw to measure the magnetic property in the in-plane or out-of-plane direction, respectively. The straw is connected to the sample transport rod, which is used to move the sample through the detection coil. During the measurement at an applied magnetic field, the sample's voltage response is measured at discrete steps over the specified scan length, typically 6 cm. The measurement is repeated three times and averaged to improve the signal-to-noise ratio, as shown in Figure 2-13. The average magnetic moment at the applied magnetic field is then calculated by the iterative regression method, which fits the SQUID output signal using an iterative regression algorithm to accommodate any sample position offsets during the measurement scans (McElfresh 1994).

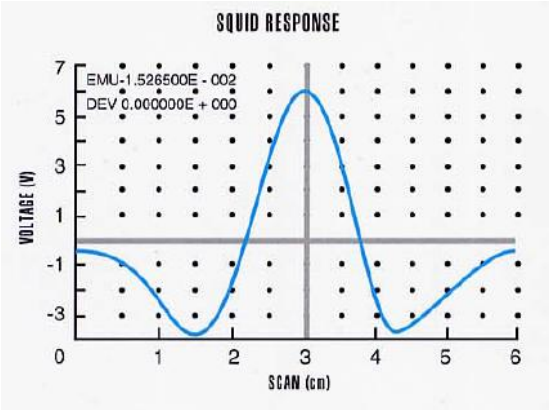

Figure 2-13. The output of the SQUID as a magnetic dipole is moved through the pickup coil. The vertical scale corresponds to an output voltage and the horizontal scale is sample position (McElfresh 1994).

By applying increasing and then decreasing magnetic fields to the sample, a ferromagnetic hysteresis loop can be obtained in the in-plane or out-of-plane direction. The saturation magnetization (M_s), remnant magnetization (M_r), and magnetic coercivity (H_c) of the ferromagnetic heterostructure can be attained by analyzing the M-H (Magnetization vs. Magnetic Field) hysteresis, which is analogous to the P-E hysteresis loop obtained for ferroelectric

materials. The measured M-H loop is a summation of the diamagnetic response of the straw and the magnetic response of the ferromagnetic material. Therefore, the diamagnetic response must be subtracted from the measured data to attain the M-H loop only of the ferromagnetic material, as shown in Figure 2-14.

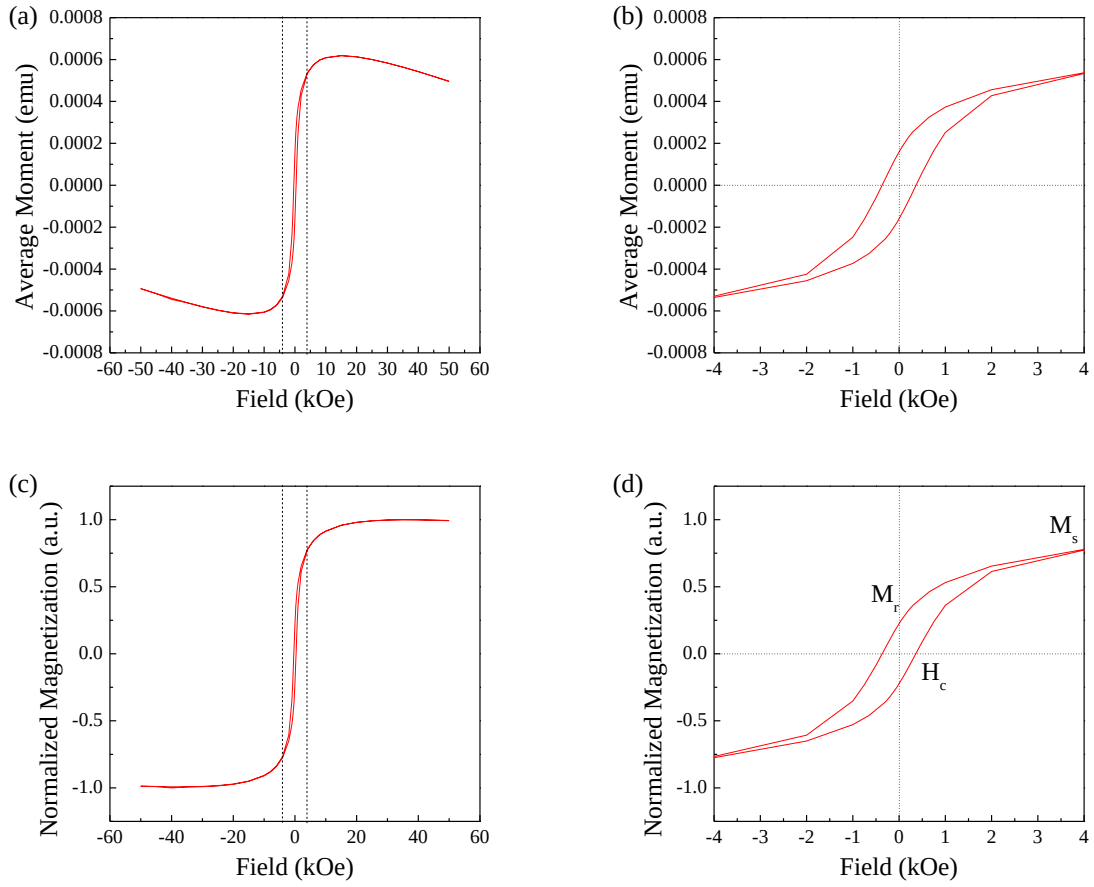

Figure 2-14. M-H hysteresis loop of a 100 nm thick sol-gel mesoporous CFO PEP 500 film on Si substrate measured via SQUID in the in-plane direction: (a) measured M-H loop, (b) zoomed-in view of (a) from -4 to 4 kOe, (c) analyzed M-H loop with the diamagnetic response of the straw subtracted, and (d) zoomed-in view of (c) from -4 to 4 kOe.

2.5.5 PFM and AFM

Analysis on the uniformity of deposited PZT layer require the use of atomic force microscopy (AFM) imaging. The AFM (Bruker Dimension FastScan Scanning Probe

Microscope) consists of a cantilever with a sharp-tip probe, specifications listed in Table 2-6, at its end that is used to scan the sample surface in the tapping mode. As the tip scans across the surface of sample area ranging up to 30 × 30 μm^2, deflection of the cantilever occurs as a result of the forces between the tip and sample to produce an image of the sample surface topography with atomic scale preciseness.

Table 2-6. List of tip and cantilever specifications of AFM tip (Bruker model FASTSCAN-A) used in this work

Tip Specification	
Material	Silicon
Geometry	Rotated (Symmetric)
Height	2.5-8 μm
Nominal Radius	5 nm
Maximum Radius	12 nm

Cantilever Specification	
Material	Silicon Nitride
Geometry	Triangular
Thickness	0.58 μm
Length	27 μm
Width	32 μm
k (spring constant)	18 N/m
f_o (resonant frequency)	1400 kHz
Front Side Coating	None
Back Side Coating	Reflective Aluminum

After obtaining the AFM image, Nanoscope Analysis program is used to analyze and determine the root-mean-square (RMS or R_q) average of height deviation (i.e. surface roughness):

$$RMS = R_q = \sqrt{\frac{\sum (Z_i)^2}{N}} \tag{2-8}$$

where Z_i is the current ith height value out of N total number of points within the box cursors. Before calculating the RMS, the data must first be flattened to correct for tilt in the plane of the

data. Figure 2-15 shows an AFM 3-dimensional image of an 18.3 nm thick ALD PZT thin film on Pt substrate that has been rapid thermal annealed with an RMS roughness of 1.9 nm.

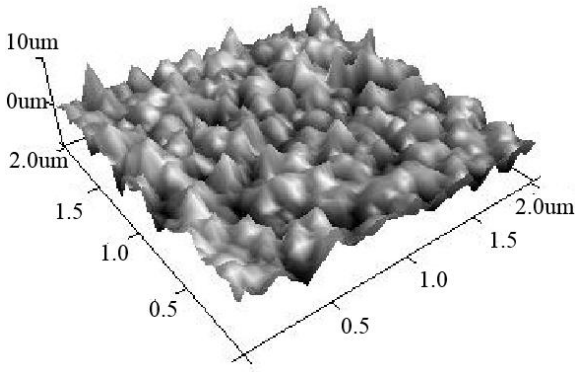

Figure 2-15. A 2 × 2 μm^2 scan size AFM image of an 18.3 nm thick PZT film on Pt substrate with a RMS roughness of 1.9 nm.

Piezoresponse force microscopy (PFM) is a scanning probe microscopy technique that can be used for probing electromechanics on the nanometer scale (Kalinin, Setter et al. 2009). An electrical bias is applied to the tip and when the tip is in contact with the piezoelectric surface, the electromechanical response is captured by measuring the tip's deflection from the surface's deformation. The specifications of the coated PFM tip are listed in Table 2-7.

Table 2-7. List of tip and cantilever specifications of coated PFM tip (Bruker model OSCM-PT-R3) used in this work.

Tip Specification	
Material	Silicon
Geometry	Visible Apex
Height	9-19 μm
Nominal Radius	15 nm
Maximum Radius	25 nm

Cantilever Specification	
Material	0.01-0.02 ohm-cm Silicon
Geometry	Rectangular
Thickness	2.3 μm
Length	240 μm
Width	40 μm
k (spring constant)	2 N/m
f_o (resonant frequency)	70 kHz
Front Side Coating	Ti/Pt, 20 nm
Back Side Coating	Al, 100 nm

The detected phase (first harmonic component of the bias-induced tip deflection) of the electromechanical response represents the polarization direction of the sample below the tip's position. The local surface expands or contracts if the polarization is parallel or anti-parallel with the applied electric field, respectively, resulting in a piezoresponse (PR) phase change plot and a PFM image (Proksch and Kalinin). The Bruker Dimension Icon Scanning Probe Microscope was used to obtain a PR phase change plot and a PFM image to show the piezoelectric property of crystallized PZT thin film. Figure 2-16 shows a 14 nm thick ALD PZT film deposited on Al_2O_3/4H-SiC substrate. To examine the retention properties of PZT, voltage was applied to change the polarity of the PZT film. The film was polarized at 12 V over an area of 10 × 10 μm^2, and then polarized at -12 V over a reduced area of 5 × 5 μm^2. The retention image was then obtained by scanning the surface at a tip bias of 3 V over an area of 12 × 12 μm^2. The contrast corresponds to the phase change and shows that the PZT domains were switched down and up by applying -12 V and 12 V, respectively (Zhang, Perng et al. 2011).

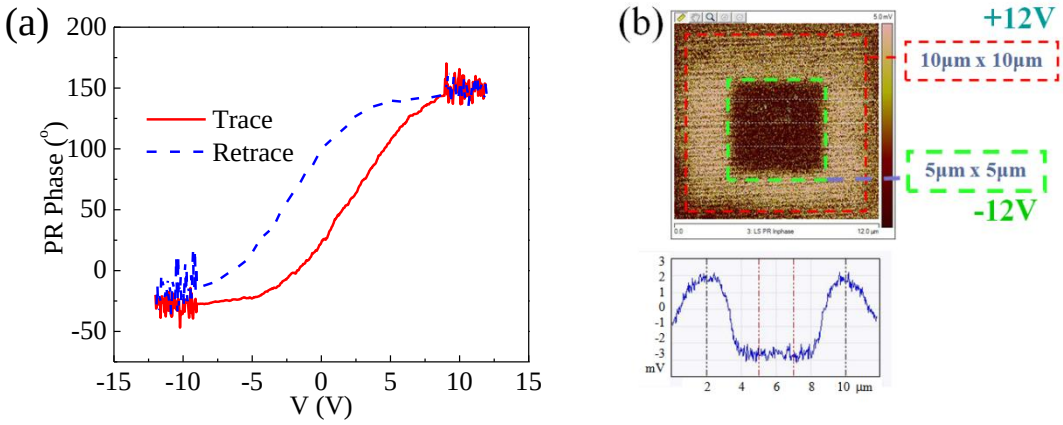

Figure 2-16. (a) Piezoresponse (PR) phase changes with the tip bias range of ±12 V captured at a sample bias of -4 V, (b) PFM image while the PZT thin film polarized at ±12 V with amplitude of the PR oscillations of ±2 mV (Zhang, Perng et al. 2011).

2.5.6 Wafer Flexure Method

The ALD PZT thin films deposited on platinized silicon substrate is mounted on a 3-inch Si carrier wafer using Loctite SuperGlue. A commercial strain gauge (~1.5 mm x 4.5 mm) is then mounted directly on top of the sample (Wilke, Moses et al. 2012). The strain gauge consists of a metallic foil pattern and when the foil is deformed, the electrical resistance changes in proportion to the induced strain. The Si carrier wafer is then clamped in a uniform pressure rig, as shown in Figure 2-17.

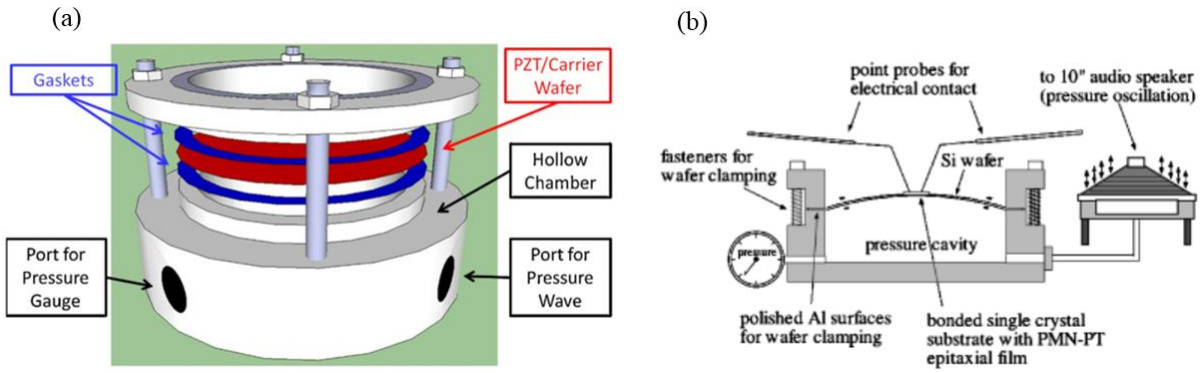

Figure 2-17. Wafer flexure method experimental setup: (a) 3D rendering of mounting of PZT/carrier wafer for measurement (Wilke, Moses et al. 2012) and (b) modification to measure small size samples of $\leq$ 1 cm^2 (Maria, Shepard et al. 2005).

2.5.7 MOKE

Another method that has recently become widely used to study magnetic thin films is magneto-optic Kerr effect (MOKE) magnetometer due to its simplicity (Qiu and Bader 2000; Oakberg 2010). The magnetic properties of a magnetic film can be measured in the in-plane and out-of-plane direction with respect to the substrate by applying the magnetic field parallel and perpendicular, respectively, to the sample surface. The in-plane MOKE measurement set-up that was used in this work is shown in Figure 2-18.

(a) (b)

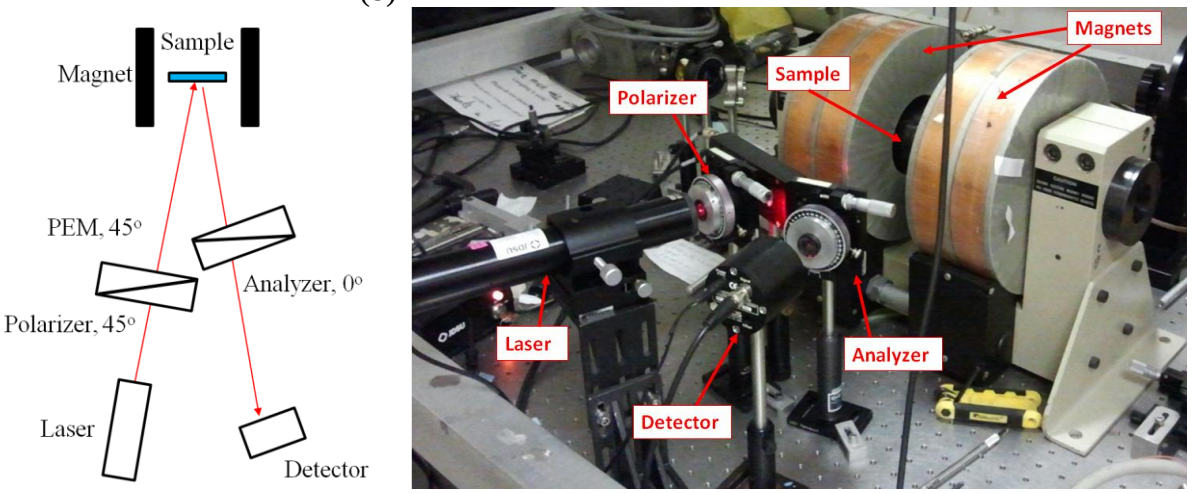

Figure 2-18. (a) Schematic and (b) picture of actual in-plane MOKE measurement set-up that was used in this work.

In this work, a polar MOKE geometry (HINDS Instruments) was used in building E-V room 18-132. A laser beam first passes through a polarizer and a photoelastic modulator (PEM), which are both set at 45°, and then impinges on the sample. The PEM is set to 630 nm and 50.073 kHz. The polarized light is reflected from the sample through an analyzer that is set at 0° to a detector which measures the rotation of the plane of polarization. The rotation is directly related to the magnetization of the material. The magneto-optic effect occurs due to the coupling between the electrical field of the light and the electron spin in the magnetic material. It has been observed that this effect is weak in nonmagnetic materials due to equal number of spin-up and spin-down electrons and strong in ferromagnetic materials due to the unbalanced population of electron spins (Qiu and Bader 2000). A hysteresis loop obtained via MOKE averaged over 5 scans in the in-plane direction of a heterostructure (from top to bottom): Ta (1.5 nm)/MgO (2 nm)/$Co_{20}Fe_{60}B_{20}$ (1.1 nm)/Ta (5 nm) annealed at 250°C for 30 minutes is shown in Figure 2-19. The sample shows a $\pm H_c$ of $\pm$390 Oe in the in-plane direction and magnetic anisotropy in the out-of-plane direction.

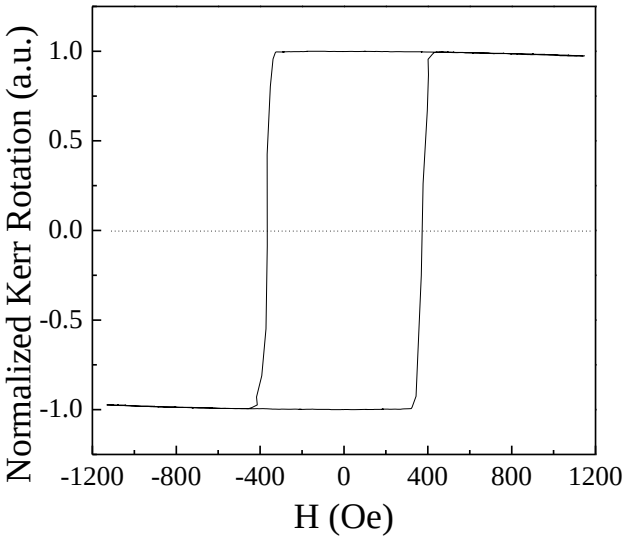

Figure 2-19. MOKE of sputtered Ta (1.5 nm)/MgO (2 nm)/$Co_{20}Fe_{60}B_{20}$ (1.1 nm)/Ta (5 nm) heterostructure that was annealed at 250^{o}C for 30 minutes measured in the in-plane direction, showing a $\pm H_c$ of $\pm$390 Oe.

2.5.8 Ex-Situ Poling Set-Up

In order to study the magnetoelectric coupling effect in multiferroic nanocomposites, the samples need to be electrically poled up to ±200 V. First, a 300 nm thick titanium layer was deposited by a CVC 601 sputtering system onto the backside of the conductive silicon substrate as the metal back electrode for the poling set-up. The ex-situ poling set-up consisted of placing the multiferroic nanocomposite of 5 × 5 mm^2 in size and a 12.7-μm-thick polymer spacer (polyvinylidene chloride) between two aluminum electrodes of 1.28 cm in diameter, as shown in Figure 2-20.

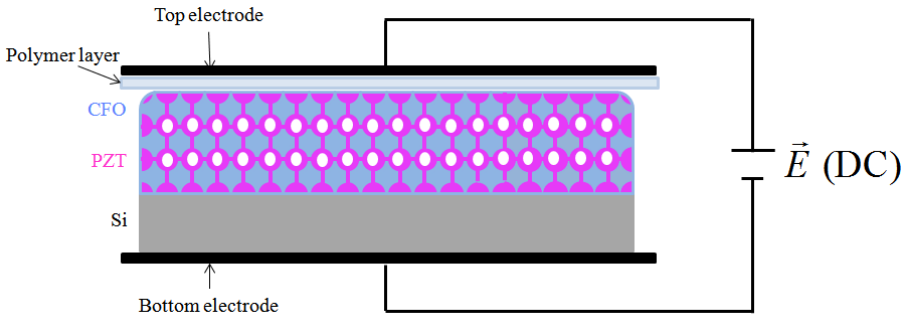

Figure 2-20. Ex-situ poling set-up with PZT/CFO multiferroic nanocomposite.

The nanocomposite was electrically poled in the out-of-plane direction for 10 minutes, then placed into a Quantum Design MPMS superconducting quantum interference device (SQUID) magnetometer to be magnetically measured at ±15 kOe (1.5 Tesla). The effect of electrically poling on the magnetic moment of a PZT/CFO multiferroic nanocomposite with total thickness of 100 nm measured in SQUID is shown in Figure 2-21.

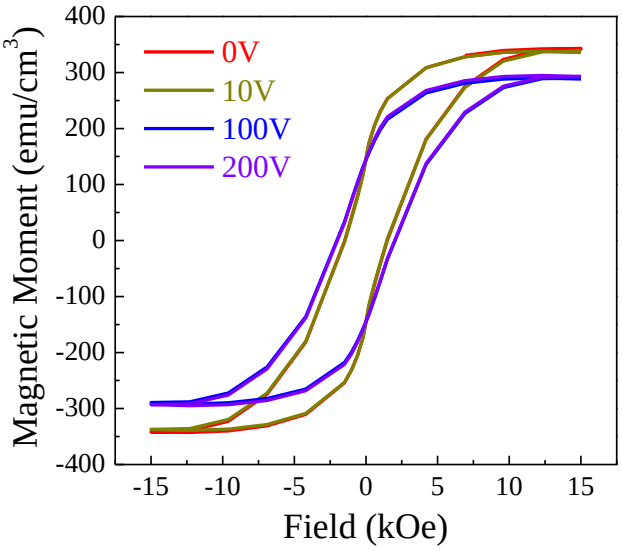

Figure 2-21. Porous CFO filled with 3 nm ALD PZT and annealed at 700°C. CFO pores had neck size of 12 nm diameter and pore size of 15 nm diameter. The samples were ex-situ poled with 0-200V and the magnetic moment was measured in SQUID with out-of-plane magnetic field.

A change in magnetization of the ferromagnetic layer was expected due to the strain transfer when the electric field was applied through the ferroelectric layer.

2.5.9 VCMA and TMR Measurement Set-Up

In order to measure the VCMA coefficient and TMR ratio, the magnetic tunnel junctions were fabricated to ellipses with diameters of 4 μm × 16 μm and 4 μm × 12 μm. The measurements were then performed via a 3-probe measurement under vacuum to measure the resistance-magnetic field (R-H) plot while applying different voltages, as shown in Figure 2-22.

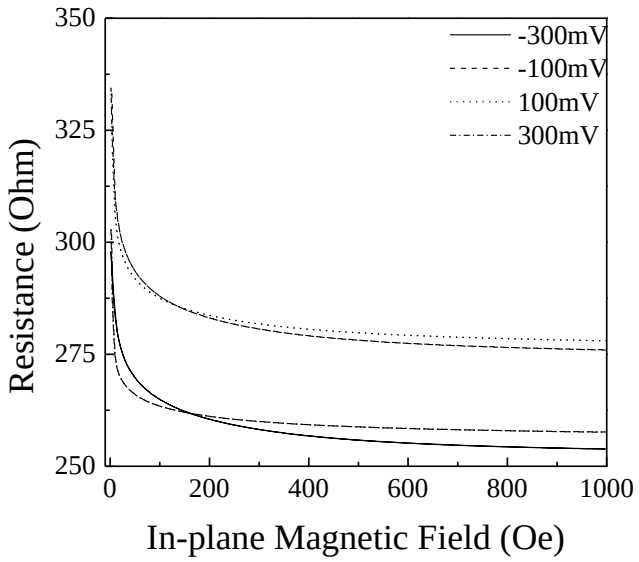

Figure 2-22. Resistance vs. in-plane magnetic field of varying applied voltages from -300 to +300 mV for an MgO MTJ device with structure from top to bottom of Pt (2 nm)/Ta (4 nm)/$Co_{20}Fe_{60}B_{20}$ (2.0 nm)/MgO (2.5 nm)/$Co_{20}Fe_{60}B_{20}$ (0.9 nm)/Ta (18 nm).

The tunneling magnetoresistance (TMR) ratio can be calculated from the R-H plot by using the Julliane model where the TMR ratio is defined by:

$$TMR = \frac{R_{ap} - R_p}{R_p} \tag{2-9}$$

The R_{ap} is the anti-parallel resistance and the R_p is the parallel resistance, and the R_{ap} is calculated according to the Slonczewski's equation by:

$$\frac{1}{R_{ap}} = \frac{2}{R_{ort}} - \frac{1}{R_p} \tag{2-10}$$

where the parallel resistance R_p is the resistance at maximum magnetic field or $1/G(H_{max})$, and the orthogonal CoFeB configuration resistance R_{ort} is the resistance at zero external magnetic field.

In order to find the VCMA coefficient, we first use an equation proposed by Slonczewski $G = G_S(1 + P_F^2 \cos\theta)$, the conductance G of the MTJ can be related to the relative angle between the two CoFeB layers, θ, where G_S is the mean surface conductance, P_F is the effective spin polarization (Slonczewski 1989), and the M_x/M_s can be calculated by:

$$\frac{M_x}{M_S} = \frac{G(H) - G(0)}{G(H_{\max}) - G(0)} \tag{2-11}$$

where M_x is the in-plane component of the magnetization, M_s is the saturation magnetization, *G(H)* is the conductance of the MTJ device at an in-plane magnetic field *H*, *G(0)* is the conductance at zero Oe in-plane magnetic field, and $G(H_{max})$ is the conductance at the maximum in-plane magnetic field measured. The M_x/M_s can then plotted from the resistance vs. in-plane magnetic field plot, as shown in Figure 2-23.

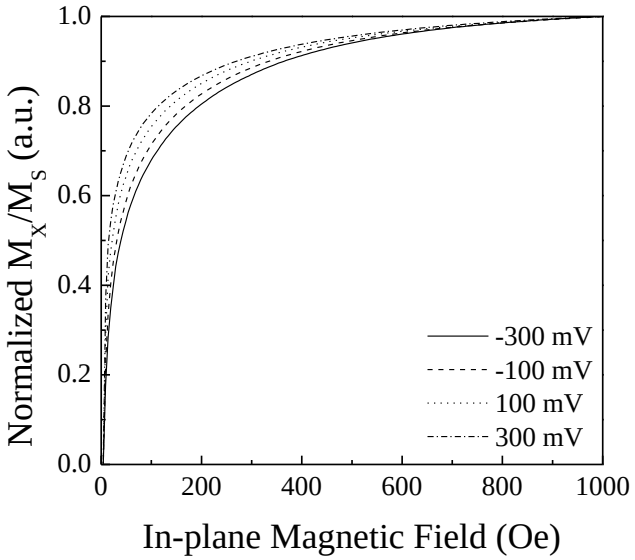

Figure 2-23. From the resistance vs. in-plane magnetic field plot, the normalized M_x/M_s can be calculated by using the Slonczewski equation.

Next, the perpendicular anisotropy energy, E_{perp}, and the interface magnetic anisotropy, K_i, can be obtained using the following equations (Ikeda, Miura et al. 2010; Shiota, Bonell et al. 2013):

$$E_{perp} = M_S \int_0^1 H \cdot d\left(\frac{M_x}{M_S}\right) \tag{2-12}$$

$$K_i = \left(2\pi {M_S}^2 + E_{perp}\right) t_{CoFeB} \tag{2-13}$$

where H is the in-plane magnetic field and t_{CoFeB} is the thickness of CoFeB free layer. Then, the VCMA coefficient, ξ, in units of fJ/V-m is found from the slope of the K_i vs. electric field plot, as shown in Figure 2-24.

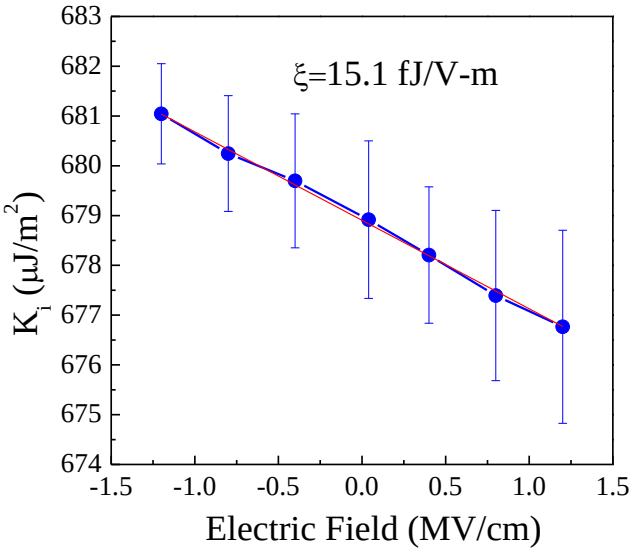

Figure 2-24. From the normalized M_x/M_s plot, the K_i can be calculated for each applied voltage. The VCMA coefficient, ξ, is the slope in this figure and is in units of fJ/V-m. For the reference MgO MTJ device used in this work, the ξ was measured to be 15.1 fJ/V-m.

CHAPTER 3. ATOMIC LAYER DEPOSTION OF PZT THIN FILMS

Studies were conducted on the growth and characterization of ALD lead titanate zirconate (PZT) thin films. PZT thins films were grown and characterized on silicon and platinized silicon substrates using atomic layer deposition. A (100) textured ALD $PbTiO_3$ seed layer was used as a template to attain the (100) oriented PZT on platinized silicon substrates. Scalability of PZT films were realized over large 6-inch area wafers and by chemical vapor deposition (CVD). Furthermore, ALD PZT films were deposited to coat La_2NiMnO_6 and La_2CoMnO_6 nanoparticles to synthesize multiferroic core-shell nanoparticles.

3.1 PZT on Silicon Substrates

As-deposited ALD PZT thin films are amorphous, so a subsequent annealing step is needed to crystallize the PZT films. In addition to rapid thermal annealing, microwave annealing of the ALD PZT thin films on platinized silicon substrate was also tested using the Milestone SynthWAVE Microwave Reactor. ALD PZT film with thickness of 15 nm was deposited on platinized silicon substrate and microwave annealed at 200°C at microwave power of 1200 W for 30 minutes in a deionized water solvent. The XPS survey scan of the film is shown in Figure 3-1.

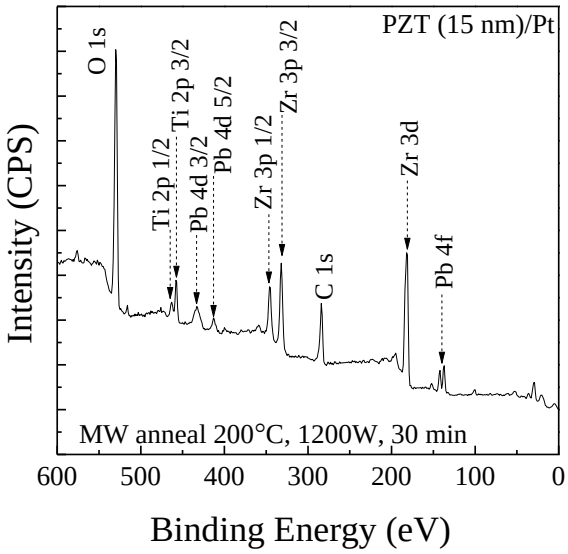

Figure 3-1. XPS survey scan of 15 nm thick ALD PZT thin film on Pt substrate that was microwave annealed at 200°C at 1200 W for 30 minutes.

The XRD of the microwave annealed PZT/Pt sample is compared to the platinized silicon substrate, as-deposited PZT/Pt sample, and RTA 700°C for 1 minute in O_2 environment PZT/Pt sample, as shown in Figure 3-2.

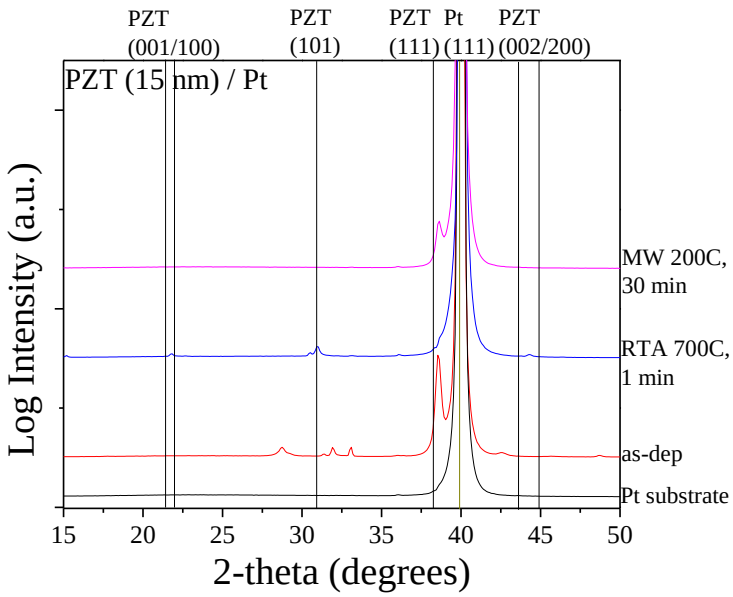

Figure 3-2. XRD scan comparing Pt substrate and 15 nm thick ALD PZT thin film on Pt substrate that was as-deposited, RTA at 700°C for 1 minute, and microwave annealed at 200°C at 1200 W for 30 minutes.

As can be seen in the XRD measurement by the lack of PZT crystalline peaks, the microwave annealing process did not crystallize the film. Therefore, in this work, the ALD PZT thin films were all crystallized via rapid thermal annealing at 700°C for 1 minute in oxygen environment.

In order to observe the piezoelectric properties of ALD PZT films, the P-E hysteresis loop at $\pm$5, $\pm$10, $\pm$15, and $\pm$20 V was obtained with a RT-66A, as shown in Figure 3-3, for a 20 nm thick ALD PZT film grown on platinized silicon substrate that was fabricated into a metal-ferroelectric-metal (MFM) device structure to measure the electrical properties of the thin film. The challenge of this measurement was the ultra-thin thickness of the PZT film due to the leakage problem. Therefore, 10 nm thick ALD Al_2O_3 was deposited between the Pt top electrode and ALD PZT film as a barrier layer.

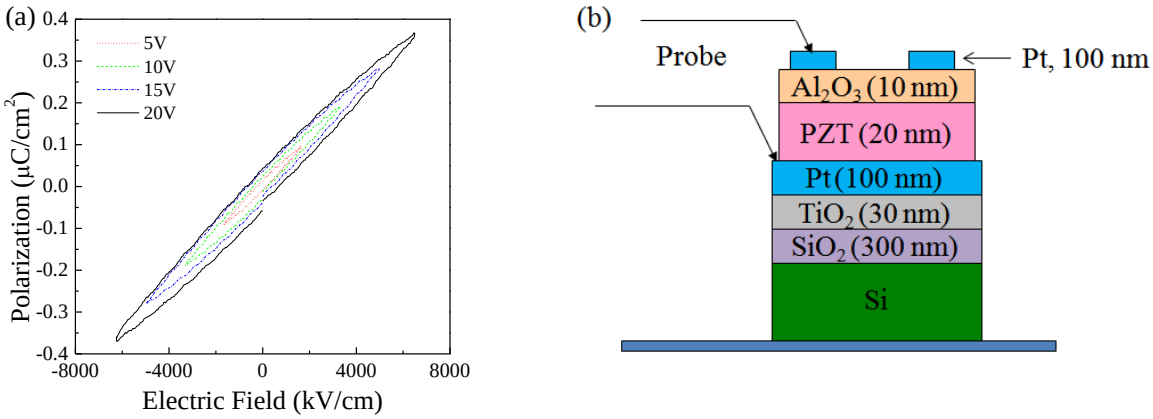

Figure 3-3. (a) P-E hysteresis loop of 20 nm thick ALD PZT thin film poled at ±5, ±10, ±15, and ±20 V and (b) schematic of the MFM device structure of Pt / ALD Al_2O_3 (10 nm) / ALD PZT (20 nm) / Pt substrate.

In order to quantify the dielectric constant of PZT thin films, PZT metal-oxide-semiconductor capacitor (MOSCAP) devices were made and characterized by capacitance-voltage (C-V) measurements. The dielectric constant (*K*) of the PZT film was calculated by measuring the capacitance of the film and using the following expression:

$$K = \frac{Cd}{A\varepsilon_o} \tag{3-1}$$

where *C* is the capacitance (units of *F*), *d* is the thickness of the dielectric layer (units of *m*), *A* is the area of the capacitor (units of m^2), and ε_o is the permittivity of free space and equal to 8.854 × 10^{-12} F/m.

An ALD PZT film with thickness of 20 nm and a CVD PZT film with thickness of 57 nm were separately deposited on a Si (100) substrate. For both samples, the top electrodes were 800 μm in diameter and Ti (10 nm)/Au (50 nm) were deposited through a shadow mask using the CHA Mark 40 e-beam evaporator. The bottom electrodes were made by scratching the backside with a diamond scribe to remove the native silicon dioxide layer, and then depositing 300 nm thick Ti layer using the CVC 601 Sputtering System. After fabrication, the ALD and CVD PZT

MOSCAP devices were measured at the probe station, which was connected to a Hewlett Packard 4284A Precision LCR Meter operating in the C_p-D mode, using soft contact probe tips (Micromanipulator, model 7B-5G) that are gold plated with point radius of 5-micron. A voltage was applied through the top and bottom electrodes with the PZT film between the electrodes in order to obtain the C-V curve. The C-V measurements were taken with sweeping voltage bias from -10 V to 10 V at a high frequency of 1 MHz with voltage step of 0.4 V, as shown in Figure 3-4.

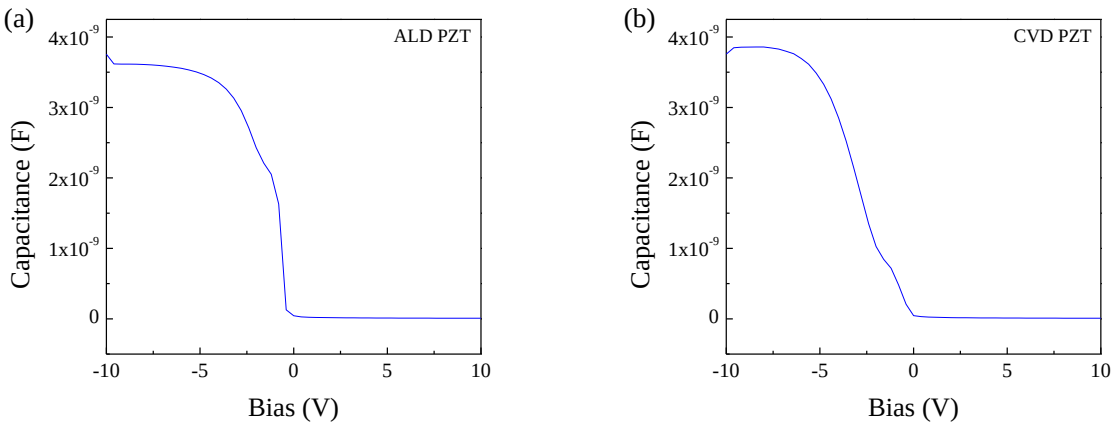

Figure 3-4. C-V curve of (a) ALD PZT film with thickness of 20 nm and (b) CVD PZT film with thickness of 57 nm deposited on Si substrate.

The dielectric constant of 20 nm thick ALD PZT film was found to be 17 and the dielectric constant of 57 nm thick CVD PZT film was found to be 48, which are plausible values taking account existing works on ultra-thin PZT films (Bastani, Schmitz-Kempen et al. 2011; Zhang, Perng et al. 2011). The dielectric constant dependence on thickness of PZT thin films was studied by Bastani *et al.* for films with thicknesses ranging from 20–260 nm, and they found that processing conditions, such as Pb content in the films, and the interfacial dead layer between film-electrode interface decreased the dielectric constant. They also observed a sharper linear

drop of dielectric constant with thickness for PZT films with thicknesses below 120 nm (Bastani, Schmitz-Kempen et al. 2011).

In order to demonstrate the feasibility of obtaining conformal PZT thin film on three-dimensional structures via ALD, a 15 nm thick ALD PZT thin film was deposited over 300 nm hollow Si_3N_4 cylinders with an aspect ratio up to 2.2:1. Table 3-1 shows SEM images of top-down view and cross-sectional view of the hollow Si_3N_4 cylinders before and after ALD PZT deposition.

Table 3-1. Top-down and cross-sectional SEM images of 15 nm thick ALD PZT thin film deposited over hollow 0.3 μm × 0.5 μm Si_3N_4 cylinders with AR of 2.2.

	Before ALD PZT Coating	After ALD PZT Coating
Top-Down View	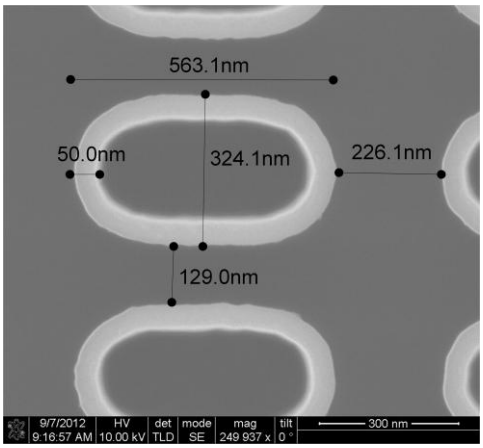	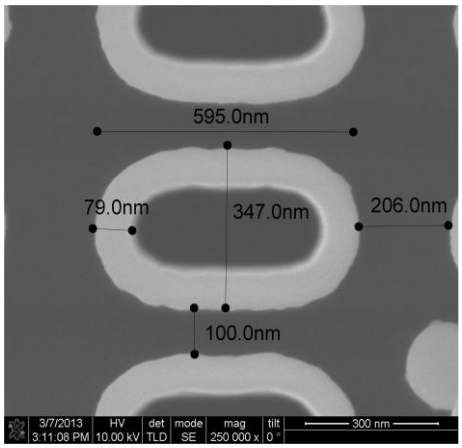
Cross-Sectional View	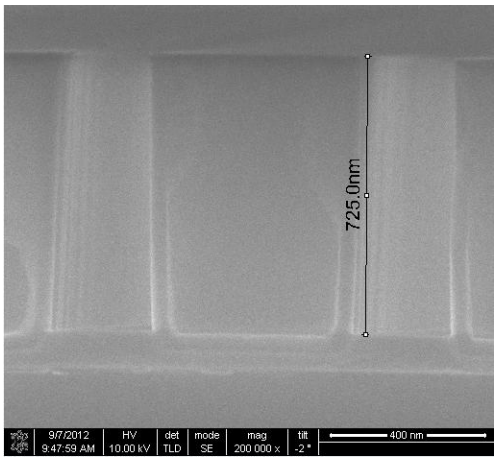 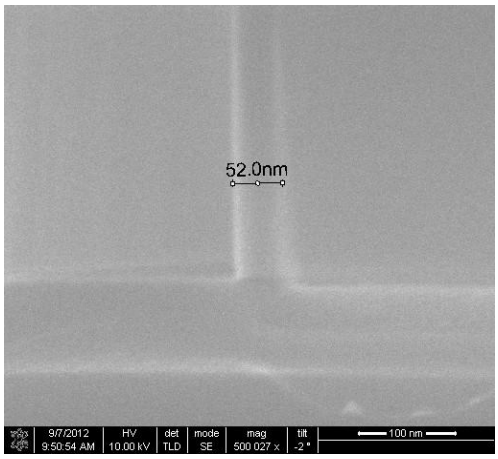	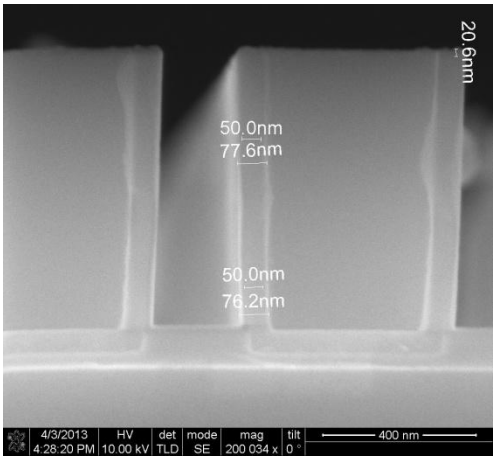 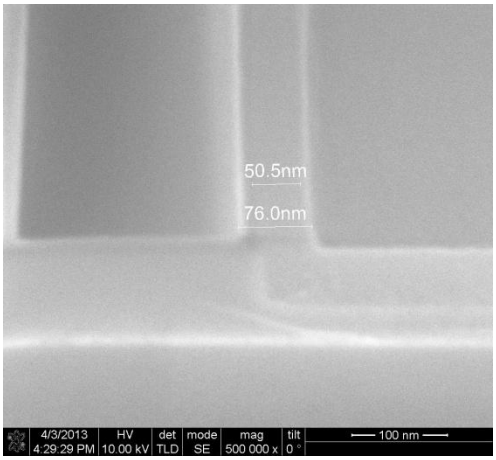

For higher aspect ratio structures, silicon trenches with width of 0.72 µm and depth of 6.12 µm having a high aspect ratio of 8.5:1 were used. SEM of silicon trench is shown in Figure 3-5.

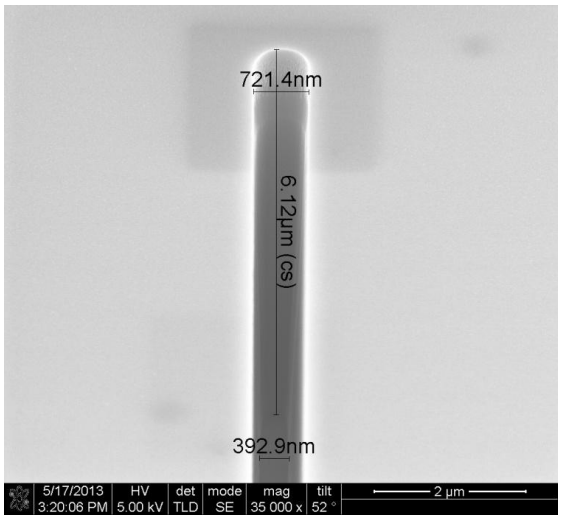

Figure 3-5. SEM of silicon trench with width of 0.72 µm and depth of 6.12 µm with high aspect ratio of 8.5.

A 20.9 nm thick PZT thin film was deposited on the silicon trenches. The top-view and cross-sectional SEM and EDX views of the coated 0.6 micron wide trenches are shown in Figure 3-6 and Figure 3-7, respectively.

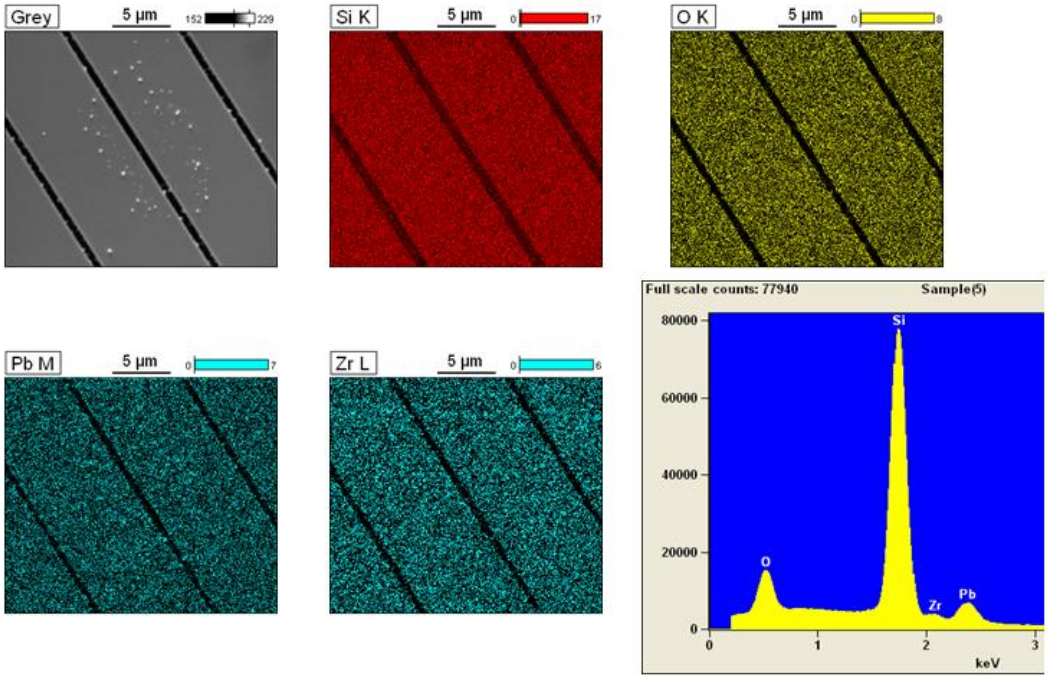

Figure 3-6. Top-view SEM and EDX images of 20.9 nm thick PZT film on Si trenches with high aspect ratio of 8.5.

The EDX showed Pb and Zr elemental peaks on the surface. The Ti peak was difficult to detect because it can only be seen at higher energy levels. The cross-sectional views showed that the intensity of Pb peak decreases from the top to bottom of the trench while the Zr and Ti peaks were not detected.

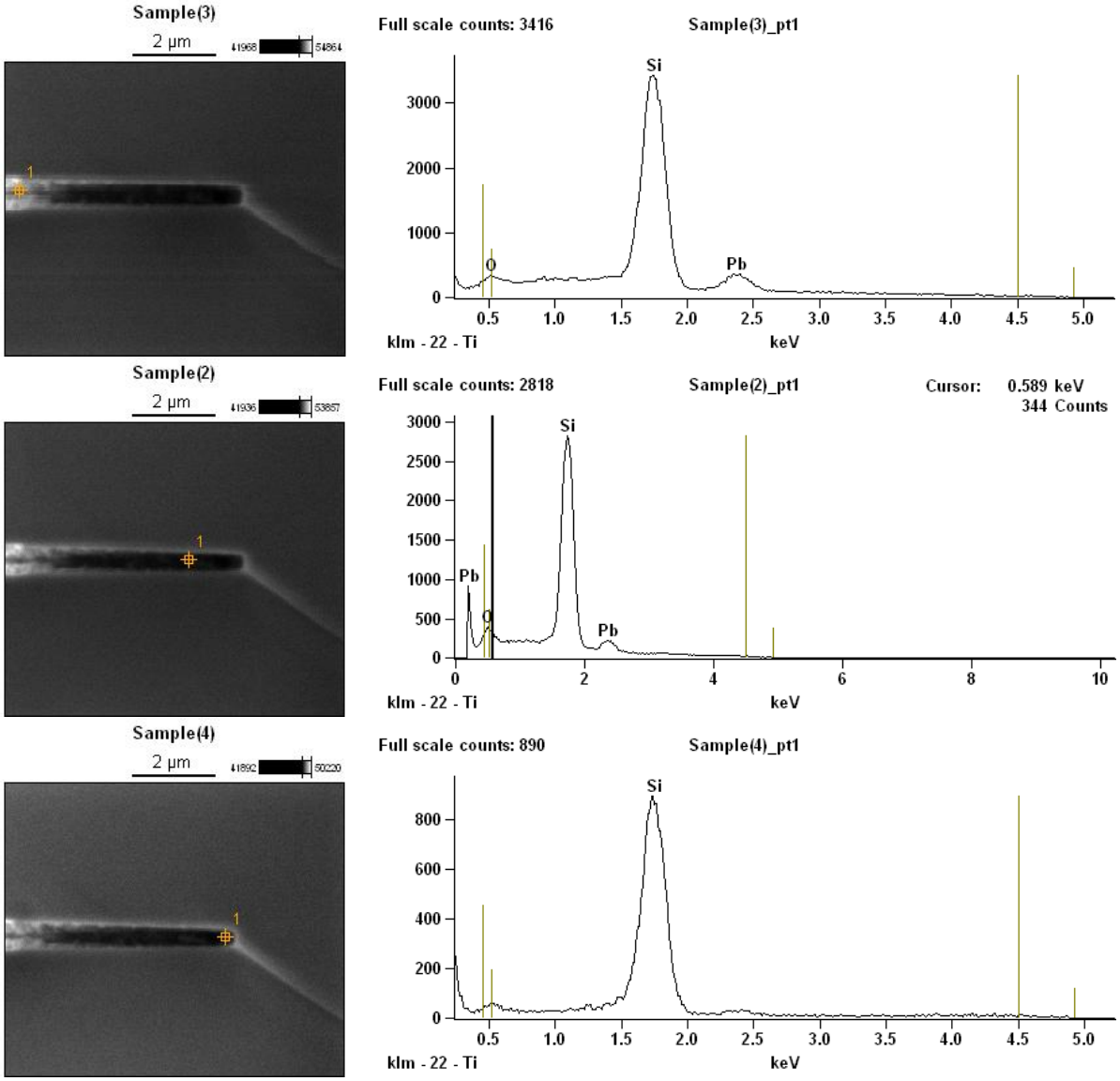

Figure 3-7. Cross-sectional view SEM and EDX images of 20.9 nm thick PZT film on Si trenches with high aspect ratio of 8.5.

3.2 ALD PZT with an ALD $PbTiO_3$ Seed Layer

PZT thin films were successfully grown on platinized silicon substrates using atomic layer deposition (ALD). The platinized silicon substrate, commercially manufactured from MEMS Exchange, consists of 100 nm thick Pt (111) thin film grown on a 35 nm thick TiO_2 layer on a thermally oxidized 300 nm thick SiO_2 film on a silicon wafer. ALD PZT thin film showed

the expected (111) orientation when grown on Pt (111) substrate, as confirmed by the Grazing Incidence Wide Angle X-ray Scattering (GIWAXS) diffraction data shown in Figure 3-8 and Figure 3-9 which was collected at the Stanford Synchrotron Radiation Laboratory (SSRL) using beamline (BL) 11-3.

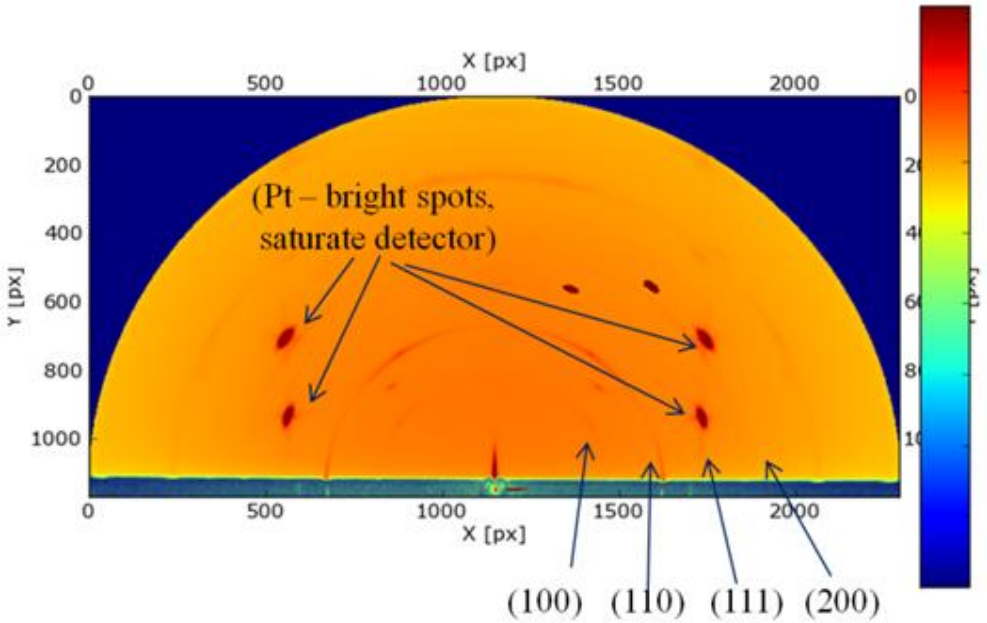

Figure 3-8. GIWAXS 2D diffraction data of 6.4 nm thick ALD PZT thin film on Pt (111) substrate.

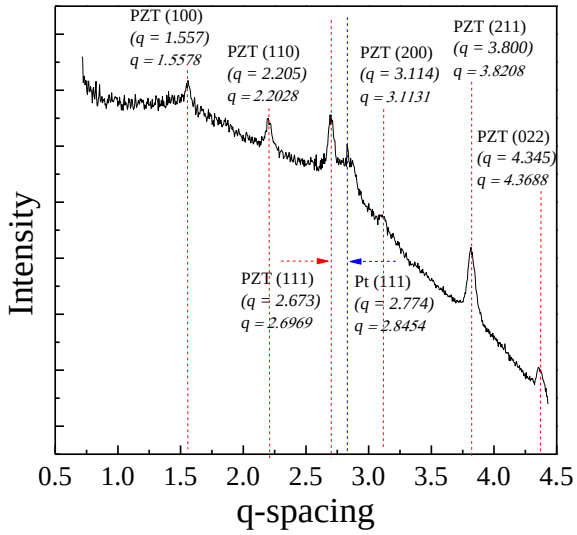

Figure 3-9. Out-of-plane diffraction at $\chi = 90^{o}$ measured at SSRL beamline 11-3 of 6.4 nm thick ALD PZT thin film on Pt (111) substrate.

The (001) oriented PZT was desired because it has a higher transverse piezoelectric coefficient, $e_{31,f}$, than (111) oriented PZT (Ledermann, Muralt et al. 2003). PZT orientation is generally governed by nucleation, so the challenge was to use a (001) textured ALD $PbTiO_3$ seed layer as a template to attain the desired (001) oriented PZT thin film.

The $PbTiO_3$ seed layer was chosen due to its good lattice matching with PZT film, as shown in Table 3-2, and its tendency to grow in the (001) orientation on platinized silicon substrate (Trolier-McKinstry 2008).

Table 3-2. Crystal structure and lattice spacing for platinum, $PbTiO_3$, and PZT with references [1](Arblaster 2006), [2](Nelmes and Kuhs 1985), and [3](Noheda, Gonzalo et al. 2000), respectively.

Material	[1]Pt	[2]$PbTiO_3$	[3]$Pb(Zr_{0.52}Ti_{0.48})O_3$
Crystal Structure	Face-centered Cubic	Tetragonal	Tetragonal
Lattice Spacing	3.92 Å	a = 3.90 Å c = 4.16 Å	a = 4.05 Å c = 4.14 Å

In order to seamlessly integrate the PZT thin film, the $PbTiO_3$ seed layer was also deposited via ALD. The processing (e.g. cycle ratios, precursor housing temperatures) and annealing (e.g. methodology, temperature, time, ramp rate, environment) conditions were studied to obtain stoichiometric and (001) oriented $PbTiO_3$ seed layer. The films were characterized for composition and crystallinity via X-ray photoelectron spectroscopy (XPS) and X-ray diffraction (XRD), respectively. Figure 3-10 shows lead titanate thin films were successfully deposited on Pt substrates via ALD.

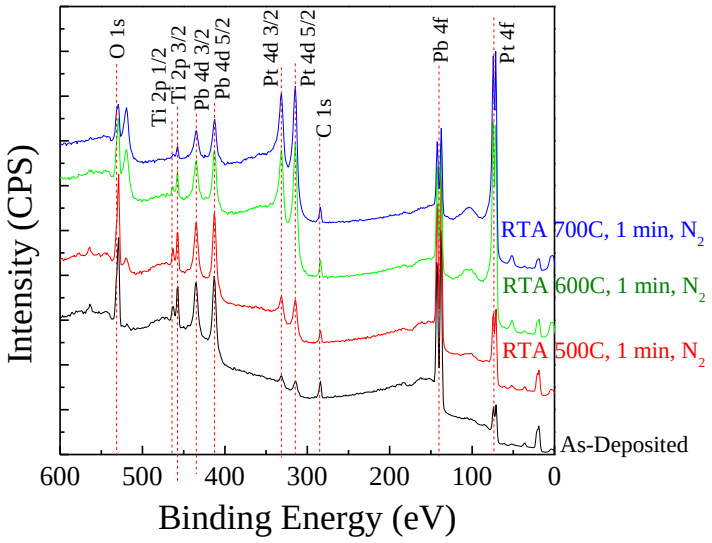

Figure 3-10. XPS for ALD $PbTiO_3$ thin film on Pt substrate, pre- and post-annealing.

Figure 3-12 shows the composition determined by XPS for as-deposited and annealed ALD $PbTiO_3$ thin film grown on platinized silicon substrate. The annealing effects of methodology, environment, temperature, and heating ramp rate were studied.

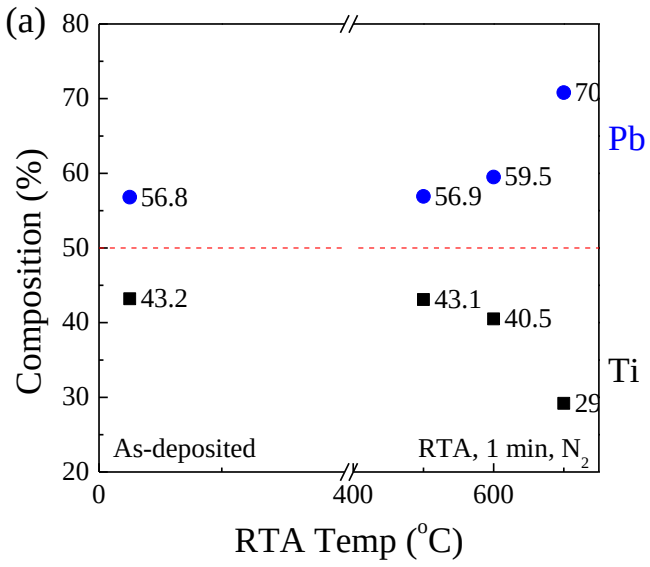

Figure 3-11. Pb and Ti composition of ALD $PbTiO_3$ thin film on Pt substrate when (a) annealed in N_2.

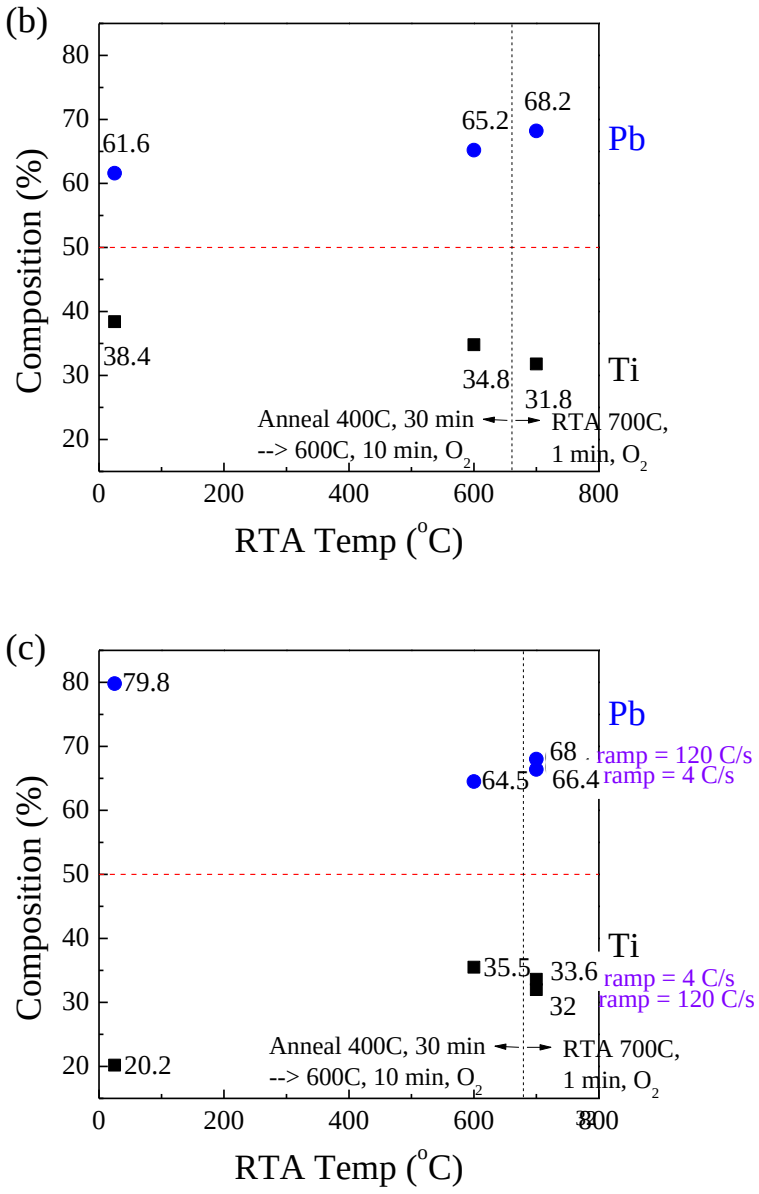

Figure 3-12 (Continued). Pb and Ti composition of ALD $PbTiO_3$ thin film on Pt substrate when (b) annealed in O_2 and (c) annealed in O_2 with different heating ramp rates.

The $PbTiO_3$ samples were annealed either by rapid thermal annealing (RTA) for 1 minute or by a 2-step (400°C for 30 minutes followed by 600°C for 10 minutes) furnace annealing process. There is a smaller Pb and Ti composition difference between the as-deposited and

annealed sample in an oxygen annealing environment compared to a nitrogen atmosphere. It was also observed that the composition after RTA and 2-step furnace annealing was relatively similar. For RTA, the difference in composition when sample was heated at a fast ramp rate of 120°C/sec compared to slow ramp rate of 4°C/sec was negligible. However, the slower ramp rate ensured that the annealing temperature did not greatly overshoot the set point, approximately by 5°C (compared to the fast ramp rate which surpassed the set point by 60°C). Therefore, RTA for 1 minute in oxygen ambient with heating ramp rate of 50°C/sec was chosen as the annealing process for ALD $PbTiO_3$ seed layer.

XRD was used to observe the crystallinity of the as-deposited and annealed $PbTiO_3$ thin films. The film was annealed in RTA at 700°C for 1 minute in oxygen environment. Figure 3-13 shows a XRD survey scan from 5°-80° and Figure 3-14 shows a XRD detailed scan from 5°-30° of an as-deposited and annealed ALD $PbTiO_3$ thin film with composition of Pb/Ti = 57/43 and a thickness of 10.1 nm, measured by XPS and ellipsometer, respectively.

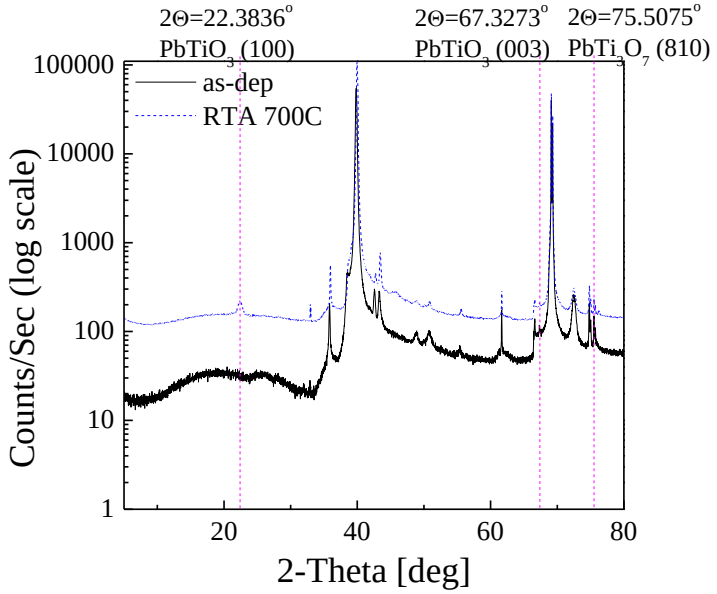

Figure 3-13. Survey XRD scan from 5°-80° of as-deposited and annealed 10.1 nm thick ALD $PbTiO_3$ thin film on platinized silicon substrate.

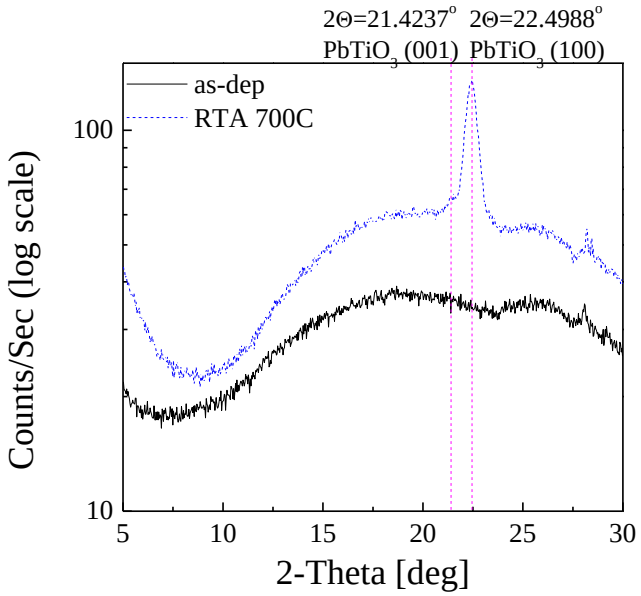

Figure 3-14. Detailed XRD scan from 5^{o}-30^{o} of as-deposited and annealed 10.1 nm thick ALD PbTiO3 thin film on platinized silicon substrate.

The survey scan confirmed that the annealing process successfully crystallized the $PbTiO_3$ thin film. The detailed scan showed that in addition to the sharp $PbTiO_3$ (100) peak, there exists a small feature for the $PbTiO_3$ (001) peak. Therefore, the XRD data showed that (001)/(100) oriented ALD $PbTiO_3$ thin film, dominantly (100) oriented, can be grown on Pt (111) substrate. This was also confirmed by the GIWAXS diffraction data taken at SSRL BL 11-3, as shown in Figure 3-15 and Figure 3-16.

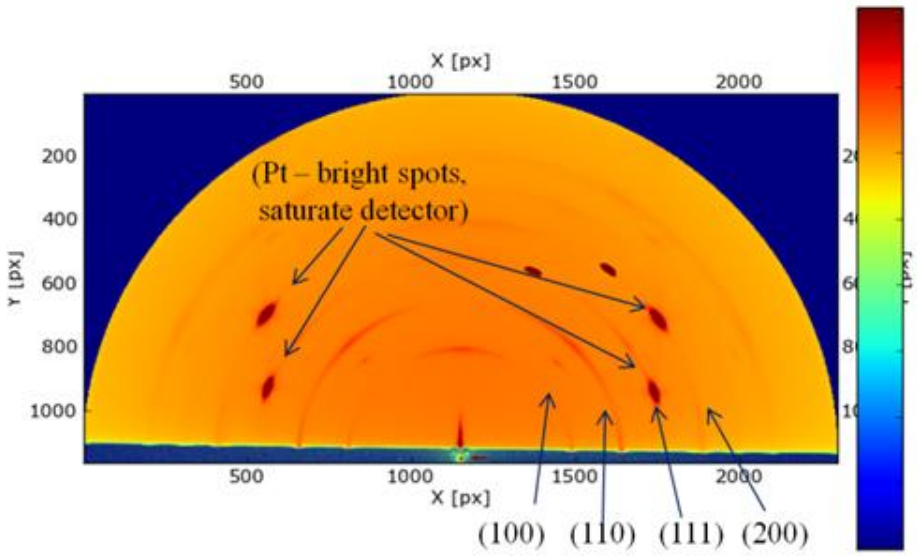

Figure 3-15. GIWAXS 2D diffraction data of 12.2 nm thick ALD $PbTiO_3$ thin film on Pt (111) substrate.

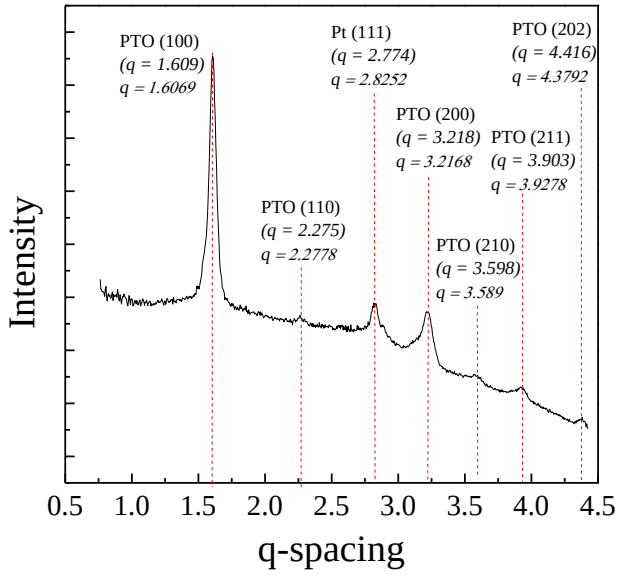

Figure 3-16. Out-of-plane diffraction at $\chi = 90^o$ measured at SSRL beamline 11-3 of 12.2 nm thick ALD $PbTiO_3$ thin film on Pt (111) substrate.

PZT growth is nucleation controlled, which indicates that the nucleation, thus including texture, is dependent on the substrate and the interface (Muralt, Maeder et al. 1998).

Previous research has shown that (001) textured PZT films was achieved with the help of a seed layer of (001) textured $PbTiO_3$ film via chemical solution deposition on $Pt/TiO_2/SiO_2/Si$ substrate (Sanchez, Potrepka et al. 2011). Previous research also has shown that a thickness of 10-20 nm of $PbTiO_3$ seed layer deposited by sputtering and sol-gel was successful in growing (001) oriented PZT films (Trolier-McKinstry 2008). Liquid injection ALD have been used to grow $PbTiO_x$ films on platinum-covered silicon substrates, but XRD data of 15 nm thick $PbTiO_x$ film showed it to be randomly oriented at (001)/(100) and (101)/(110) (Watanabe, Hoffmann-Eifert et al. 2007). Therefore, the ALD operating conditions, such as housing temperatures and number of cycles, and annealing parameters, such as temperature, time, environment, and ramp rates, was studied and optimized to achieve dominantly (001)/(100) oriented $PbTiO_3$ seed layer on platinized silicon wafer. The growth of (001)/(100) textured PZT thin films, in order to obtain superior piezoelectric properties for device applications, on the ALD $PbTiO_3$ seed layer was then studied.

After depositing and annealing the ALD $PbTiO_3$ seed layer on platinized silicon substrate, the PZT thin film was deposited via ALD at sample temperature of 250^{o}C. Figure 3-17 shows Pb, Zr, and Ti composition and Figure 3-18 shows crystallinity of PZT thin film deposited on annealed ALD $PbTiO_3$ seed layer measured by XPS and XRD, respectively. Three annealing conditions were examined (1) RTA 600^{o}C for 1 minute, (2) RTA 700^{o}C for 1 minute, and (3) two-step furnace annealing process of 400^{o}C for 30 minutes followed by 700^{o}C for 10 minutes in an O_2 environment.

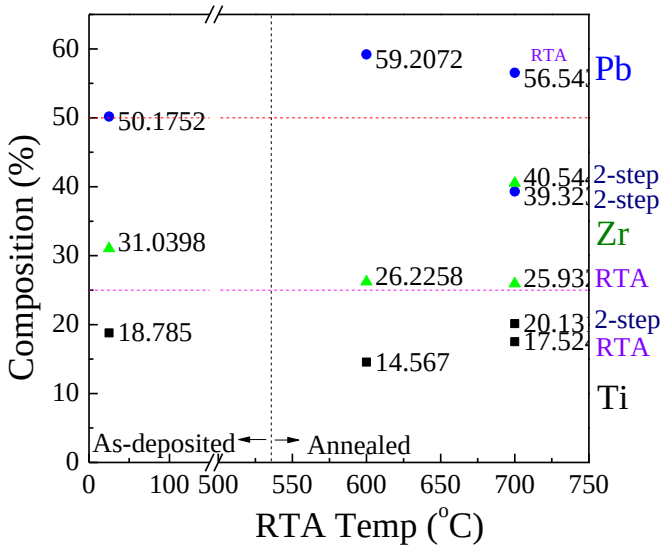

Figure 3-17. (a) Pb, Zr, and Ti composition of annealed 10.2 nm thick ALD PZT thin film on 8.7 nm thick $PbTiO_3$ seed layer on Pt (111) substrate. Three annealing conditions were used: RTA 600°C, RTA 700°C, and 2-step furnace annealing. The dotted lines indicated the desired composition for the metal elements.

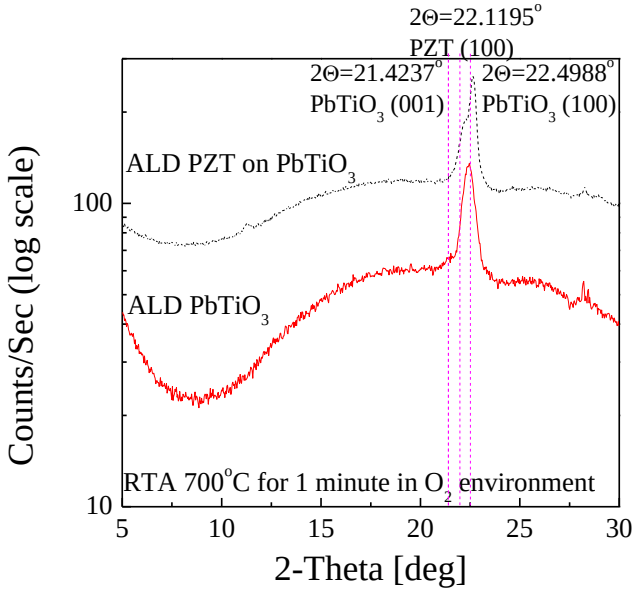

Figure 3-18. XRD of annealed 10.2 nm thick ALD PZT deposited on 8.7 nm thick $PbTiO_3$ seed layer compared to annealed 9.4 nm thick ALD $PbTiO_3$ thin film on Pt substrate.

Based on the composition analysis, near desired stoichiometry of Zr/Ti = 52/48 was obtained in ALD PZT thin film when annealed by RTA at 700°C for 1 minute in O_2 environment. XRD showed that the annealed ALD PZT thin film has a peak at PZT (100) orientation. Due to the $PbTiO_3$ seed layer to be dominantly (100) oriented, the annealed ALD PZT thin film exhibited the PZT (100) peak. Therefore, it appeared that the ALD $PbTiO_3$ seed layer is effective in obtaining textured PZT thin film. Figure 3-19 shows images taken from a scanning electron microscope (SEM) to confirm the uniformity of the annealed ALD PZT thin film deposited on ALD $PbTiO_3$ seed layer on platinized silicon substrate.

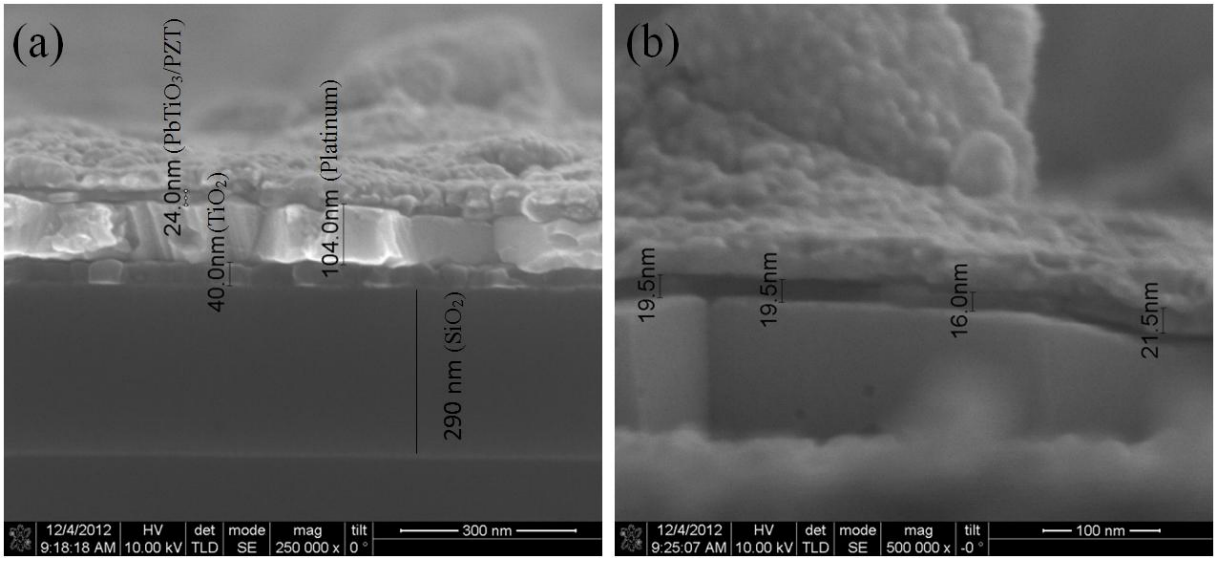

Figure 3-19. (a) Lower and (b) higher magnification of SEM images of annealed ALD PZT thin film on $PbTiO_3$ seed layer on platinized silicon substrate ($Pt/TiO_2/SiO_2/Si$). A 20 nm thick layer of gold was sputtered on the sample before imaging.

The piezoelectric property of an annealed ALD PZT (199.9 Å)/ALD $PbTiO_3$ (44.5 Å)/Pt sample was observed via piezoresponse force microscopy (PFM), as shown in Figure 3-20. The film was polarized at 12 V over an area of 5 × 5 μm^2 and, then, polarized at -12 V over a reduced area of 2 × 2 μm^2. An area of 7 × 7 μm^2 was scanned with a tip bias of 3 V to obtain a Phase

image. The color contrast indicated that the PZT domains were switched when poled at 12 V and -12 V.

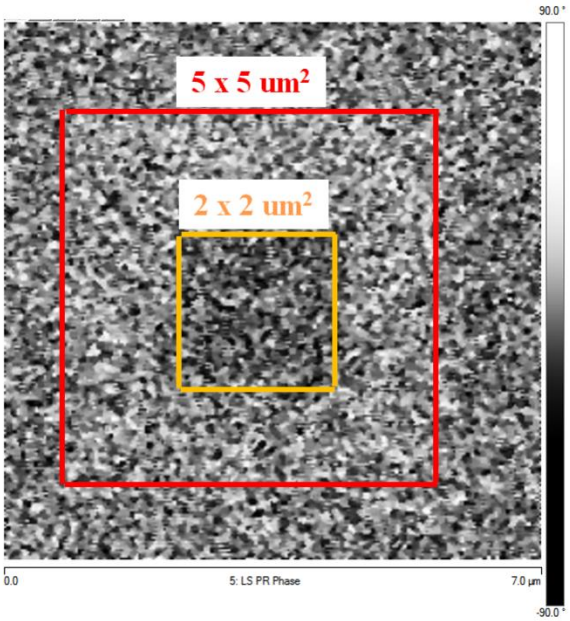

Figure 3-20. PFM image of ~20 nm thick ALD PZT thin film deposited on 4.5 nm ALD $PbTiO_3$ seed layer on platinized silicon substrate, polarized at 12 V over 5 × 5 μm^2, polarized at -12 V over 2 × 2 μm^2, and scanned with tip bias of 3 V over 7 × 7 μm^2.

3.3 Scalability of PZT Thin Films

In order to study the scalability of ALD to 4"-8" (100-200 mm) wafers, the modified PZT large scale reactor was used. Atomic layer deposition is strongly dependent on the substrate temperature so the sample heater temperature must be uniform from the wafer's center to the edge. Thermocouples were attached to the center and edge of the sample heater and the difference in temperature was determined to be 10^{o}C. In order to attain a more uniform temperature, a 0.020" thick molybdenum sheet was utilized and the temperature difference between the center and edge of the sample heater was reduced to 5^{o}C. Thickness uniformity across 6-inch wafer substrate improved with the temperature uniformity, which indicated that the film thickness is dependent on the substrate's temperature. Figure 3-21 shows the average

thickness from the center to the edge of half a 6-inch platinized silicon wafer as measured via ellipsometry.

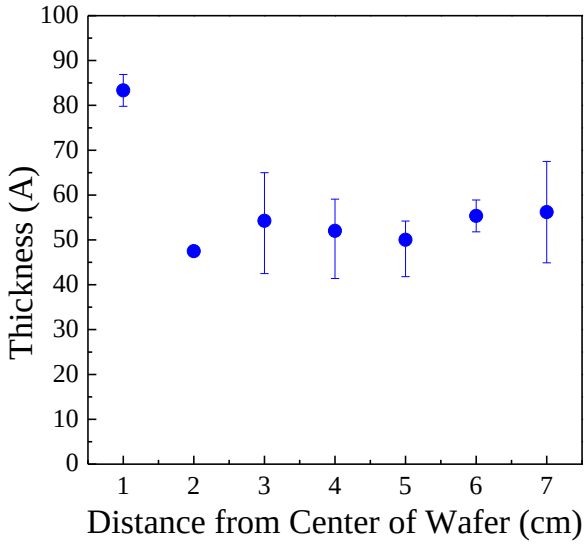

Figure 3-21. Ellipsometer measurement of PZT film thickness from center to edge on a 6-inch platinized silicon wafer substrate.

Between the radial distances from center of wafer of 2-7 cm, the average thickness was 52.8 Å with a difference of 13.1 Å. In the XPS survey scans, as shown in Figure 3-22, only Pb peaks were detected on the thin film deposited over a large platinized silicon substrate. However, XPS scans of samples in the small reactor which were deposited simultaneously confirmed Pb, Zr, and Ti peaks.

(a) (b)

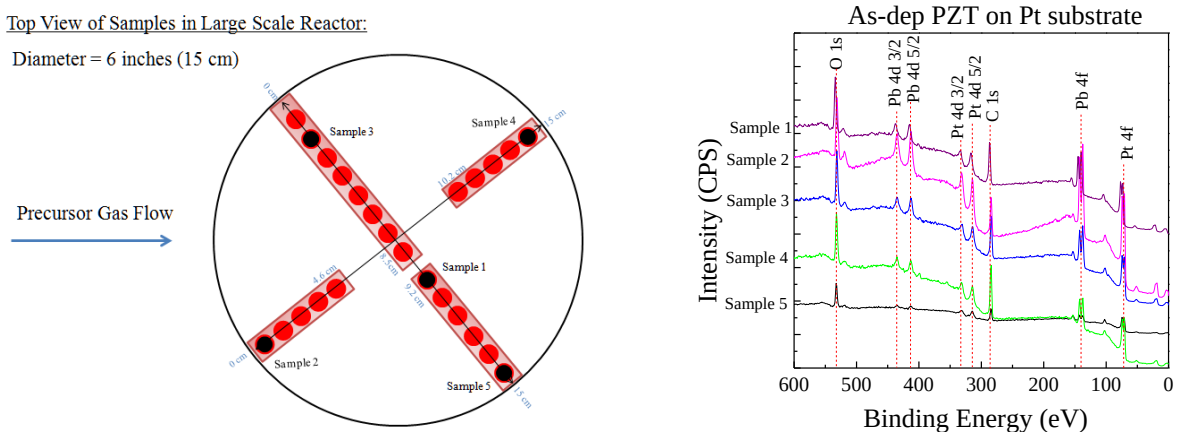

Figure 3-22. Large scale reactor: (a) position and (b) XPS survey scans of samples 1-5 deposited on platinized silicon substrate.

Compared to other deposition methods ALD is a capable technique for conformal coating and offers great control over stoichiometry and sub-nm thicknesses, but it is not meant for growing thick film with thicknesses in the hundreds of nanometers range. As such, one method that was explored to increase the throughput was developing a hybrid ALD/CVD process to enable thick PZT films. The conformality of CVD is a challenge because it depends on the reactive sticking probability of the precursor on the substrate. By using precursors that can grow films at low temperature and have high vapor pressure to saturate the surface, conformality can be improved (Kumar, Yanguas-Gil et al. 2008). Therefore, the goal was to first deposit a PZT seed layer via ALD to conformally coat 3D structures and then a PZT thick film is grown using a low-temperature CVD process, as it is easier to grow films on itself. XPS confirms that PZT growth was realized via CVD but not yet the desired Zr/Ti = 52/48 stoichiometry, as shown in Figure 3-23.

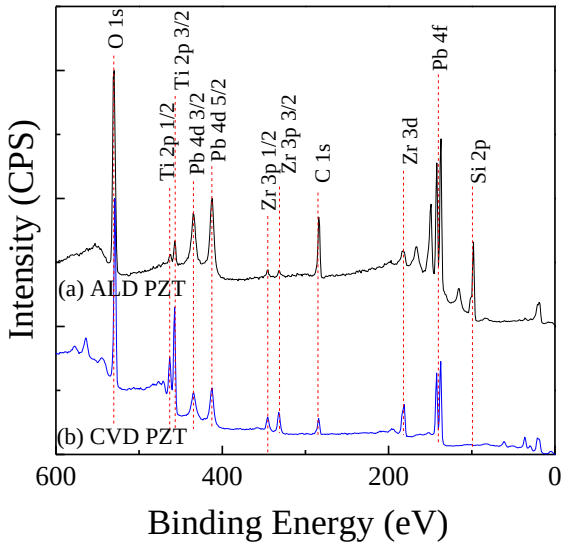

Figure 3-23. XPS survey scans for (a) ALD and (b) CVD as-deposited PZT thin films on Si (100) substrates.

Figure 3-24 is a SEM image of a PZT film grown by ALD/CVD hybrid process on 300 nm hollow Si_3N_4 cylinders with an aspect ratio up to 2.2.

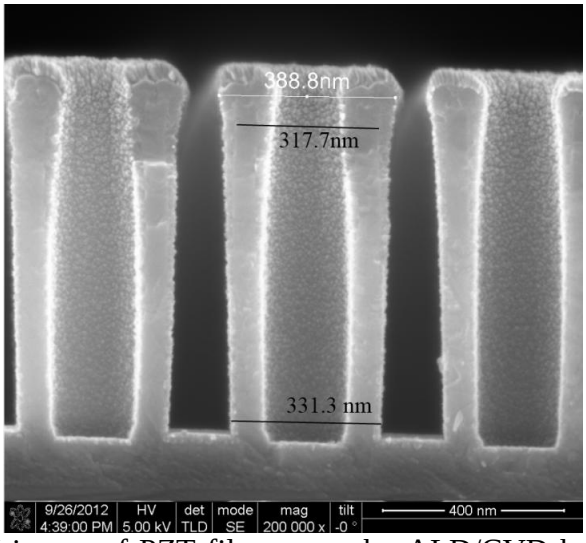

Figure 3-24. SEM image of PZT film grown by ALD/CVD hybrid process over 300 nm hollow Si_3N_4 cylinders with aspect ratio up to 2.2.

The SEM image shows the PZT film was 44 nm thick on the surface of the cylinder, and the thickness decreases from 26 nm to 9.3 nm going from top to bottom on the sidewall of the cylinder.

3.4 ALD PZT Thin Films over La_2XMnO6 (X = Ni or Co) Nanoparticles

ALD PZT thin films were deposited to coat ferromagnetic La_2NiMnO_6 (LNMO) and La_2CoMnO_6 (LCMO) nanoparticles to synthesize multiferroic core-shell nanoparticles. The LNMO and LCMO nanoparticles with average particle size of ~50 nm were prepared using a facile, environmentally friendly, scalable molten-salt reaction at 700°C in air (Mao 2012; Mao, Parsons et al. 2013). The LNMO and LCMO nanoparticles were suspended in an isopropyl alcohol solvent and a thin layer of the solution was pipetted onto Si substrates. Once the isopropyl alcohol solvent evaporated, a layer of the nanoparticles remained on the Si substrate for deposition. ALD PZT thin films with thicknesses of 9.7 nm were deposited over the layer of LNMO and LCMO nanoparticles and rapidly thermally annealed at 700°C for 1 minute in oxygen environment. XPS survey scans of as-deposited and RTA at 700°C ALD PZT films deposited on LNMO and LCMO nanoparticles are shown in Figure 3-25.

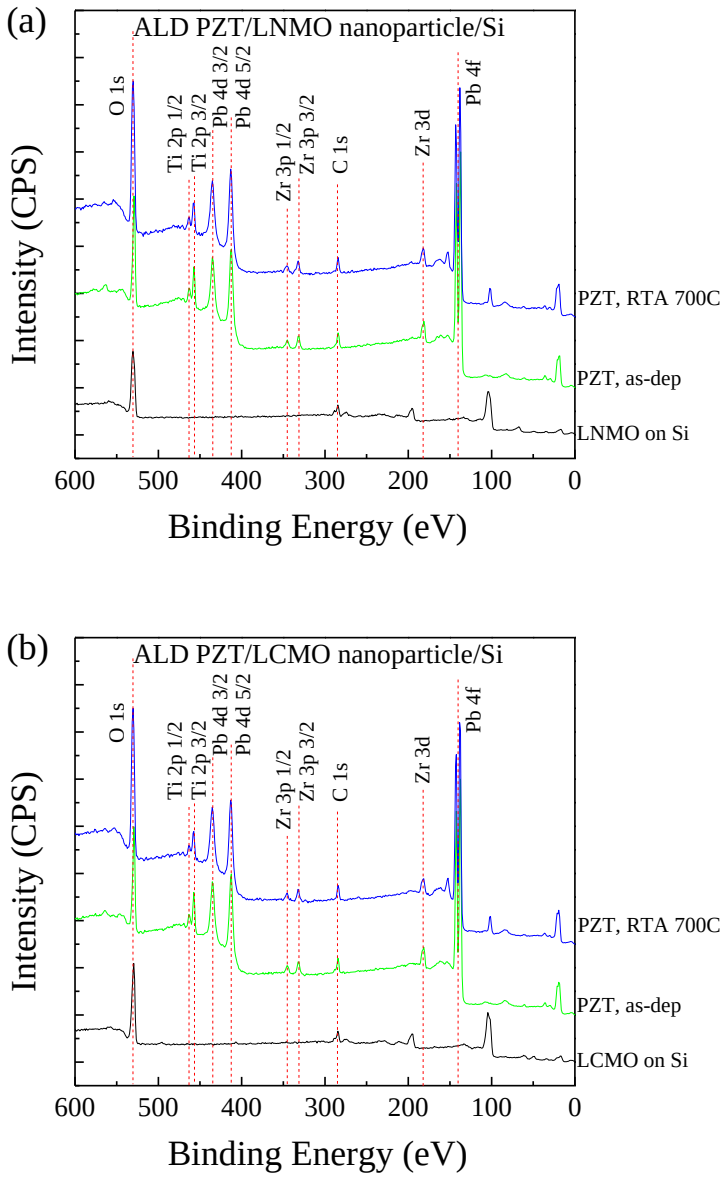

Figure 3-25. XPS survey scan of as-deposited and RTA at 700°C ALD PZT films on (a) LNMO nanoparticles and (b) LCMO nanoparticles on Si substrates.

Based on XPS, the ALD PZT thin film had a composition of Zr/Ti ratio of 30/70. The XRD scans of annealed PZT thin film on LNMO and LCMO nanoparticles were measured by the Panalytical X'Pert Pro X-ray Powder Diffractometer and are shown in Figure 3-26.

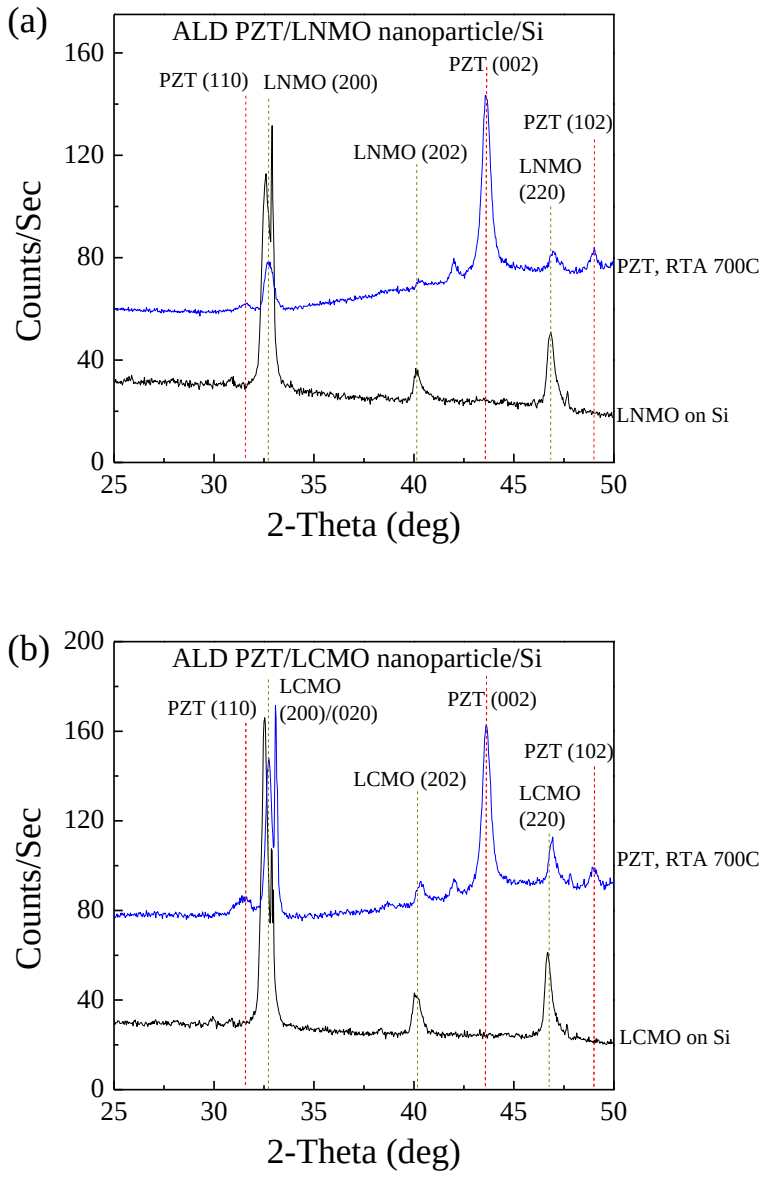

Figure 3-26. XRD scan of RTA at 700°C ALD PZT films on (a) LNMO nanoparticles and (b) LCMO nanoparticles on Si substrates.

The XRD scans of annealed PZT/nanoparticles showed PZT and corresponding nanoparticles crystalline peaks. HRTEM images of LNMO nanoparticles coated with ALD PZT thin films are shown in Figure 3-27.

(a) (b)

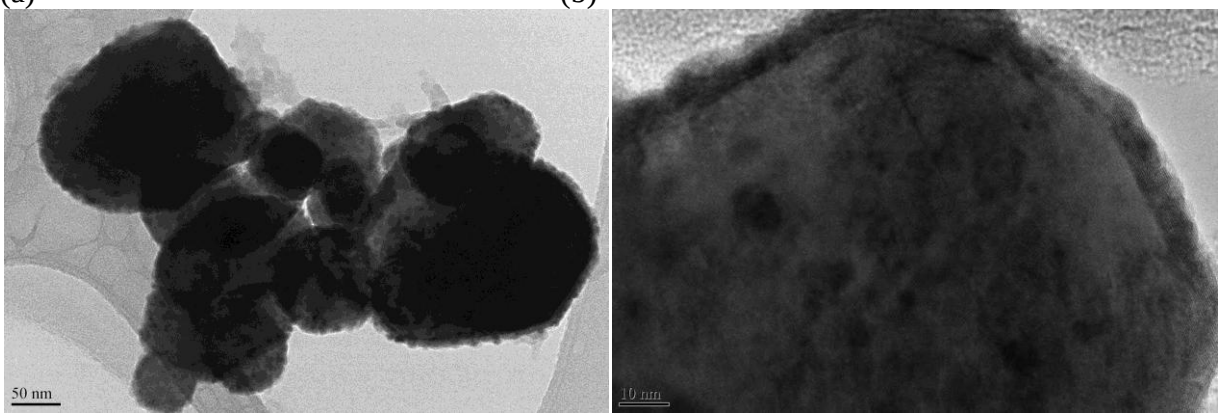

Figure 3-27. HRTEM images of ALD PZT films on LNMO nanoparticles at (a) low magnification and (b) high magnification.

The HRTEM images confirmed that the nanoparticles were coated with a crystalline thin film with a thickness of approximately 10 nm.

In summary, PZT films were deposited on silicon and platinized silicon substrates. ALD and CVD PZT films were deposited on silicon substrates to fabricate PZT MOS capacitor devices for C-V measurements in order to quantify the dielectric constants of the films. The conformality of ALD PZT thin films were confirmed over 300 nm hollow Si_3N_4 cylinders with an aspect ratio up to 2.2 and over silicon trenches with aspect ratio up to 8.5.

The (001) oriented PZT with MPB composition of Zr/Ti = 52/48 is desired because it has a higher transverse piezoelectric coefficient than (111) oriented PZT. The stoichiometry of PZT and $PbTiO_3$ thin films was determined via XPS. Near-desired composition was attained for annealed films, with a PZT composition of Pb = 58%, Zr = 19%, and Ti = 23% and a $PbTiO_3$ composition of Pb = 55% and Ti = 45%. A (100) textured ALD $PbTiO_3$ seed layer was successfully used as a template to attain an (100) oriented ALD PZT thin film on platinized silicon substrate. The crystallinity of (100) oriented PZT thin film and $PbTiO_3$ seed layer were confirmed by XRD measurements.

Additionally, the scalability of ALD PZT thin films over large 6-inch platinized silicon wafers and of CVD PZT thin films was realized. ALD PZT thin films were also deposited to coat La_2NiMnO_6 and La_2CoMnO_6 nanoparticles to make core-shell multiferroic nanoparticles.

CHAPTER 4. MAGNETOELECTRIC EFFECT IN PZT/CFO NANOCOMPOSITES

By controlling the composition, thickness, and conformality of ALD PZT thin films, multiferroic nanocomposites were engineered. Specifically, ALD PZT thin films were shown to uniformly coat the walls of nanoscale templated mesoporous CFO (with neck size of 6 nm in radius) to form a complex 0D-3D nanocomposite. XPS and XRD measurements confirmed the elemental analysis and crystallinity, respectively, of the PZT/CFO nanocomposites. To study the magnetoelectric coupling effect, the nanostructure was electrically poled ex-situ and the resulting magnetic moment was measured in superconducting quantum interference device (SQUID) magnetometer while sweeping in-plane and out-of-plane magnetic fields. The in-plane results show that there is no change in magnetization as a function of voltage, which is due to the effect of substrate clamping. The out-of-plane results show that the magnetization changes as a function of voltage. The mesoporous CFO coated with 3 nm thick PZT film shows a greater magnetization change than the 6 nm thick PZT film, suggesting that porosity in the templated mesoporous CFO matrix is needed for a greater magnetoelectric coupling effect.

4.1 ALD PZT Thin Films on Dense CFO Films

Our first goal was to characterize ALD PZT thin films for composition and crystallinity on flat, non-porous CFO films (hereafter called dense CFO films). The dense CFO films with thicknesses of 200 nm were deposited on silicon substrates via sol-gel method. Next, PZT thin films with thicknesses of 10 nm were deposited via ALD onto the dense CFO films. A XPS survey scan of ALD PZT/dense CFO that was annealed by RTA at 700°C for 1 minute in O_2 atmosphere is shown in Figure 4-1.

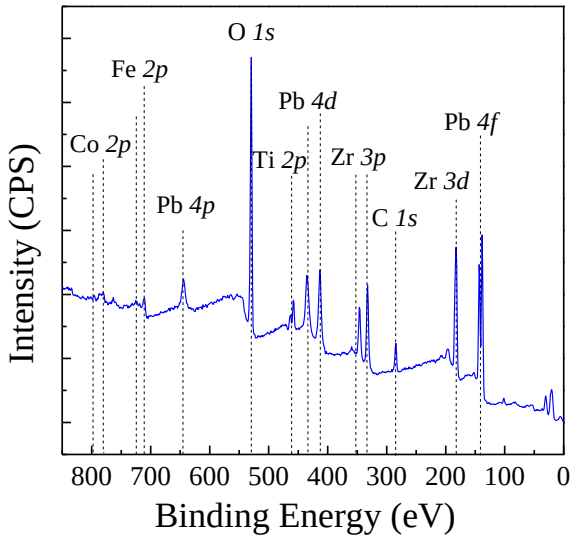

Figure 4-1. XPS survey scan of 10 nm thick ALD PZT film deposited on 200 nm thick sol-gel dense CFO film on a silicon substrate that was RTA at 700°C for 1 minute in O_2 environment.

The ALD PZT/dense CFO samples and ALD PZT/Pt reference samples were annealed at three different conditions under oxygen ambient: (1) furnace-annealed at 400°C for 30 minutes then at 700°C for 10 minutes, (2) RTA at 600°C for 1 minute, and (3) RTA at 700°C for 1 minute. The compositions of each sample were quantified by XPS and are shown in Figure 4-2.

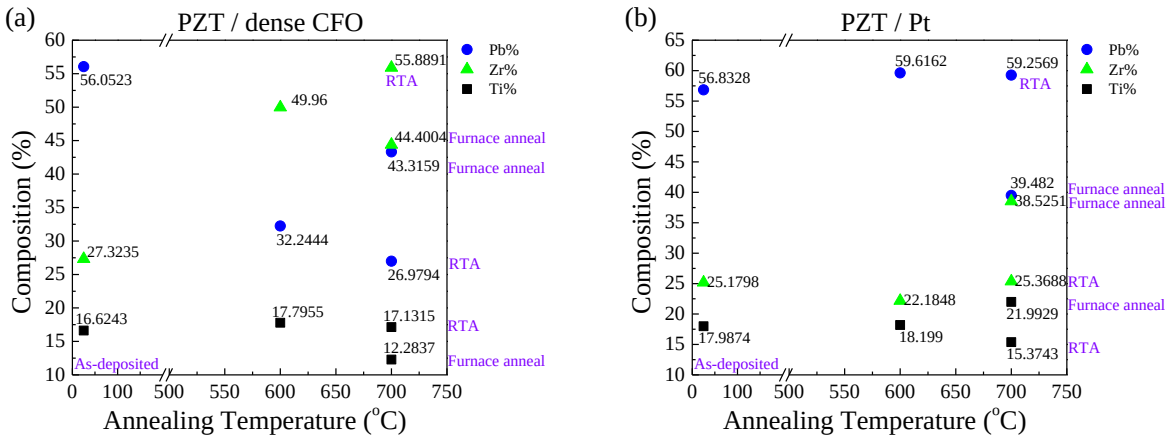

Figure 4-2. Compositions of as-deposited, furnace-annealed at 400°C for 30 minutes then at 700°C for 10 minutes, RTA at 600°C for 1 minute, and RTA at 700°C for 1 minute in O_2 environment samples of 10 nm thick ALD PZT deposited on (a) 200 nm thick dense CFO film and (b) platinized silicon substrate, to be used as reference samples.

The XPS analysis shows that the PZT composition becomes rich in Zr after annealing at the three different conditions, unlike the PZT/Pt reference samples. Because XPS is a surface sensitive technique with a penetration depth of 10 nm, and the dense CFO is 200 nm thick, energy-dispersive x-ray spectroscopy (EDX) was used to determine the PZT composition, as shown in Table 4-1.

Table 4-1. Composition of ALD PZT film deposited on dense CFO, quantified by XPS and EDX, and compared to composition of reference sample ALD PZT/Pt measured by XPS.

	Pb %	Ti %	Zr %
XPS of ALD PZT/dense CFO	19.9	22.2	57.9
EDX of ALD PZT/dense CFO	46.0	25.0	28.0
XPS of ALD PZT/Pt (reference)	55.4	19.7	24.9

The PZT composition of ALD PZT/dense CFO using EDX was similar to the reference sample of ALD PZT/Pt quantified by XPS, so the composition of the reference samples were

used to approximate the ALD PZT/dense CFO films. In order to obtain the desired PZT stoichiometry of Zr/Ti = 52/48, annealing the samples by RTA at 700°C for 1 minute in O_2 environment was chosen and used for all PZT/CFO multiferroic nanocomposites. The crystallinity of annealed ALD PZT/dense CFO were measured by using grazing incidence wide angle X-ray scattering (GIWAXS) collected at the Stanford Synchrotron Radiation Laboratory (SSRL) using beamline 11-3, as shown in Figure 4-3.

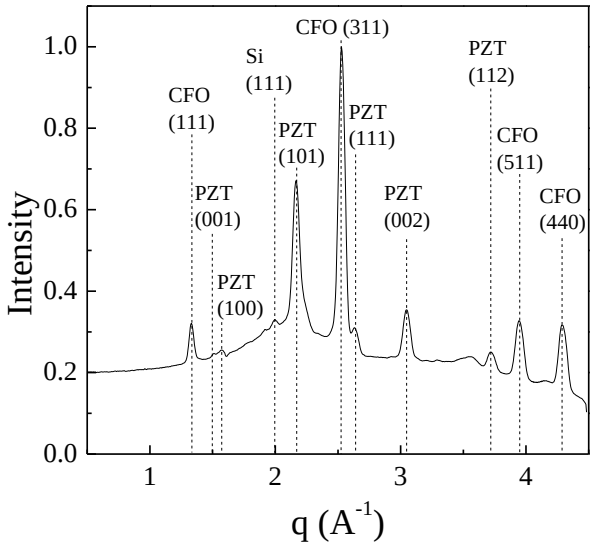

Figure 4-3. XRD survey scan of ALD PZT (6.2 nm)/dense CFO (200 nm)/Si sample that was RTA at 700°C for 1 minute in O_2 environment.

The XRD scan shows crystalline peaks for ALD PZT and dense CFO films, so ALD PZT thin films were then deposited into mesoporous CFO matrixes.

4.2 ALD PZT/Porous CFO Nanocomposites

At first, both the nanoporous host and the final composite material should be characterized. Approximately 100 nm thick mesoporous CFO is shown to have ordered pores through SEM – Figure 4-4.

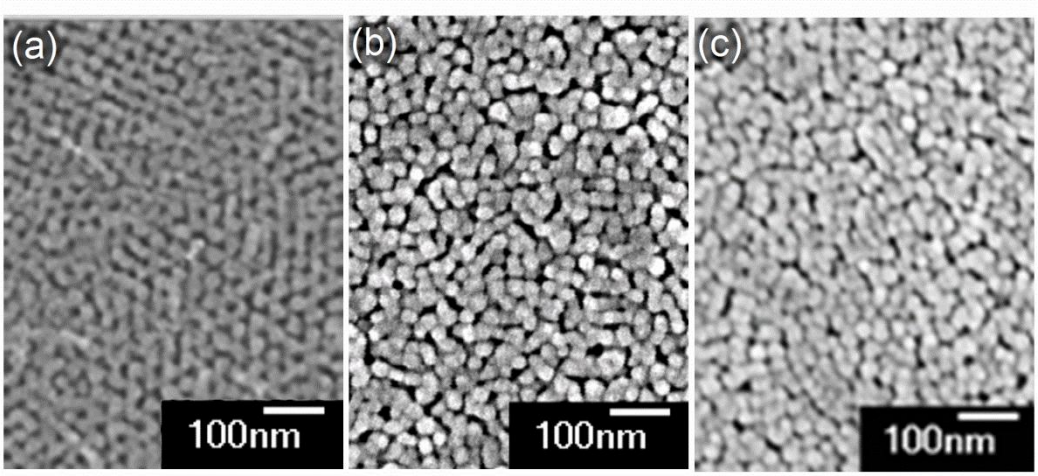

Figure 4-4. Tilted top view SEM images show (a) unfilled pores in the mesoporous CFO matrix, (b) as-deposited 3 nm ALD PZT in CFO pores, and (c) as-deposited 6 nm ALD PZT in CFO pores.

The pore radius is 9 nm in size and neck radius is 6 nm in size, confirmed by TEM and SEM. Then, 3 nm and 6 nm of ALD PZT were deposited onto the neck and pore walls of the CFO framework, as confirmed via SEM and shown in Figure 4-4 (b) and (c). The thicknesses of ALD PZT thin film were chosen based on the mesoporous CFO architecture. Because the neck radius is 6 nm, ALD PZT film with a thickness of 6 nm was chosen to fully coat the neck walls and avoid depositing an excessive and undesired layer of PZT thin film on top of the mesoporous CFO matrix. Note that the neck size can be completely filled with 6 nm of PZT and impede gas flow through the network, but the pores themselves should not be completely filled. Once the necks are filled, the gas reactants of the PZT do not have access into the pores, so the PZT starts depositing on the top of the mesoporous CFO matrix, which is undesirable. Therefore, 6 nm of PZT was chosen to be the thickest film to be deposited in the template mesoporous CFO matrix. Porosimetry measurements in Figure 4-5 (a) and (b) confirms that the porosity in the CFO framework was reduced from 30.42% to 0.37% upon 6-nm-thick ALD PZT deposition.

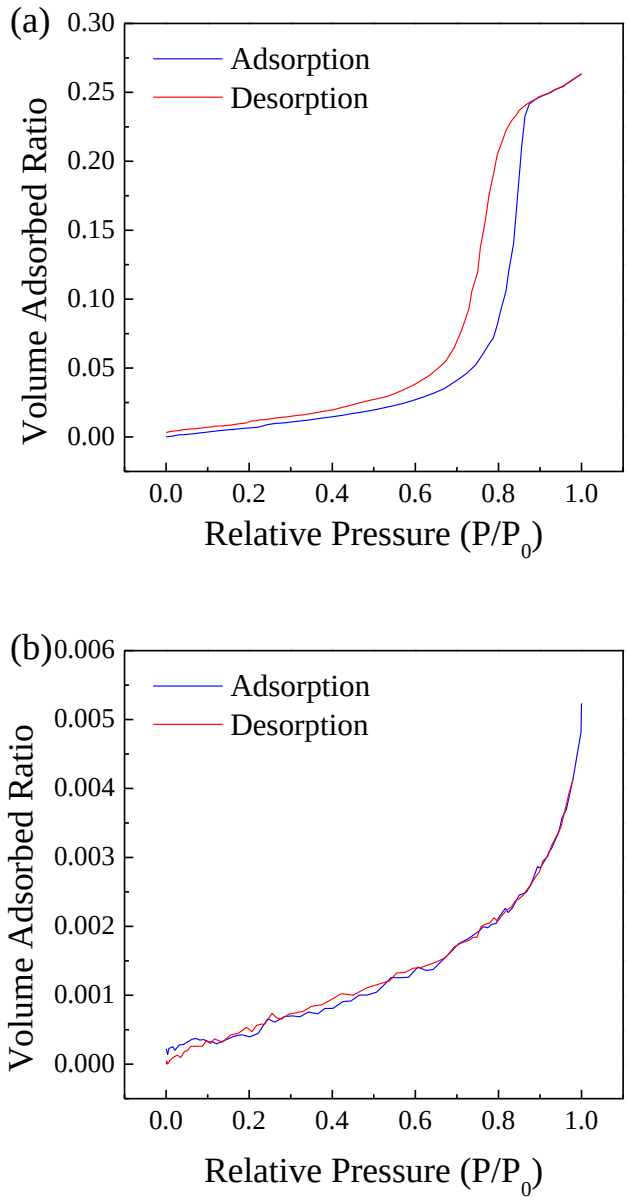

Figure 4-5. Volume adsorption isotherms and extracted porosity values for (a) unfilled mesoporous CFO matrix and (b) annealed 6 nm ALD PZT in CFO pores.

The thickness of 3 nm PZT was chosen so that the neck and pore walls were not fully coated, allowing more porosity in the mesoporous CFO when compared to the 6-nm-thick PZT film. The 3-nm-thick PZT film, however, shows comparable porosimetry measurements with the 6-nm-thick PZT film because the pores are sealed due to coarsening and grain growth upon

annealing. By comparing partially-filled CFO pores (with 3-nm-thick PZT) to mostly-filled CFO pores (with 6-nm-thick PZT), the effect of the amount of piezoelectric material (i.e. PZT) on the magnetoelectric coupling to the ferromagnetic material (i.e. CFO) can be studied. Thicker PZT film results in a decrease of porosity in the mesoporous CFO matrix.

ALD PZT thin film is deposited as an amorphous layer, so the samples are crystallized by rapid thermal annealing (RTA) at 700°C for 1 minute in an oxygen environment. XRD confirms that the CFO and PZT both have the correct crystalline structure, as shown in Figure 4-6, with average grain sizes of 55 Å and 60 Å, respectively.

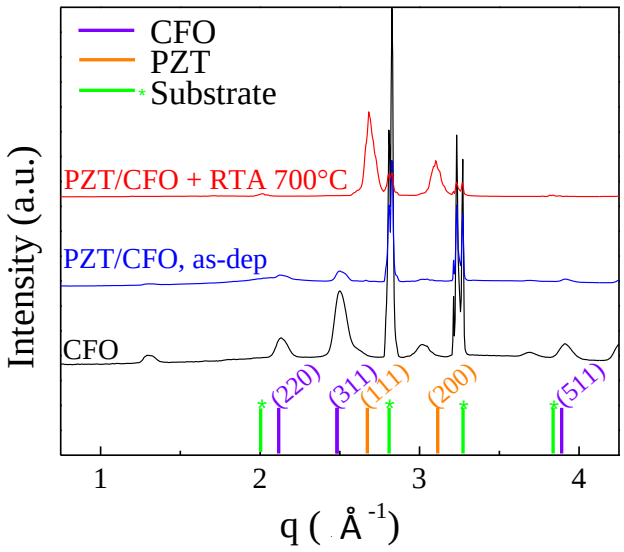

Figure 4-6. XRD shows that the as-deposited 6 nm PZT film on mesoporous CFO shows only the crystalline CFO peaks. After annealing at 700°C, PZT peaks (111) and (200) are seen in the sample.

Both the CFO and PZT phases are polycrystalline and show no preferential crystallographic orientations. XPS shows that PZT was deposited with composition Zr:Ti ratio of 60:40, as shown in Figure 4-7.

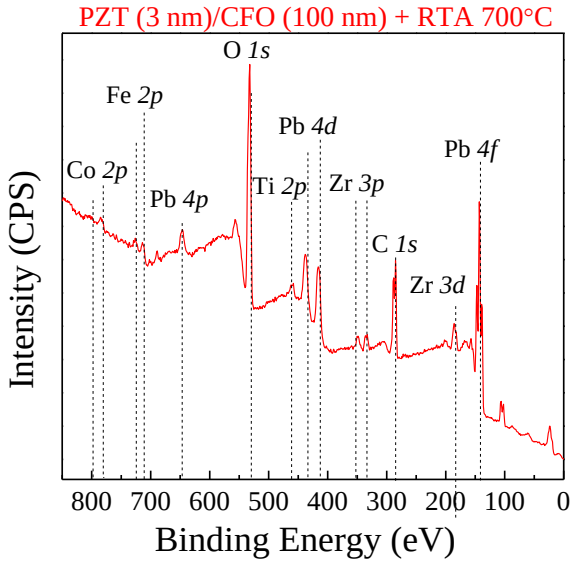

Figure 4-7. XPS survey of annealed 3 nm ALD PZT deposited on 100 nm porous CFO shows that the different elements are present in the sample.

As shown in Table 4-2, the XPS shows that the ALD PZT/mesoporous samples become Zr-rich after annealing the PZT film via rapid thermal annealing at 700°C in O_2 ambient for 1 minute at heating ramp rate of 4°C/sec. However, the ALD PZT/Pt samples did not show this same trend. XPS is an extremely surface sensitive technique with a penetration depth of approximately 10 nm. The mesoporous CFO is 100 nm thick, so energy-dispersive x-ray spectroscopy (EDX) with a larger penetration depth than XPS was performed on the samples to determine whether there was a high lead loss occurrence.

Table 4-2. PZT composition measured via XPS and EDX.

	XPS				EDX	
Sample	PZT/CFO PEP 500°C		PZT/Pt		PZT/CFO PEP 500°C	
Condition	As-Dep	RTA 700°C	As-Dep	RTA 700°C	As-Dep	RTA 700°C
Pb 4f %	52.7	27.8	53.8	58.9	58.5	55.0
Zr 3d %	29.1	54.9	28.8	25.1	23.6	26.0
Ti 2p %	18.2	17.3	17.4	16.0	17.9	18.0

Based on the EDX results, it appeared that the composition of the post-annealed ALD PZT/mesoporous CFO sample correlated well to the ALD PZT/Pt reference sample's composition measured by XPS. Therefore, the XPS composition of the annealed ALD PZT/Pt reference samples was used to approximate the composition of post-annealed ALD PZT/mesoporous CFO samples.

TEM spot scans from the bottom to top of the nanocomposite were done, and show that all the elements of PZT and CFO are present. Energy-dispersive x-ray spectroscopy (EDS) was performed to do an elemental mapping of a 39 × 38 nm^2 area of 3-nm-thick PZT in mesoporous CFO matrix, as shown in Figure 4-8.

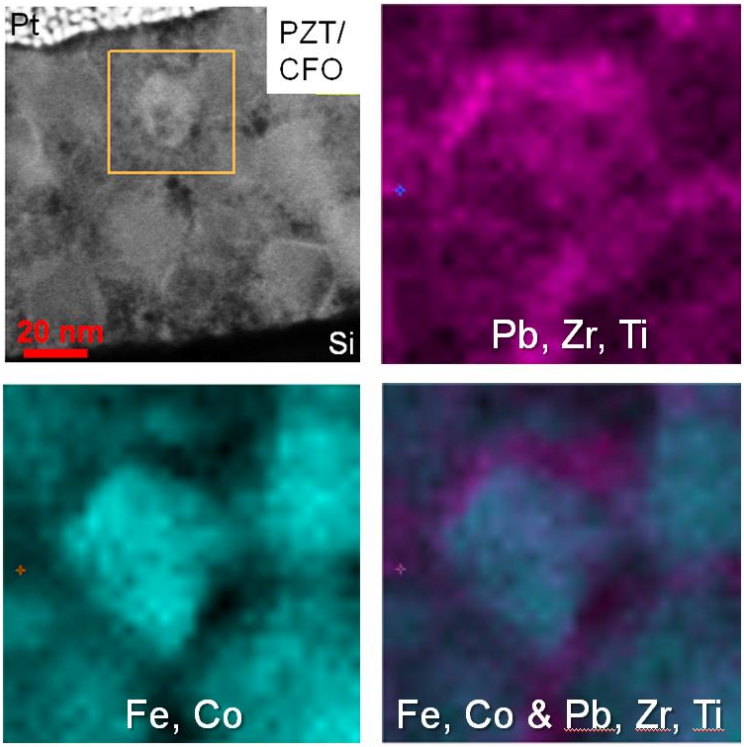

Figure 4-8. Cross-sectional TEM Cross-sectional TEM of 3 nm ALD PZT in porous CFO. Box inset shows 39 × 38 nm^2 EDS map of Pb/Zr/Ti, Fe/Co, and overlay of the two.

In order to prepare the sample for TEM, Pt was deposited over the nanocomposite. The EDS map confirms that PZT was deposited and coated the necks and pores all the way through the 100 nm thick mesoporous CFO.

4.3 Magnetoelectric Effect in PZT/CFO Nanocomposites

In synthesizing magnetoelectric nanocomposites, it is important to determine the effect of the deposition of ALD PZT thin film on the mesoporous CFO's magnetic properties. Mesoporous CFO matrix without PZT deposited in the pores was observed to have a small preference for in-plane magnetization, based on SQUID magnetometry studies, as shown in Figure 4-9.

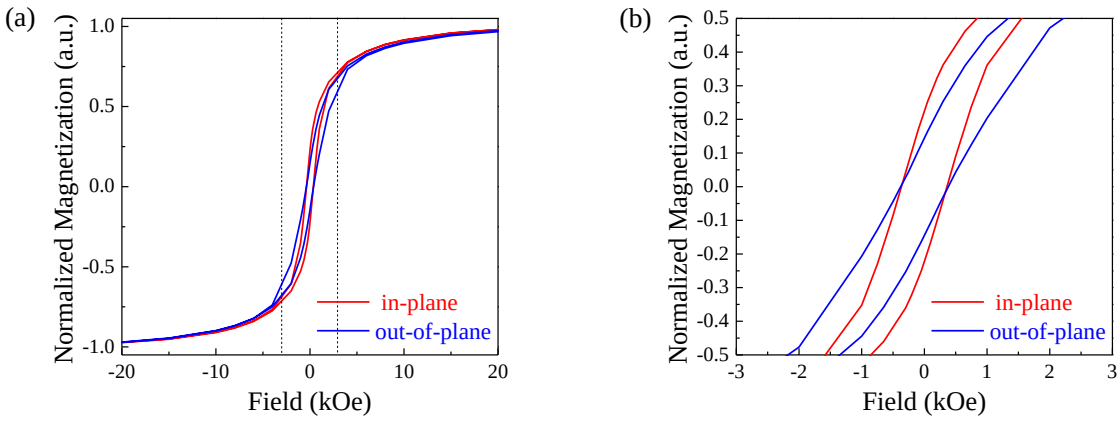

Figure 4-9. SQUID of 100 nm thick mesoporous CFO with pore diameter of 18 nm and neck diameter of 12 nm in size. (b) is a zoomed-in view of (a) at magnetic fields from -3 to 3 kOe.

As shown in Figure 4-11, as-deposited PZT/CFO nanocomposite showed the same magnetic trend as mesoporous CFO matrix. After annealing the nanocomposite at 700°C, however, it becomes magnetically anisotropic with a preference for out-of-plane magnetization.

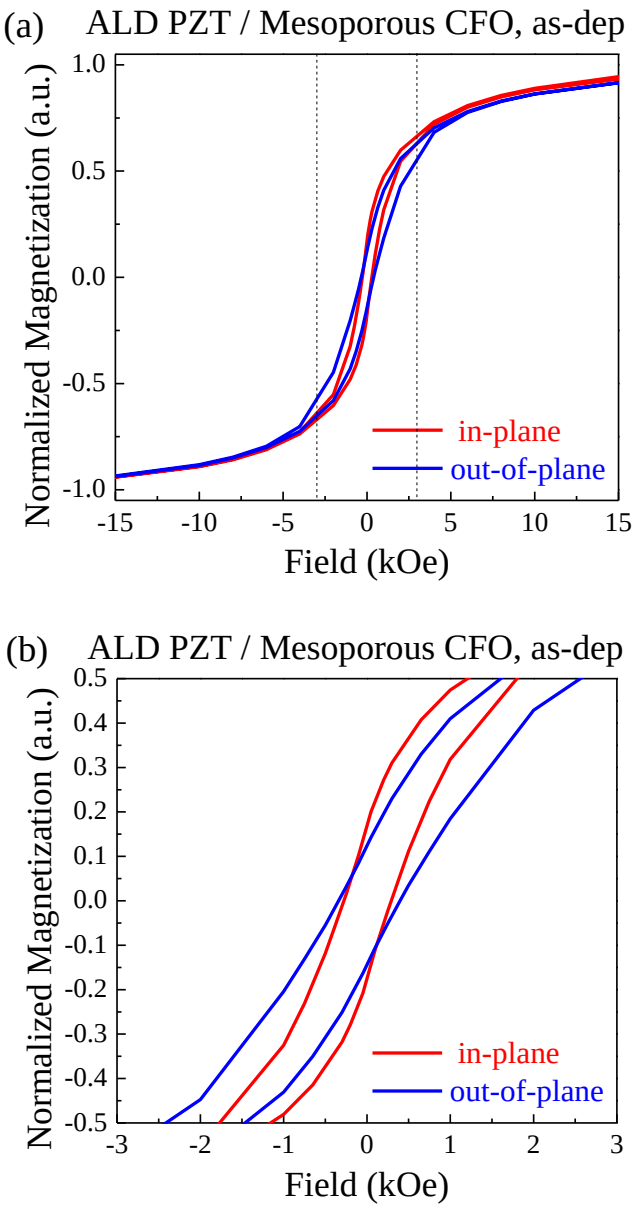

Figure 4-10. SQUID of mesoporous CFO filled with as-deposited ALD PZT. (b) is a zoomed-in view of (a), at magnetic fields from -3 to 3 kOe. As-deposited ALD PZT did not affect magnetic property of mesoporous CFO.

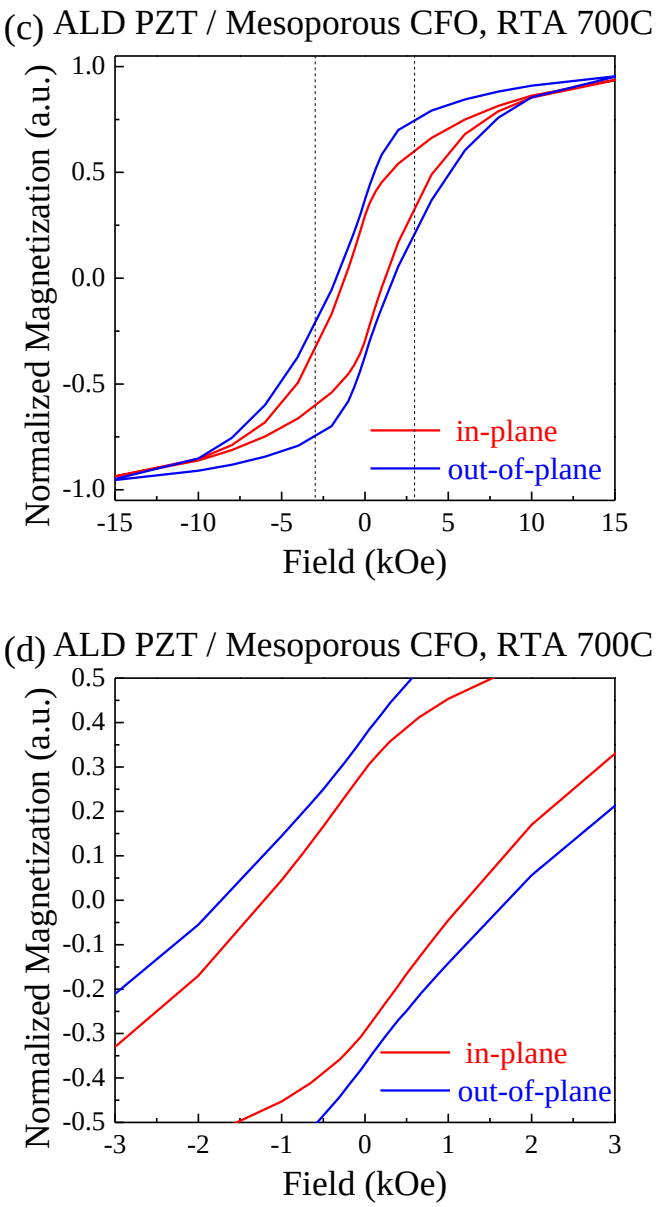

Figure 4-11 (Continued). SQUID of mesoporous CFO filled with ALD PZT annealed at 700°C. (d) is a zoomed-in view of (c) at magnetic fields from -3 to 3 kOe. Annealed ALD PZT induced out-of-plane magnetic anisotropy.

As shown in previous work (Quickel, Le et al. 2010), mesoporous CFO is mechanically flexible and the pores can only flex out-of-plane because substrate clamping prevents the pores from flexing in-plane direction. CFO exhibits negative magnetostriction, which means that as CFO is strained, the magnetization aligns with the compressive direction.

In order to observe the effect of magnetoelectric coupling in the PZT/CFO nanocomposite, the samples were poled with applied electric fields E_{eff} ranging 0–1.42 MV/m in an *ex situ* poling set-up. E_{eff} was calculated by dividing the applied voltage V (0–200 V) with the total thickness d (100 nm) of the PZT/CFO nanocomposite. Because the entire sample was poled, magnetization could then be measured in a SQUID magnetometer in-plane (i.e. parallel to the sample surface and perpendicular to the applied electric field) and out-of-plane (i.e. perpendicular to the sample surface and parallel to the applied electric field). Change in magnetic moments as a function of electric field for partially-filled CFO pores (with 3 nm thick PZT) are shown in Figure 4-13 (a) (in-plane) and (b) (out-of-plane) and mostly-filled CFO pores (with 6 nm thick PZT) are shown in Figure 4-13 (c) (in-plane) and (d) (out-of-plane).

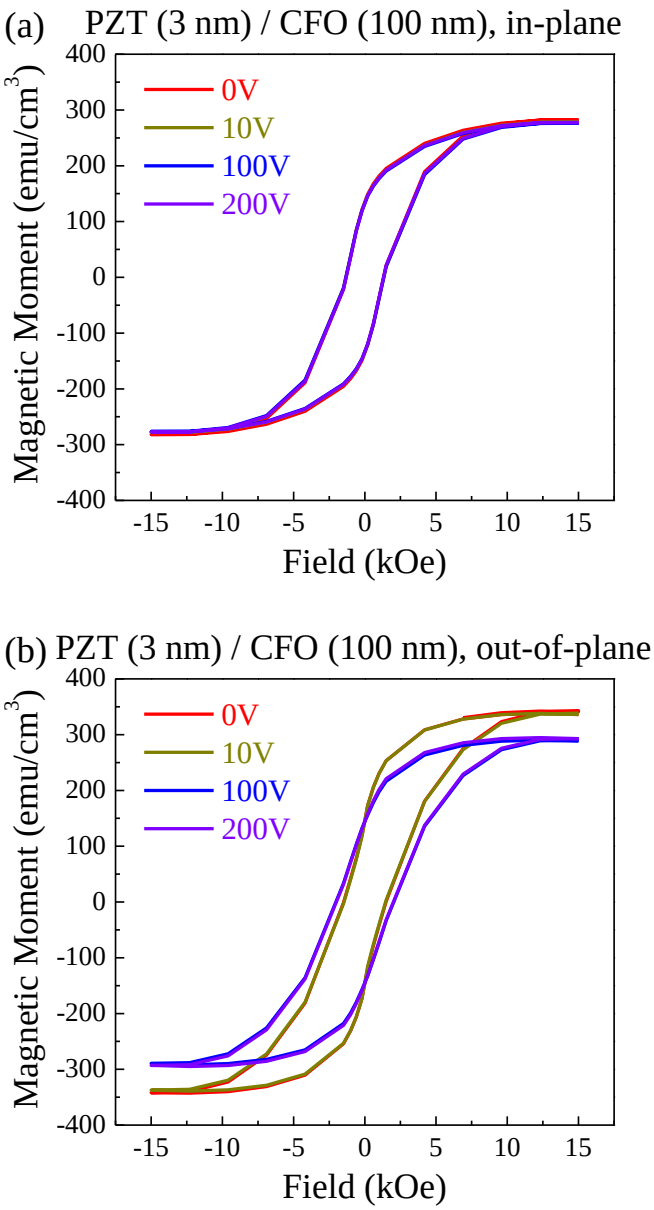

Figure 4-12. Porous CFO filled with 3 nm ALD PZT and annealed at 700°C. CFO pores had neck size of 12 nm diameter, and pore size of 15 nm diameter. The samples were ex-situ poled with 0-200 V and the magnetic moment was measured in SQUID with (a) in-plane magnetic field and (b) out-of-plane magnetic field. The applied voltages of 0, 10, 40, 100, and 200 V correspond with applied electrical fields, E_{eff}, of 0, 0.07, 0.28, 0.71, and 1.42 MV/m, respectively.

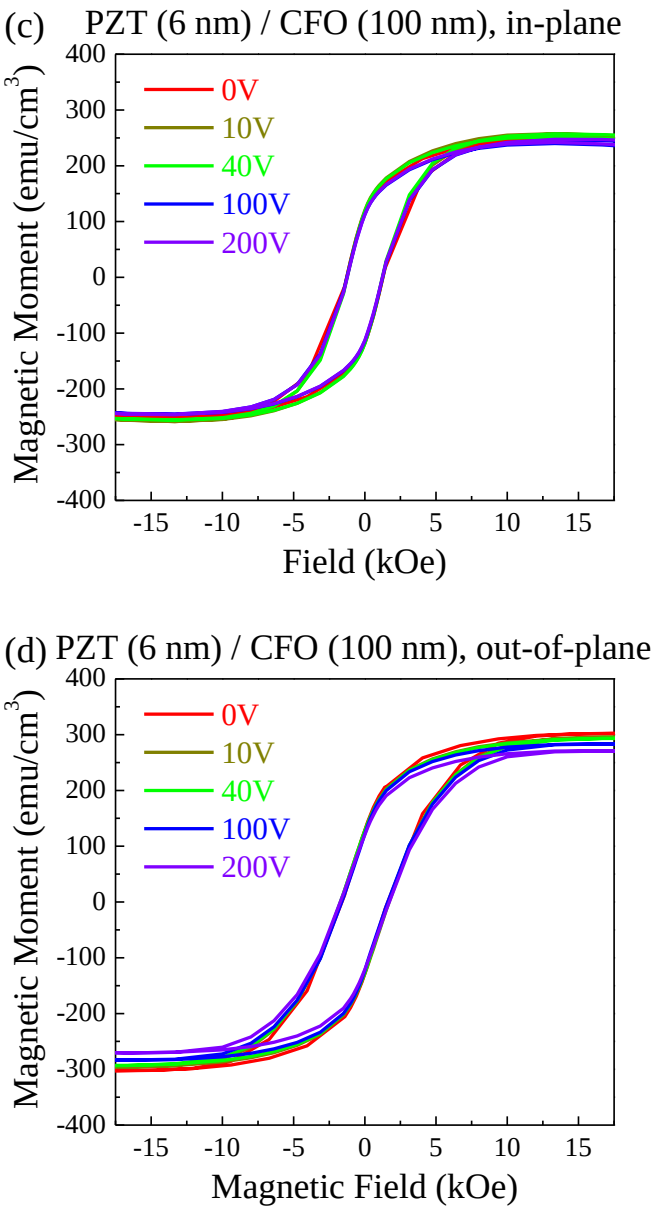

Figure 4-13 (Continued). Porous CFO filled with 6 nm ALD PZT and annealed at 700°C. CFO pores had neck size of 12 nm diameter, and pore size of 15 nm diameter. The samples were ex-situ poled with 0-200 V and the magnetic moment was measured in SQUID with (c) in-plane magnetic field and (d) out-of-plane magnetic field. The applied voltages of 0, 10, 40, 100, and 200 V correspond with applied electrical fields, E_{eff}, of 0, 0.07, 0.28, 0.71, and 1.42 MV/m, respectively.

Figure 4-14 shows the percentage change in saturation magnetization dependent on applied electric field.

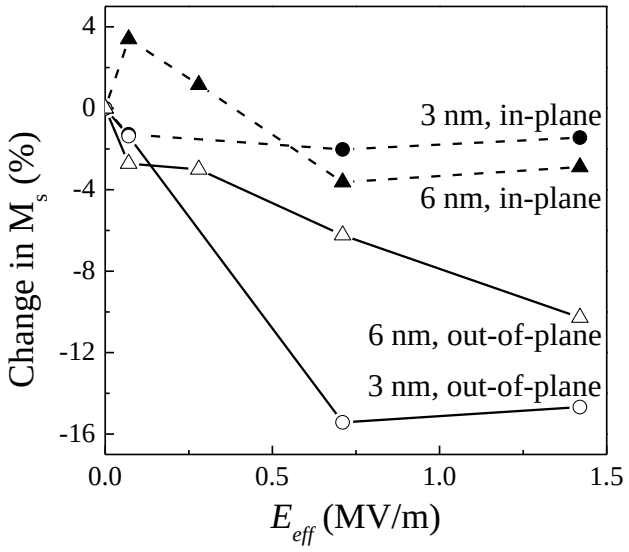

Figure 4-14. Shows the percentage change in M_s (relative to M_s at 0 V) versus E_{eff}. In-plane shows relatively no change in M_s (1.2-3.6%) and out-of-plane shows 3 nm thick PZT has greater change of 15.4% than 6 nm thick PZT change of 10.3%.

The applied voltages of 0, 10, 40, 100, and 200 V correspond with electrical fields of 0, 0.07, 0.28, 0.71, and 1.42 MV/m, respectively. In both nanocomposites, the in-plane results show that there is no significant change in magnetization (1.2–3.6%) as a function of electric field. This was expected due to the effect of substrate clamping (substrate thickness of 0.5 mm) on the 100-nm-thick nanocomposite.

On the other hand, the out-of-plane magnetization is not subject to in-plane clamping. We expected that the composite with the thicker PZT layer would be able to generate a greater strain against the CFO framework, triggering a larger change in magnetization. Instead, the mesoporous CFO coated with 3-nm-thick PZT film shows a greater saturation magnetization change of 15.4% compared to the 6-nm-thick PZT film of 10.3%. It is believed that the 3-nm-PZT system with its pores only partially filled retains more mechanical flexibility compared to the 6-nm-PZT composite, which behaves more closely to a bulk magnetoelectric without

porosity. This added flexibility would in turn enable greater strain changes to propagate through the composite film, enhancing the magnetoelectric coupling effect. The inverse magnetoelectric coupling coefficient calculated for the partially-filled CFO pores (with 3 nm thick PZT) was determined to be 85.6 Oe-cm/mV, which is larger than the literature reported value for 0D-3D composites, as shown in Table 4-3.

Table 4-3. Magnetoelectric coupling coefficient for different nanocomposite architectures for PZT/CFO multiferroics with references [1](He, Ma et al. 2009), [2](Wan, Wang et al. 2005), and [3](Wan, Zhang et al. 2006).

α_E (mV/cm-Oe)	2-2[1]	1-3[2]	0-3[3]
PZT/CFO (thickness)	70 (270 nm)	317 (400 nm)	30 (1000 nm)

The mostly-filled CFO pores (with 6 nm thick PZT) was measured at Stanford Synchrotron Radiation Lightsource (SSRL) at beamline 7-2 to determine the strain states of the PZT/CFO nanocomposites before and after poling. The CFO (311) and PZT (200) peaks were measured at 0 V (unpoled state) and 100 V (poled state), as shown in Figure 4-16.

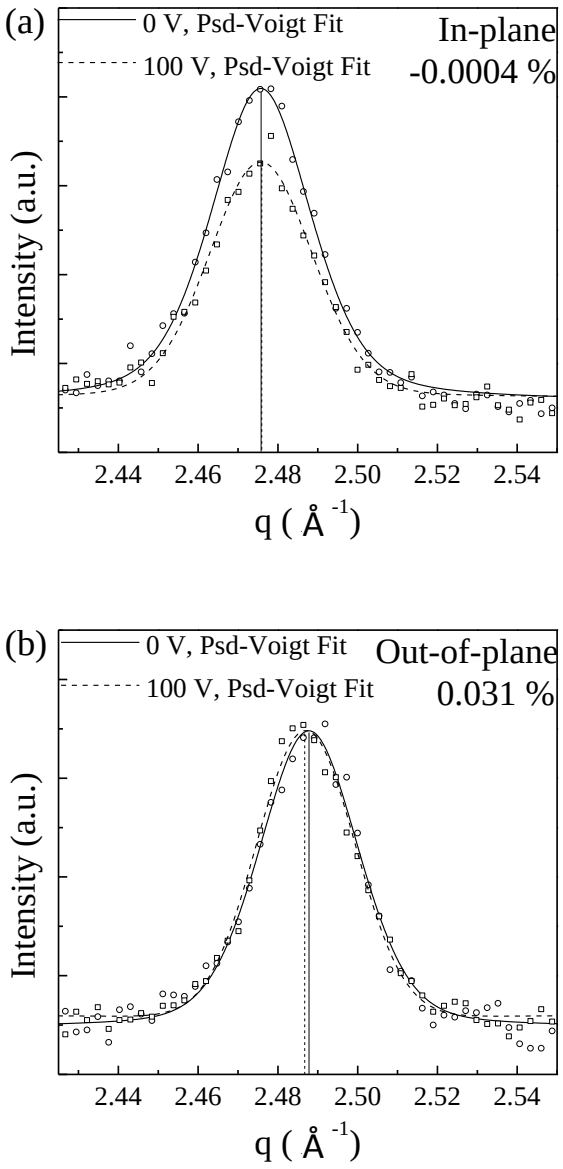

Figure 4-15. Porous CFO filled with 6 nm ALD PZT and annealed at 700^{o}C. (a-b) CFO (311) peaks were measured at before (0 V) and after (100 V) poling at SSRL BL 7-2. (a) were measured in the in-plane direction and (b) were measured in the out-of-plane direction.

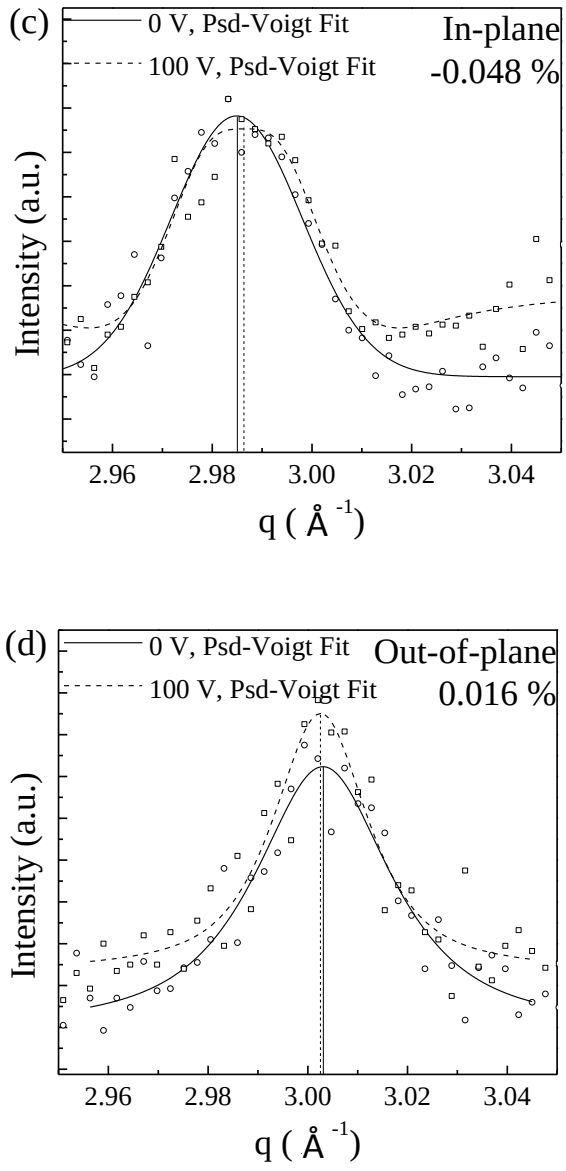

Figure 4-16 (Continued). Porous CFO filled with 6 nm ALD PZT and annealed at 700^{o}C. (c-d) PZT (200) peaks were measured at before (0 V) and after (100 V) poling at SSRL BL 7-2. (c) were measured in the in-plane direction and (d) were measured in the out-of-plane direction.

The peaks were fitted with Pseudo-Voigt to determine the center peak position, which was then used to calculate the change in PZT and CFO lattice spacings using Bragg's law, as shown in Table 4-4.

Table 4-4. Center peak position was determined by Pseudo-Voigt fitting of CFO (311) and PZT (200) peaks. The d-spacing was calculated by using Bragg's law the percentage change in strain is shown.

		0 V		100 V		
		Center peak position	d-spacing	Center peak position	d-spacing	% change in strain
In-plane	CFO (311)	2.476 $Å^{-1}$	2.538 Å	2.476 $Å^{-1}$	2.538 Å	-0.0004 %
	PZT (200)	2.985 $Å^{-1}$	2.105 Å	2.986 $Å^{-1}$	2.104 Å	-0.048 %
Out-of-plane	CFO (311)	2.488 $Å^{-1}$	2.526 Å	2.487 $Å^{-1}$	2.526 Å	0.031 %
	PZT (200)	3.003 $Å^{-1}$	2.092 Å	3.003 $Å^{-1}$	2.093 Å	0.016 %

The in-plane peaks showed minimal change while the out-of-plane peaks showed increasing CFO and PZT lattice spacings. The change in d-spacing indicated that the PZT crystal structure had changed due to poling with an applied electric field, and the strain was transferred to CFO to change its crystal structure; thus confirming the magnetoelectric coupling effect in ALD PZT/mesoporous CFO multiferroic nanocomposites.

Generally, sol-gel and gas-phase deposition methods have been formally used to engineer multiferroic nanocomposites. However, this is the first demonstration of the magnetoelectric effect in multiferroic nanostructures comprising of porosity. Although further studies need to be made, this work shows that combining ALD and wet chemistry techniques provides the capability of synthesizing nanocomposites with complex porous three-dimensional architecture that demonstrates the magnetoelectric effect; thereby allowing an additional parameter (i.e. porosity) to be explored in future nanocomposites.

CHAPTER 5. APPLICATION OF ALD PZT IN MEMORY DEVICE

In this work, the growth of MTJ stacks with an MgO/PZT/MgO tunnel barrier using a combination of sputtering and atomic layer deposition (ALD) techniques was shown to be a viable process. First, an 18 nm thick Ta layer was deposited as the MTJ bottom electrode on thermally oxidized Si substrates, and then a $Co_{20}Fe_{60}B_{20}$ free layer (out-of-plane magnetically anisotropic) was sputtered. For the MgO MTJ, a 2.5 nm thick MgO tunnel barrier was then sputtered. A $Co_{20}Fe_{60}B_{20}$ fixed layer (in-plane magnetically anisotropic) and capping layers of Ta and Pt were then sputtered on top of the tunnel barrier. For the PZT MTJ, a 1.5 nm thick PZT film was deposited via ALD with an atomic Zr:Ti ratio of 52/48 between two layers of 1.0 nm thick sputtered MgO to form the MgO/PZT/MgO tunnel barrier. The PZT thin film was deposited by ALD at a substrate temperature of 250°C with $Pb(tmhd)_2$, $Zr(tmhd)_4$, and $Ti(O^{i}Pr)_2(tmhd)_2$ as metalorganic precursors and deionized H_2O vapor as the oxidant.

The perpendicular magnetic anisotropy of the bottom free magnetic $Co_{20}Fe_{60}B_{20}$ layer was verified via superconducting quantum interference device magnetometry, confirming that the ALD PZT deposition process is a viable method for synthesizing PZT MTJs. The TMR ratio and VCMA effect were measured by sweeping an in-plane magnetic field from 0-3000 Oe while varying the applied voltage from -300-300 mV. The MgO MTJs were measured to have a tunneling magnetoresistance (TMR) ratio of 61.5% and a VCMA coefficient ($\xi_{average}$) of 14.3 ± 2.7 fJ/V-m, whereas the PZT MTJs were measured to have a TMR ratio of 53.1% and a $\xi_{average}$ of 19.8 ± 1.3 fJ/V-m. The VCMA coefficient of PZT MTJs was 38.5% larger than those of MgO MTJs. In conclusion, PZT MTJs were demonstrated to have tunneling magnetoresistance and an enhanced VCMA effect, making them being potential candidates for future voltage-controlled, ultralow-power, high-density memory devices.

5.1 TMR and enhanced VCMA effect in PZT MTJs

First, material properties of the MTJ stacks were characterized using Kratos AXIS X-ray photoelectron spectroscopy (XPS) and FEI Titan scanning transmission electron microscopy (STEM). XPS confirmed the composition ratio Zr:Ti = 52:48 of the PZT thin film deposited on a film stack with only the bottom free CoFeB layer, which consisted of Ta(18nm)/CoFeB(0.8nm)/MgO(1.0nm), as shown in Figure 5-1.

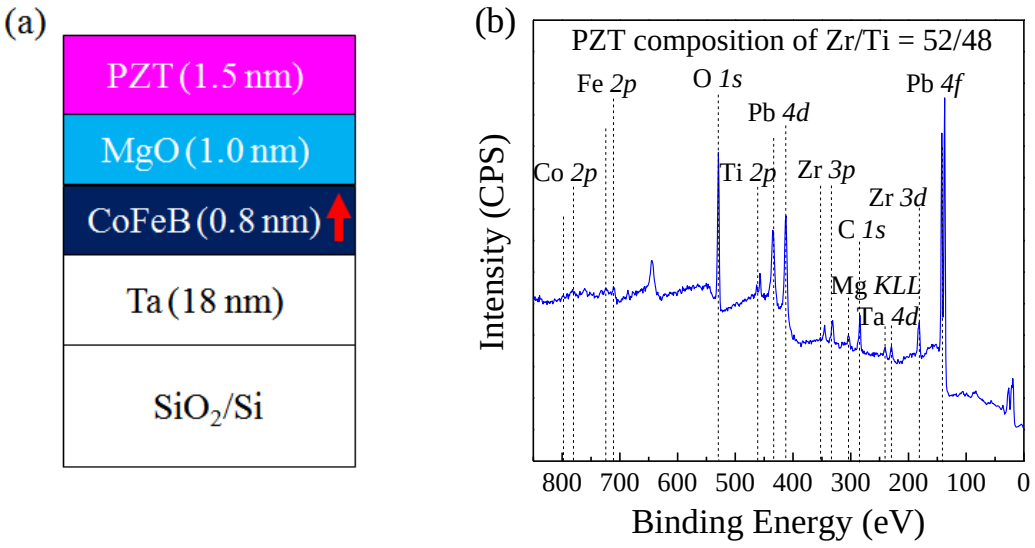

Figure 5-1. (a) Schematic of stack, with arrow denoting the CoFeB layer to be perpendicular magnetically anisotropic, and (b) XPS survey scan of 1.5 nm thick PZT deposited on MTJ bottom stack layers of Ta (18nm)/CoFeB (0.8nm)/MgO (1.0nm) and annealed at 200°C for 30 minutes. PZT has composition of Zr:Ti = 52:48.

Note that it has been shown that PZT exhibits enhanced properties (e.g. dielectric) at the morphotropic phase boundary, i.e. Zr:Ti = 52:48 composition (Jaffe, Cook et al. 1971). The XPS survey scan also showed the Mg *KLL*, Co *2p*, Fe *2p*, and Ta *4d* elemental peaks. Note that the B *1s* peak was not observed here because the estimated XPS penetration depth is 10 nm and the boron presumably diffused into the Ta layer due to annealing process (Miyajima, Ibusuki et al.

2009; Karthik, Takahashi et al. 2012). Cross-sectional TEM was performed on the fabricated MgO MTJ and PZT MTJ devices, as shown in Figure 5-2 (a) and (b), respectively.

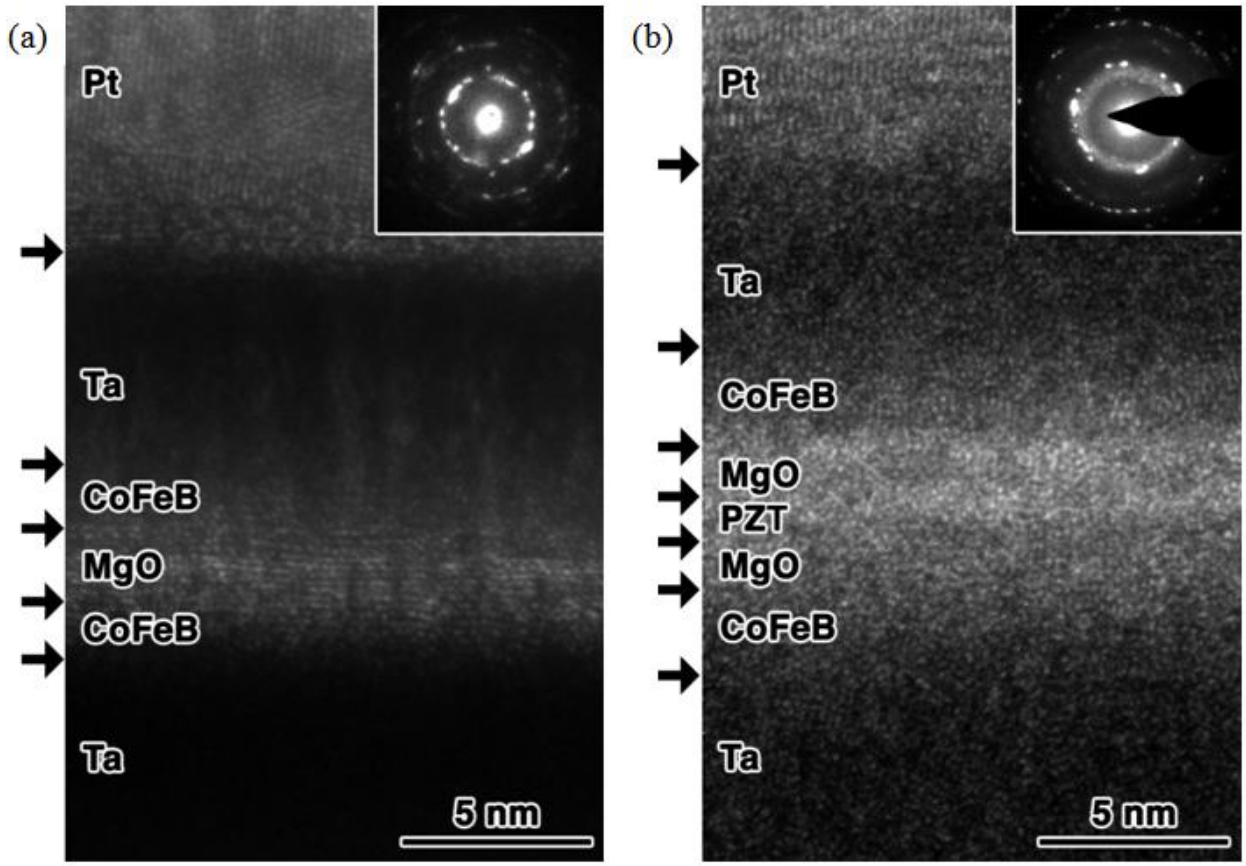

Figure 5-2. TEM of (a) MgO MTJ annealed at 250°C for 30 min and (b) PZT MTJ annealed at 200°C for 30 min.

Nano-diffraction were collected for both cross-sections. A selected-area aperture was used for the MgO MTJ, but in order to maximize diffracted intensity from the ~3 nm thick MgO/PZT/MgO layers-of-interest in the PZT MTJ, a highly condensed probe was employed, elongating along the in-plane direction of the film, which provided informative results due to the FEI Titan's parallel beam nearly all the way to crossover. The inset diffraction patterns clearly showed that the MgO had crystallized; however, indexing of the remaining spots to either CoFeB or PZT was not possible due to resolution limitations.

Next, unpatterned MgO and PZT MTJ stacks were characterized for their magnetic properties using Quantum Design MPMS superconducting quantum interference device (SQUID) magnetometer while sweeping out-of-plane magnetic field to ± 3 kOe. The saturation magnetization (M_s) of the 0.9 nm thick free CoFeB layer was obtained after subtracting the linear background containing diamagnetic signals from non-magnetic materials as well as the in-plane magnetized fixed CoFeB layer. The M_s was measured to be 1017 ± 22 emu/cm^3 and 931.7 ± 41 emu/cm^3 for MgO and PZT MTJ stacks, respectively, as shown in Figure 5-3.

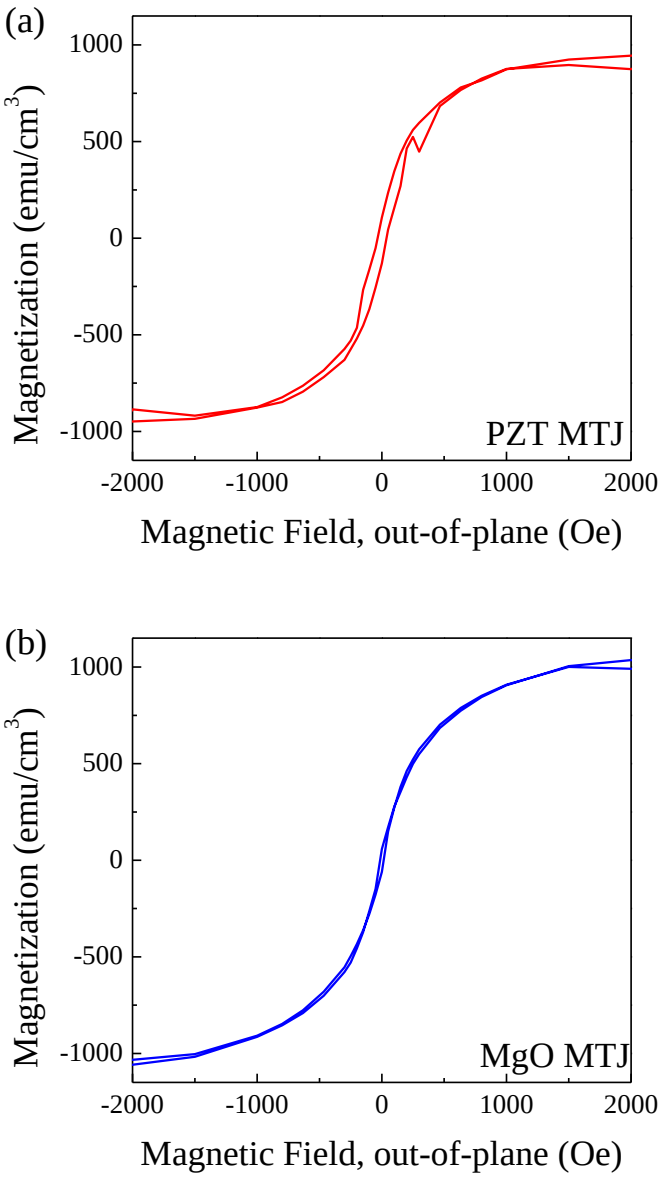

Figure 5-3. SQUID of (a) PZT MTJ and (b) MgO MTJ with magnetic field in out-of-plane direction.

The MTJs were then measured electrically to investigate the VCMA effect via TMR readout at room temperature using a three point probe configuration to exclude the bottom electrode resistance (Shiota, Murakami et al. 2011; Shiota, Bonell et al. 2013). The resistance was measured as the in-plane magnetic field was swept from 0 to 3000 Oe while voltages were

applied between -300 to +300 mV, as shown in Figure 5-4 (a) and (b). The resistance-area (RA) product of the PZT and MgO MTJ in Figure 5-4 (a) and (b) was 125 $k\Omega \cdot \mu m^2$ and 19 $k\Omega \cdot \mu m^2$, respectively.

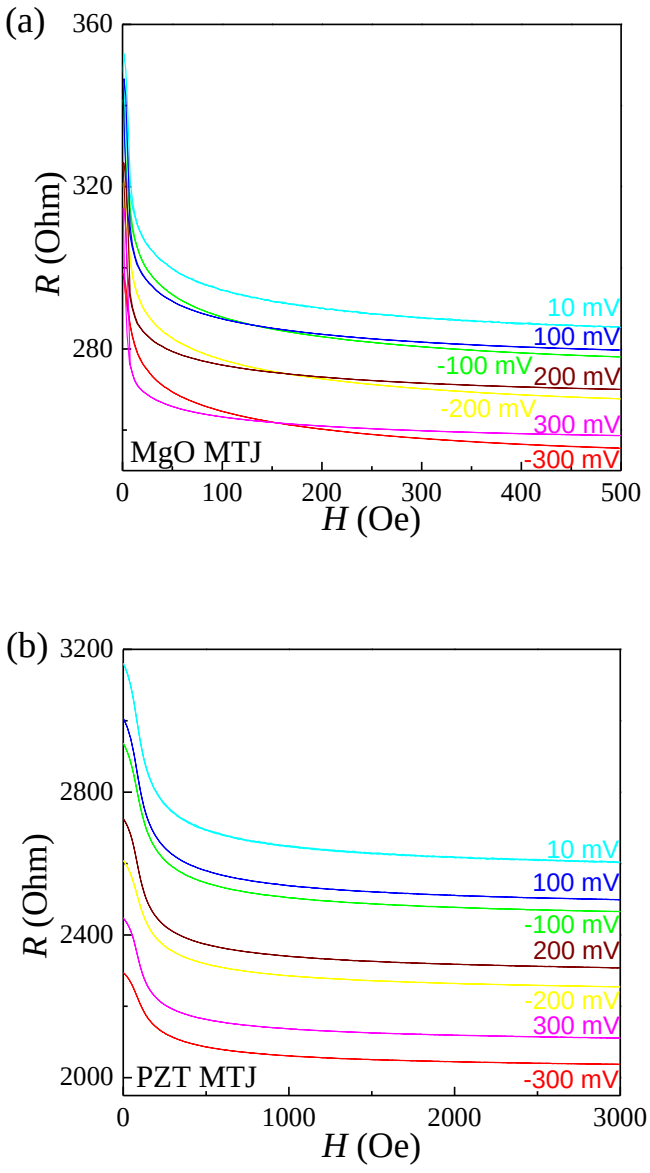

Figure 5-4. Resistance vs. in-plane magnetic field of varying applied voltages from -300 to 300 mV for a (a) MgO MTJ device and (b) PZT MTJ device.

As the free layer has a perpendicular magnetic easy-axis and the fixed layer is magnetically in-plane, at maximum in-plane magnetic field which is larger than the perpendicular anisotropy field of the free layer, the two ferromagnetic layers are both fully magnetically in-plane, resulting in the smallest MTJ resistance. When the external field decreases to zero, the fixed layer remains magnetically in-plane, but the free layer rotates from being magnetically in-plane to a perpendicular orientation, which increases the MTJ resistance.

The VCMA coefficient, ξ, (i.e. the slope of K_i versus E_{eff} plot) is calculated using Equations (2-11)–(2-13) and shown in Figure 5-5 for two representative MgO and PZT MTJ devices.

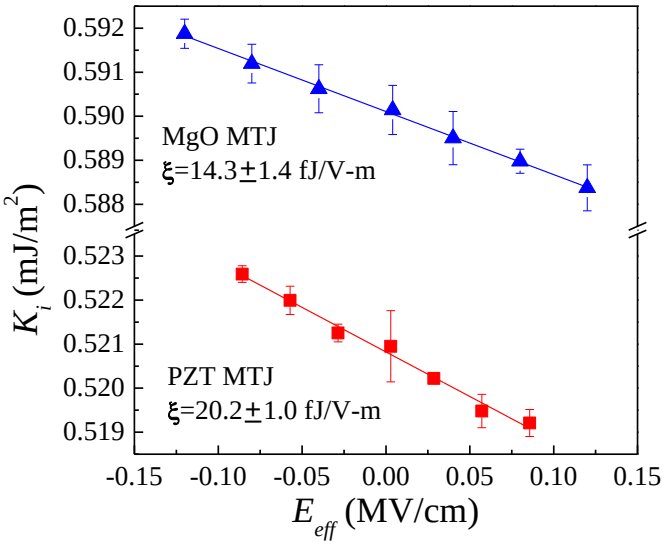

Figure 5-5. Interfacial perpendicular magnetic anisotropy (K_i) vs. applied electric field (E_{eff}) for a MgO and PZT MTJ device.

A total of six devices were measured for each MTJ stack and the average VCMA coefficients were $\xi_{average}$ = 14.3±2.7 fJ/V-m for MgO MTJs, whereas $\xi_{average}$ = 19.8±1.3 fJ/V-m for PZT MTJs. Compared with other works on Ta/CoFeB/MgO in literature with ξ = 10-60 fJ/V-m (Endo, Kanai et al. 2010; Liu, Pai et al. 2012; Zhu, Katine et al. 2012; Shiota, Bonell et al.

2013; Alzate, Amiri et al. 2014; Okada, Kanai et al. 2014), the VCMA values in our PZT and MgO MTJs are on the lower bounds, which might be caused by fabrication variations. Nevertheless, a comparison between the VCMA coefficients still indicates that the VCMA effect is enhanced by 38.5% with the MgO/PZT/MgO tunnel barrier.

From the physics point of view, this enhanced VCMA effect is generally considered to originate from the modification of charge accumulated at the CoFeB/MgO interface which affects the interfacial perpendicular magnetic anisotropy. As indicated from *ab initio* calculations, the K_i stems from the hybridization of Fe/Co *3d* orbitals and O *2p* orbitals at the CoFeB/MgO interface (He, Chen et al. 2011; Yang, Chshiev et al. 2011). The application of a positive electric field (i.e. top electrode of the MTJ at a higher electric potential) across the MgO barrier induces accumulation of electrons at the bottom CoFeB/MgO interface, which in turn decreases the value of K_i, which is consistent with the data shown in Figure 5-5 (Maruyama, Shiota et al. 2009; Niranjan, Duan et al. 2010). Hence, if the interface charge density σ_q increases for the same applied electric field E_{eff}, a larger VCMA coefficient ($\xi = \Delta K_i / \Delta E_{eff}$) can effectively be achieved.

Therefore, the change of charge density at the CoFeB/MgO interface under different MTJ bias voltages modifies the K_i values, thus the perpendicular anisotropy energy E_{perp}. The interface charge density σ_q can be expressed as $\sigma_q = \epsilon_0 K_{eff} V/d = \epsilon_0 K_{eff} E_{eff}$, where ϵ_0 is the permittivity of free space, and K_{eff} is the effective dielectric constant of the tunnel barrier. Thereby, for the same tunnel barrier thickness, the increase of the effective dielectric constant K_{eff} by incorporating PZT in the tunnel barrier lowers the bias voltage required to generate the interface charge to overcome the same energy barrier E_{perp}.

In addition, from the obtained VCMA ratio between the PZT MTJ and the MgO MTJ, the dielectric constant for the PZT ultra-thin film could be calculated. Using the serial capacitor assumption in the PZT MTJ, the effective dielectric constant was $K_{PZT-MTJ} = (d_{MgO} + d_{PZT})/(d_{MgO}/K_{MgO} + d_{PZT}/K_{PZT})$. For the MgO MTJ, the dielectric constant was assumed to be $K_{MgO-MTJ} = K_{MgO} = 10$ (Robertson 2004). As the change of interfacial PMA is proportional to the change of interface charge density, i.e. $\Delta K_i \propto \Delta\sigma_q$, we can deduce $\xi \propto \epsilon_{eff}$. Thus, based on the VCMA coefficients obtained for PZT and MgO MTJ, the dielectric constant of the PZT ultra-thin film was estimated to be 28.4, a plausible value taking into account the 1.5 nm PZT thickness, as well as existing literature values for an ultra-thin ALD PZT film (Bastani, Schmitz-Kempen et al. 2011; Zhang, Perng et al. 2011). This process of incorporating thin film into a MTJ tunnel barrier and calculating the relative change of the VCMA coefficient could be a potential future method to measure dielectric constants of ultra-thin films.

The VCMA coefficients were plotted against the interfacial perpendicular magnetic anisotropy energy, K_i, for all measured MgO and PZT MTJ devices, as shown in Figure 5-6. The VCMA coefficients were also plotted against TMR ratio for all measured MgO and PZT MTJ devices, as shown in Figure 5-7.

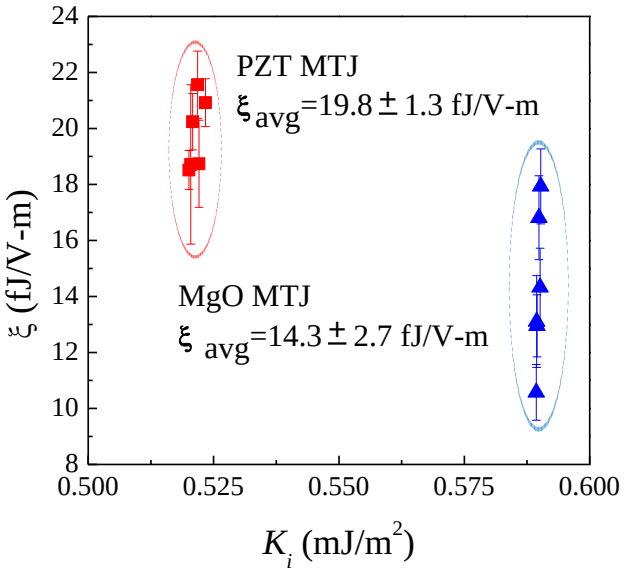

Figure 5-6. For all measured devices of MgO MTJ and PZT MTJ: VCMA coefficient ξ, vs. K_i. PZT MTJ shows $\xi_{average}$ = 19.8±1.3 fJ/V-m, whereas MgO MTJ shows $\xi_{average}$ = 14.3±2.7 fJ/V-m.

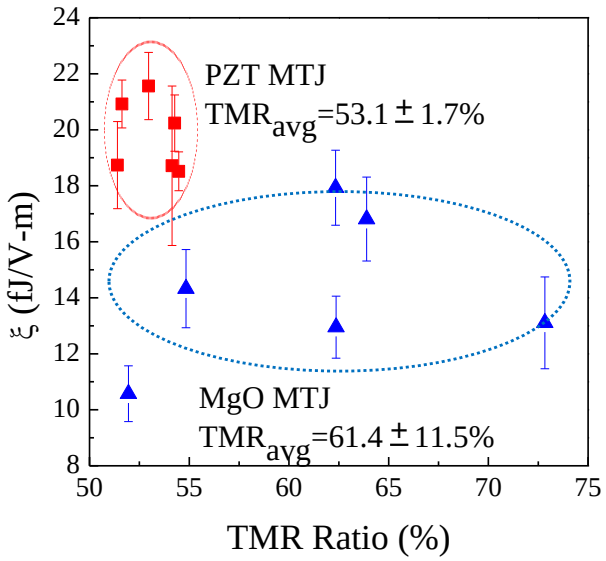

Figure 5-7. For all measured devices of MgO MTJ and PZT MTJ: VCMA coefficient ξ, vs. TMR ratio. PZT MTJ shows TMR ratio of 53.1±1.7%, whereas MgO MTJ shows TMR ratio of 61.4±11.5%.

Typical K_i values for the Ta/CoFeB/MgO structure is around 1 mJ/m^2 (Ikeda, Miura et al. 2010; Alzate, Amiri et al. 2014) and the observed smaller K_i values of 0.5-0.6 mJ/m^2 in this work might be improved with higher annealing temperatures (Skowroński, Nozaki et al. 2015). The PZT MTJs were observed to have a greater VCMA effect and a smaller TMR ratio compared to the MgO MTJs. The TMR is calculated using Equations (2-9)–(2-10) and the $TMR_{average}$ = 61.4±11.5% for MgO MTJs, while the $TMR_{average}$ = 53.1±1.7% for PZT MTJs.

Compared with other works on Ta/CoFeB/MgO in the literature with VCMA ranging from 10-60 fJ/V-m (Endo, Kanai et al. 2010; Kita, Abraham et al. 2012; Liu, Pai et al. 2012; Zhu, Katine et al. 2012; Shiota, Bonell et al. 2013; Alzate, Khalili Amiri et al. 2014; Okada, Kanai et al. 2014), the VCMA values in our PZT and MgO MTJs are on the lower bound, but the VCMA effect can be improved by optimizing a number of parameters including annealing conditions (Li, Yu et al. 2015), surface roughness (Ahmed and Victora 2015), and intrinsic strain (Ong, Kioussis et al. 2015) of the layers. Nevertheless, a 40% enhancement in the VCMA coefficient was achieved by using the MgO/PZT/MgO tunnel barrier while a relatively high TMR was still preserved.

In conclusion, by combining atomic layer deposition and magnetron sputtering techniques, an ultrathin PZT layer was successfully incorporated into the MgO tunnel barrier of a magnetic tunnel junction for the first time. The resulting magnetic tunnel junctions using high-ϵ tunnel barrier were shown to have both large tunneling magnetoresistance (>50%) and an enhanced VCMA effect (by 40%) at room temperature. This novel high-ϵ tunnel barrier MTJ is a potential candidate for future voltage-controlled, ultralow-power, high-density MRAM devices.

CHAPTER 6. SUMMARY

The synthesis of PZT thin films was demonstrated using thermal ALD. The processing conditions (i.e. rapidly thermal annealing temperatures) were determined to enable the deposition of PZT films with desired morphotropic phase boundary composition of Zr/Ti = 52/48, as confirmed by XPS. The films were characterized in respect to crystal structure via XRD and SEM, and piezoelectric properties via PFM. (100)-textured ALD PZT films were successfully obtained on Pt (111) substrates with the help of a 5-10 nm thick ALD $PbTiO_3$ seed layer. It was also shown that ALD PZT thin films could be successfully integrated into multiferroic memory devices and engineered to make multiferroic nanocomposites.

Additionally, scalability of ALD PZT thin films over large 6-inch platinized silicon wafers was realized. ALD PZT thin films were also deposited to coat La_2XMnO_6 (X = Ni or Co) nanoparticles to make core-shell multiferroic nanoparticles. ALD and CVD PZT films were deposited on silicon substrates to fabricate PZT MOS capacitor devices for C-V measurements in order to quantify the dielectric constants of the films.

In this work, the magnetoelectric coupling effect was studied in a complex architecture made of ALD PZT thin film coupled with templated mesoporous CFO matrix. Because the neck size has a radius of 6 nm, the ALD PZT thin films were deposited with thickness of 6 nm (mostly-filled CFO pores) and 3 nm (partially-filled CFO pores). The morphology, elemental analysis, and crystallinity were characterized by SEM, XPS, XRD, and TEM. The magnetoelectric coupling effect was studied by ex-situ electrically poling the PZT/CFO nanocomposite at 0–1.42 MV/m, and then measuring the change in magnetic moment via SQUID by sweeping in-plane and out-of-plane magnetic fields at ±20 kOe (2 Tesla). The in-plane magnetization showed no change due to substrate clamping of the PZT/CFO

nanocomposite. However, the out-of-plane magnetization exhibited a dependence on the applied electric field, suggesting a strain-mediated magnetoelectric effect between the PZT (piezoelectric) and CFO (magnetostrictive) layers. The magnetoelectric coupling coefficient was calculated to be 85.6 Oe-cm/mV. The 3-nm-thick PZT (partially-filled CFO pores) showed 5.1% greater change in the saturation magnetization than the 6-nm-thick PZT (mostly-filled CFO pores), suggesting that residual porosity allows mechanical flexibility to enhance magnetoelectric coupling. The impact of this work shows that combining ALD and wet chemistry techniques provides the capability of synthesizing nanocomposites with complex porous three-dimensional architecture that demonstrates the magnetoelectric effect; thereby allowing an additional parameter (i.e. porosity) to be explored in future nanocomposites. Further studies could include changing the size of the pore walls and determining the relationship between porosity and magnetoelectric coupling coefficient.

Additionally in this work, the TMR and VCMA effect were demonstrated for PZT MTJs with MgO (1.0 nm)/PZT (1.5 nm)/MgO (1.0 nm) tunnel barrier and compared with MgO MTJs with a 2.5 nm thick MgO tunnel barrier. The PZT film was deposited via atomic layer deposition with morphotropic phase boundary composition of Zr:Ti = 52:48. Elemental analysis was characterized by XPS and STEM. The TMR ratio and VCMA effect were measured by sweeping an in-plane magnetic field from 0-3000 Oe while varying applied voltage from -300 to +300 mV. The MgO MTJs were measured to have TMR ratio of 61.4$\pm$11.5% and $\xi_{average}$ = 14.3$\pm$2.7 fJ/V-m, whereas the PZT MTJs were measured to have TMR ratio of 53.1$\pm$1.7% and $\xi_{average}$ = 19.8$\pm$1.3 fJ/V-m. The VCMA coefficient of PZT MTJs was observed to be 38.5% larger than those of MgO MTJs. The dielectric constant of the PZT ultra-thin film was also determined to be 28.4 using a serial capacitor assumption for the MgO/PZT/MgO barrier. The

impact of this work is that it was the first demonstration of increased VCMA in a complete MTJ stack using a high dielectric constant material within the tunnel barrier and exhibiting sizeable TMR at room temperature, thereby showing that PZT MTJs are potential candidates for future voltage-controlled, ultralow-power, high-density MRAM devices. Further studies of PZT MTJs would be interesting, such as crystallizing the PZT ultra-thin film and investigating the effect of piezoelectric and ferroelectric behavior from the PZT layer on MTJ properties.

APPENDIX A. SCHEMATICS OF ALD PZT REACTOR

A.1. Isometric View of Low-vacuum ALD PZT Reactor

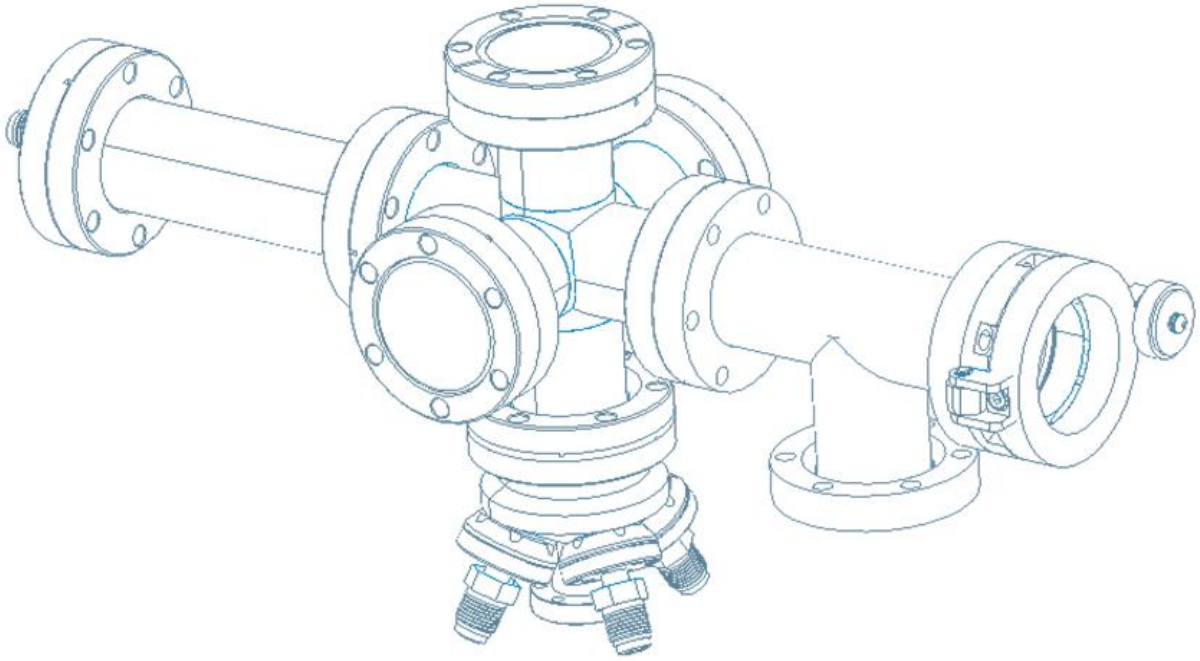

University of California, Los Angeles, Department of Chemical and Biomolecular Engineering							
Part	ALD PZT Reactor	Material	Stainless steel (316)				
Filename	ALD of small scale PZT reactor_130819	Scale	No	Unit	inch	Quantity	1
Designer	Diana Chien	Date	8/19/2013				
Revised by		Date					
Contractor		Date					
Comments	All parts were from MDC		Tolerance		+/- .0001		

APPENDIX B. STANDARD OPERATING PROCEDURES

B.1 ALD PZT Chamber Operating Procedure

B.1.1 Chemicals Used:

1. Lead bis (2,2,6,6-tetramethyl-3,5-heptanedionato) [$Pb(C_{11}H_{19}O_2)_2$, $Pb(TMHD)_2$]
2. Titanium diisopropoxidebis (2,2,6,6-tetramethyl-3,5-heptanedionato) [$Ti(O\cdot i\text{-}C_3H_7)_2(C_{11}H_{19}O_2)_2$, $Ti(O\cdot i\text{-}Pr)_2(TMHD)_2$]
3. Zirconium tetrakis(2,2,6,6-tetramethyl-3,5-heptanedionato) [$Zr(C_{11}H_{19}O_2)_4$, $Zr(TMHD)_4$]
4. Deionized Water

B.1.2 Emergency Shutdown:

1. If depositing, stop the LabView program.

2. Shut down all the electronics: Temperature Controllers (top and bottom), Water Heating Transformer, Mass Flow Controller control panel, and Substrate Heating Transformer.

3. Close all the precursor/reactant valves: Pb (V12), Zr (V8), Ti (V10), N_2 (V9), and H_2O (V5)

4. Manually close the roughing valve to isolate the chamber.

5. Proceed to emergency exit locations.

B.1.3 Operating Procedure:

1. *Initial check:* Check TC pressure gauge reads base pressure, make sure all the valves are closed, and both temperature controllers (top and bottom) are reading room temperature on all channels.

2. *Venting the chamber:* Close the roughing valve to isolate the chamber, unlock the door so it is able to open when vented, open the N_2 MFC (channel 4) to 10-15%, open the N_2 line (V11 on black box and V6 on Li chamber box), open the N_2 valve (V9) for 1-5 minutes, close the N_2 valve (V9), close the N_2 line (V11 on black box and V6 on Li chamber box), close the N_2 MFC (channel 4) to 0%, and manually open the vent valve until door opens. Once vented, manually close the vent valve.

3. *Sample loading:* Make sure chamber is vented. Take off the conflat flange with TC/power feedthrough and load the sample onto the substrate heater. Use the multimeter to check the resistance. Readings should be:
   Across the thermocouples: 1-2 Ohms
   Across the power leads (to substrate heater): 0.2-0.4 Ohms
   From thermocouple to power leads: 0.5-2 Ohms

From thermocouple to conflat flange: OL
From power leads to conflat flange: OL

If resistance readings are not correct, then check all the connections. If resistance readings are correct, then attach the conflat flange onto the chamber. Check the resistance again after tightening the conflat flange. Also, use a flashlight and check that the sample is being held in the substrate heater.

4. *Pumping the chamber:* Open the roughing valve, and pump the chamber until TC pressure gauge reads base pressure of 120 mTorr.

5. *Nitrogen Purge:* (*) Set channel 4 of MFC controller to 20-25%. Open the N2 line (V11 on black box and V6 on Li chamber box) for 10 seconds then close valves. Open the N2 valve (V9) until base pressure is reached. Repeat the procedure (*) at least 2 more times before depositing.

6. *Heating:*
   a. Check all the temperature settings on the temperature controllers for the channels you are using.

	Setpoint Temperature	*Channel (temperature controller)*
Pb valve	150 ^{o}C	1 (top temperature controller)
Pb house	115 ^{o}C	2 (top temperature controller)
Zr valve	190 ^{o}C	3 (bottom temperature controller)
Zr house	180 ^{o}C	4 (bottom temperature controller)
Ti valve	110 ^{o}C	5 (bottom temperature controller)
Ti house	90 ^{o}C	6 (bottom temperature controller)
Chamber	100 ^{o}C	7 (bottom temperature controller)

   b. Chamber: Heat the chamber by turning on channel 7 of bottom temperature controller. The chamber needs to be heated for 1 hour before heating the precursors, and heated for 2 hours before deposition. At this time, turn on the Substrate heater transformer to 6%.
   c. Precursors: Heat the Pb, Ti, and Zr housing and valves by turning on appropriate channels on the appropriate temperature controllers (see Table). The precursors need to be heated for at least 1 hour before deposition. Usually after 1 hour of heating the chamber, I turn on the precursors. When precursors start heating, turn the Substrate heater transformer to 9-10% until the substrate heater reads ~312^{o}C (which corresponds to the substrate ~195^{o}C, the deposition temperature).
   d. Water: Heat the water by connecting the heating cord to the power and turning the gray transformer to 25%. Water needs to heat for 10 minutes, then open the water tube valve to setting = 30 to flow water vapor into the water gas line, and wait for 5 minutes. Start the water heating after the precursors have been heating for 45 minutes.
   e. Record the base pressure after heating. Deposition can now begin.

7. *Manual Deposition:* ***The procedures are only for one cycle.***
   a. PbO Deposition
      i. Open Pb valve (V12) for 15 seconds.

ii. Close the valve and wait 30 seconds to pump down the chamber to the base pressure.
iii. Open Water valve (V5) for 15 seconds.
iv. Close the valve and wait 45 seconds to pump down the chamber to the base pressure.
v. *(if needed) Perform (*) of Step 5, Nitrogen Purge Step (Perform if the chamber doesn't go back to base pressure.*

b. ZrO_2 Deposition
i. Open Zr valve (V8) for 15 seconds.
ii. Close the valve and wait 30 seconds to pump down the chamber to the base pressure.
iii. Open Water valve (V5) for 15 seconds.
iv. Close the valve and wait 45 seconds to pump down the chamber to the base pressure.
v. *(if needed) Perform (*) of Step 5, Nitrogen Purge Step (Perform if the chamber doesn't go back to base pressure.*

c. TiO_2 Deposition
i. Open Ti valve (V10) for 15 seconds.
ii. Close the valve and wait 30 seconds to pump down the chamber to the base pressure.
iii. Open Water valve (V5) for 15 seconds.
iv. Close the valve and wait 45 seconds to pump down the chamber to the base pressure.
v. *(if needed) Perform (*) of Step 5, Nitrogen Purge Step (Perform if the chamber doesn't go back to base pressure.*

d. Record the base pressure after deposition is done.

8. *Automation Deposition:*
a. Check that all valves are closed and temperatures on the controller are reading correctly for all channels.
b. Choose the desired LabView deposition program.
c. Input the desired # of global cycles, PbO, ZrO_2, and TiO_2 cycle.
d. Record the base pressure before deposition.
e. Start the LabView program.
f. After deposition is done, record the base pressure.

9. *Finishing the deposition:* Turn off the heater for substrate heater, chamber, water, precursor valves and precursor housings. Wait for the chamber to cool down to at least 60ºC or lower. (It takes about ~2 hours roughly.)

10. *Sample unloading:* Perform (*) of Step 5, Nitrogen Purge Step, for at least 3 times, Perform Steps 1 and 2, and then take off the conflat flange with TC/power feedthrough from the chamber to unload the sample.

B.2 RHEED Operating Procedure

B.2.1 Emergency Shutdown Procedure

1. Dial Voltage and Current settings to zero.

2. Turn off the RHEED Gun Power Supply (it is normally off) by pressing the Power to Zero.

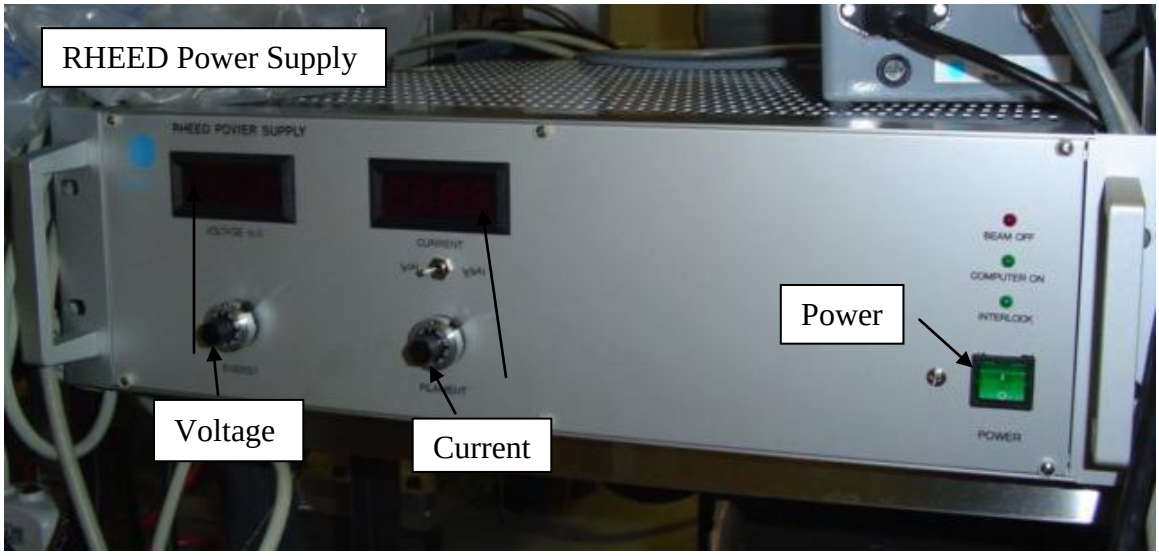

B.2.2 Operating Procedure

To operate the RHEED system, you must be trained on basic operation of the ALD chamber.

It is advised to set up the RHEED prior to deposition to obtain an initial pattern and observe the changes in real-time during deposition. For RHEED analysis, the crystallographic direction perpendicular to the edge of the sample facing the RHEED gun should be kept consistent for all samples.

The main reactor chamber must be being pumped by its turbo pump.

1. During operation, the RHEED electron gun must be differentially pumped with its own turbo pump to avoid damage at high chamber pressures. Set the Ion Gauge Controller to read "IG2" which is connected to the ion gauge between the RHEED turbo pump and the Gun. (See Figure below) Check that the pressure reads below $5x10^{-6}$ Torr (setpoint).

   A pressure interlock does not allow the Electron Gun Power Supply to turn on if the gun pressure is above the setpoint – see Appendix A for the interlock setup. Therefore, **during operation of the RHEED gun, IG2 must be on** in order to monitor the pressure of the gun. Consequently, the pressure in the chamber (IG1) cannot also be monitored because the Ion Gauge Controller can only operate one gauge at a time. The IG2 need to be on ~30 min to read an accurate pressure.

2. **Make sure** the small manual Gate Valve between the Turbo and the Gun is open. (Otherwise the gun does not actually get pumped!)

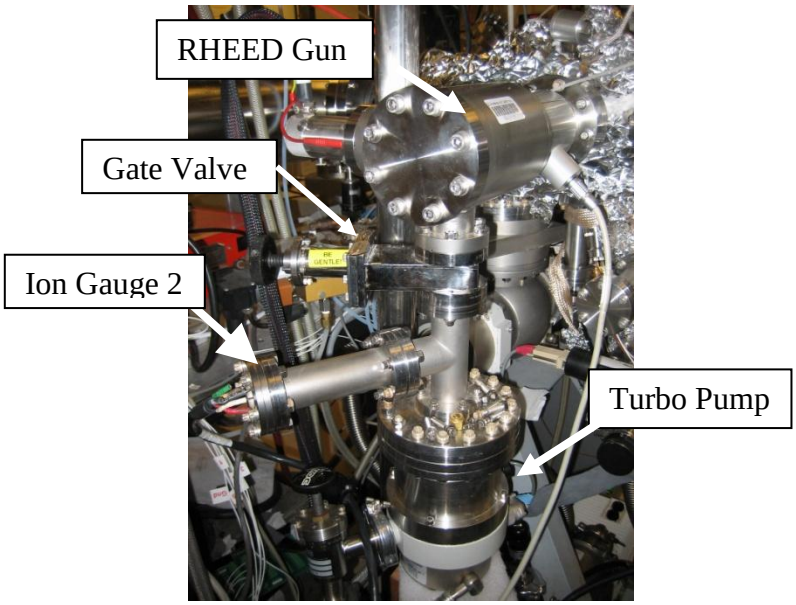

3. Turn on the power on the RHEED Power Supply
    a. The Interlock light should be illuminated (ok)
    b. The Computer On light should be dim
    c. The Beam Off light should be dim
    (If lit, flip the Beam Blanking toggle switch on the Remote Control Box.)
4. Slowly ramp up the Current to 1 A. Wait for 30 seconds, and slowly ramp up to 1.2 A and finally 1.4 A. Above 1 A, the ramp-up should be ~0.1A per 5 seconds. The maximum operating current should not exceed 1.45 A.
5. Slowly ramp up the Voltage to the desired setting (10 keV or 15 keV)

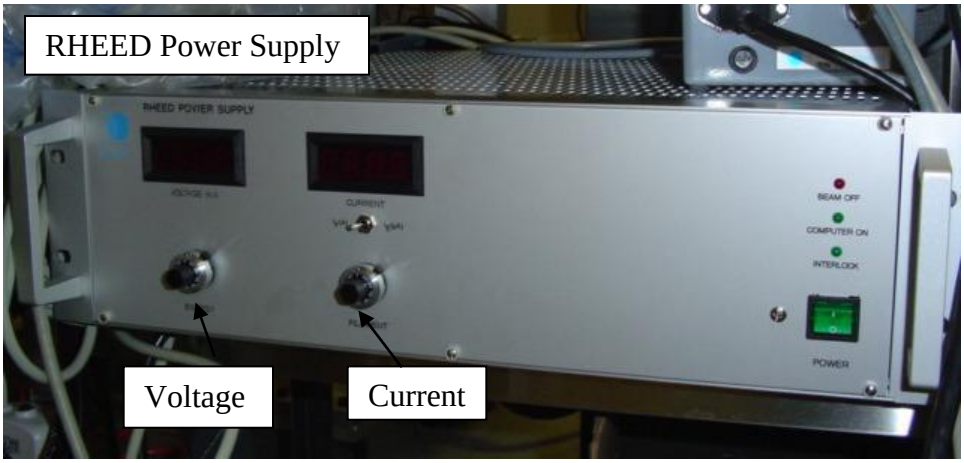

6. Using the Remote Control box, adjust the X and Y-deflection knobs to roughly align the beam with the sample surface. The midscale position for the X and Y-deflection is 5. If X-deflection is increased, beam moves to the left of the screen as viewed from outside the chamber. If decreased, beam moves to the right. Similarly, if Y-deflection is increased, beam moves up on the screen. If decreased, beam moves down. For repeatability, take note of the number of the setting.

7. Remove the top of the CCD camera box and view the direct beam pattern on the fluorescent screen.

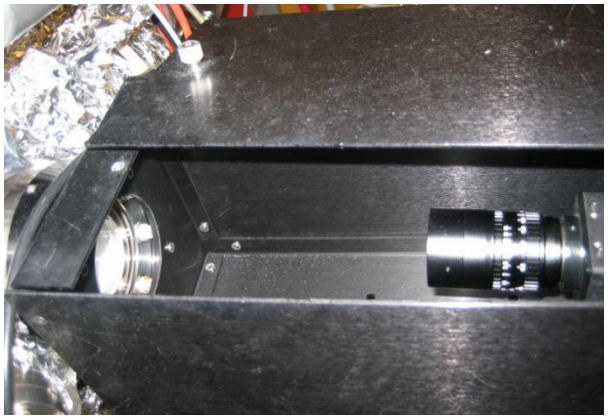

8. Adjust the Grid (intensity) and Focus knobs simultaneously to focus the direct beam as small and clearly as possible on the screen. The focus affects the intensity, so the knobs should be adjusted simultaneously.

9. Adjust the X-deflection and Rocking knobs simultaneously to obtain the necessary incident angle to observe a diffraction pattern.

   Increasing the X-deflection brings the beam out from the sample and decreasing the Rocking brings it back toward the sample. The midscale position for the Rocking option is 5.

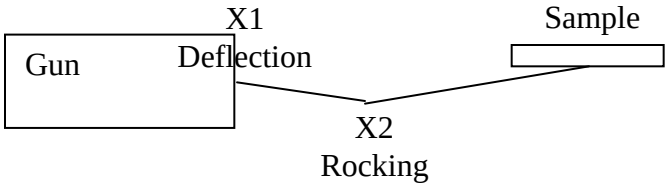

10. Adjust the rotation of the sample slightly using the manipulator to observe different diffracted planes.
11. Record the settings in the RHEED logbook.
12. Using the KSA software, a live video stream of the diffraction pattern can be obtained. To adjust the image contrast, select Properties and modify the Exposure Time or the Number of Frames. To save an individual image, select Acquire Single Image. The images can then be exported as BMP, GIF, or TIF files.

B.2.3 Factory Settings

Energy (keV)	Current (A)	Focus	Grid	Flange Target Distance (mm)
10 keV	1.4	3.84	1.92	505
15 keV	1.4	5.12	2.42	505

Flange Target Distance = distance between gun mounting flange and phosphor screen.

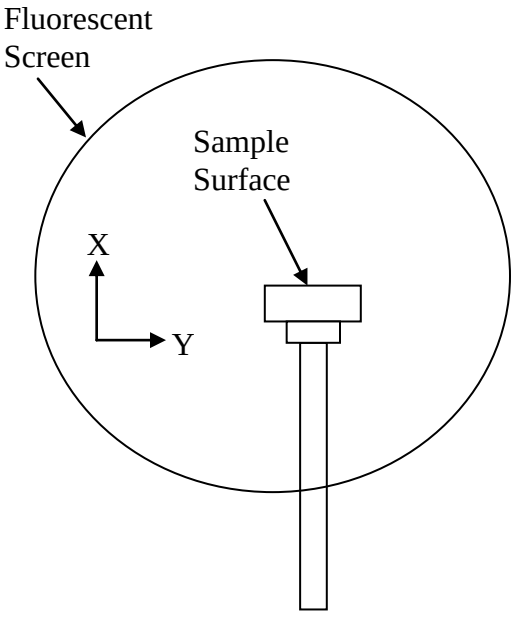

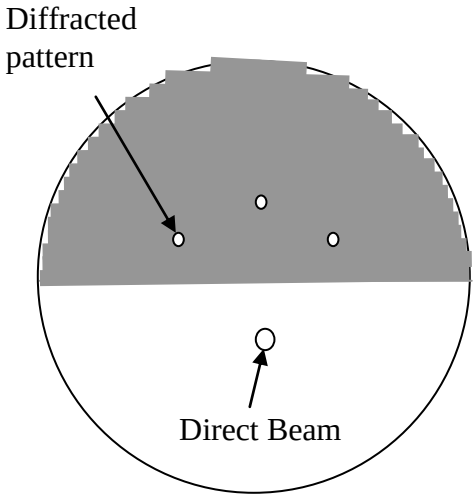

B.2.4 Troubleshooting

If the Fluorescent Screen becomes contaminated:

We used Phosphor Solutions as the vendor to clean and recoat the phosphor screen (Staib #RS64).
There were some problems with this company, so we may not want to use them again. They were very difficult to get hold of by phone and they did not receive our faxes for quite some time. The quote was for $250. One-week delivery.

Mark Heller
Phosphor Solutions
20162 HWY 18 G-206
Apple Valley, CA 92307
(760) 553-9698
FAX (760)242-7363

If the diffraction image on the screen becomes distorted:

Example: the points become stretched out into lines. There may be an AC voltage source nearby causing interference with the RHEED gun. The easiest solution is to relocated the source at least two feet away from the gun.

B.3 PFM Operating Procedure

B.3.1 Operating Procedure

1. Secure sample to microscope stage. If the substrate is insulating, screw on Ta clip to create an electrical connection between an area of exposed platinum and the sample stage (clean the Ta with IPA before use). Typical resistance values are 1 Ω through the stage and 1-10 Ω between the sample surface and stage.

2. Load a conductive tip (SCM-PIT) into the probe holder and attach the probe holder to its mount, locking it in place by screwing in the pin on the right side of the microscope.

3. Open the software and load the *Optimized Vertical Domains* experiment under *Electrical & Magnetic => Piezoresponse*.

4. Adjust the top pins until the red laser dot is on the back of the cantilever.

5. Adjust the side pins until the red laser dot is in the center of the detector.

6. Focus on the back of the cantilever and double click on the location of the tip (where it would be on the opposite side).

7. Navigate on top of the sample and close the microscope door.

8. Select *Sample (default)* and focus on the sample surface. It is often easiest to focus on the edge of the sample first.

9. Select *Tip Reflection* and focus on the back of the tip.

10. Set the *Scan Size* and *Applied Voltage* to 0 and ensure that the *Deflection Setpoint* is larger than the *Vertical Deflection* (0.1-0.25 V).

11. Engage the surface. Slowly increase the *Deflection Setpoint* in order to engage the surface with minimum force.

12. To ensure that contact has been made with the surface, perform a force curve measurement.
    a. Click on the *Ramp* node under the *Real Time* node.
    b. Set *Ramp Output* to "Z". Set *Feedback Type* to "Pixel".
    c. Sweep through a range of Z values at constant applied voltage to obtain a force curve for the cantilever. Trigger (in relative mode) to stop after measuring a 1 V deflection. The curve should resemble that shown below, where the dip is indicative of short-range adhesive forces between the tip and sample surface.
    d. The linear area of the curve sectioned off by the red dotted lines can also be used to the measure the deflection sensitivity of the cantilever.

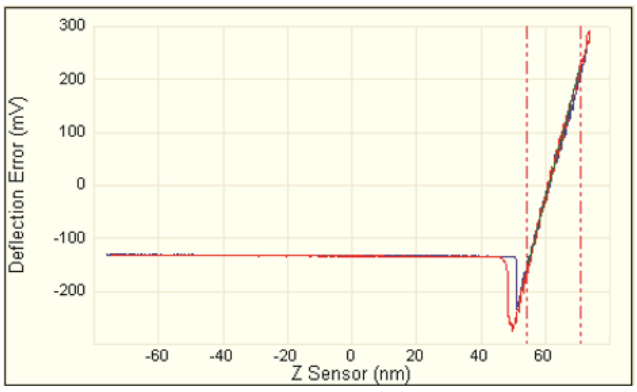

13. To determine the ferroelectric nature of the sample, obtain a P-E loop by ramping the voltage applied to the tip.
    a. Click on the *Ramp* node under the *Real Time* node
    b. Set *Ramp Output* to "Tip Bias". Set *Feedback Type* to "Pixel".
    c. Sweep through a range of applied voltages (-12 V to 12 V) to obtain a PE loop for the sample. The hysteresis is easily observed by plotting the amplitude and phase of the piezoresponse signal against the applied voltage. If the sample is ferroelectric, the results should look similar to those shown below.

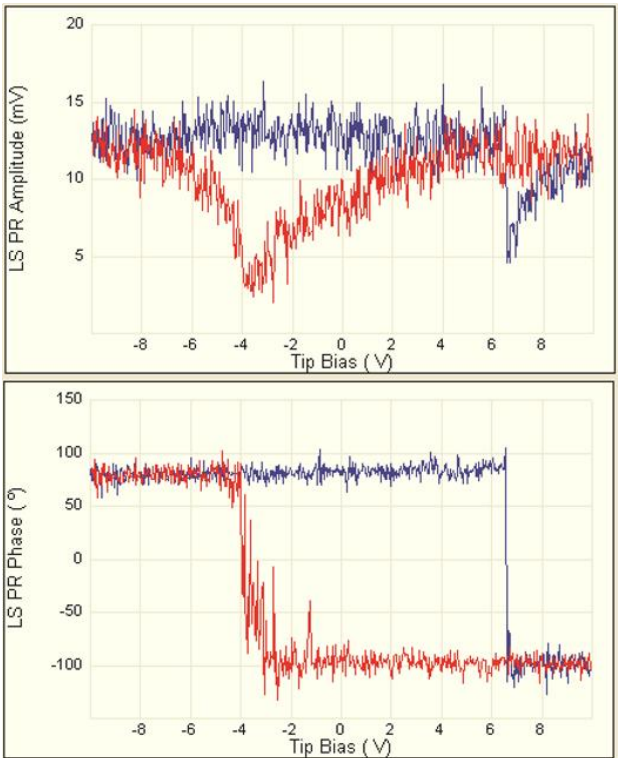

14. After performing all other desired measurements, withdraw the tip, raise the scanner head, and return the stage to the loading position.

15. Shut down the software, remove the sample and tip from the microscope, and close the door.

B.4 Conductive AFM Operating Procedure

B.4.1 Operating Procedure

1. Secure sample to microscope stage. If the substrate is insulating, screw on Ta clip to create an electrical connection between an area of exposed platinum and the sample stage (clean the Ta with IPA before use). Typical resistance values are 1 Ω through the stage and 1-10 Ω between the sample surface and stage.

2. Load a conductive tip (SCM-PIT) into the probe holder and attach the probe holder to its mount, locking it in place by screwing in the pin on the right side of the microscope.

3. Attach the xTUNA module to the scanner head using the two long screws. First remove the U-shaped wire from xTUNA module. Then, using insulated tweezers, plug one end of a wire into the hole labeled "APPMOD" and the other end into the xTUNA module (the hole previously filled with the U-shaped wire, but NOT the "test bias" hole).

4. Open the software and load the *TUNA2 Module* experiment under *Electrical & Magnetic => Application Mod*.

5. Adjust the top pins until the red laser dot is on the back of the cantilever.

6. Adjust the side pins until the red laser dot is in the center of the detector.

7. Focus on the back of the cantilever and double click on the location of the tip (where it would be on the opposite side).

8. Navigate on top of the sample and close the microscope door (no laser tuning).

9. Select *Sample (default)* and focus on the sample surface. It is often easiest to focus on the edge of the sample first.

10. Set the *Scan Size* and *Applied Voltage* to 0 and ensure that the *Deflection Setpoint* is larger than the *Vertical Deflection* (0.1-0.25 V). Set the *Sensitivity* to 1 nA/V.

11. Engage the surface. Slowly increase the *Deflection Setpoint* in order to engage the surface with minimum force. This value may be increased later to improve Ohmic contact.

12. A small offset current (a few mA) is measured. To ensure that this is simply background, turn off the line, switch Channel 3 to "None", and lift off the tip from the sample. If the same current continues to be measured, then it is indeed just background.

13. To ensure that contact has been made with the surface, perform a force curve measurement.
    a. Click on the *Ramp* node under the *Real Time* node.
    b. Set *Ramp Output* to "Z". Set *Feedback Type* to "Pixel".

c. Sweep through a range of Z values at constant applied voltage to obtain a force curve for the cantilever. Trigger (in relative mode) to stop after measuring a 1 V deflection. The curve should resemble that shown below, where the dip is indicative of short-range adhesive forces between the tip and sample surface.
d. The linear area of the curve sectioned off by the red dotted lines can also be used to the measure the deflection sensitivity of the cantilever.

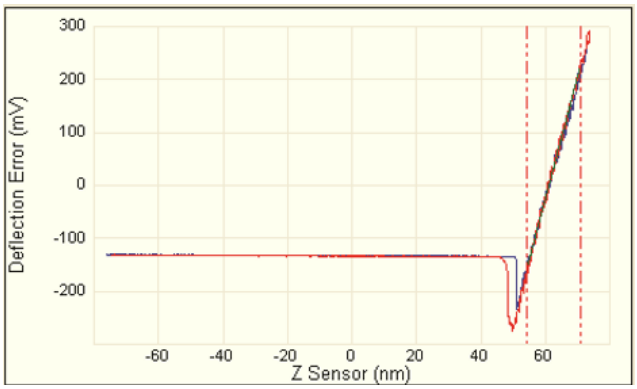

14. To find pinholes in the film, increase the samples/line to at least 512 (to increase resolution) and decrease the total number of lines. Any spots can be individually scanned (can ramp voltage at constant force) by using the *Mark, Ramp, and Capture* feature under *Point and Shoot*.

15. After performing all other desired measurements, withdraw the tip, raise the scanner head, and return the stage to the loading position.

16. Shut down the software, remove the sample and tip from the microscope (take care to hold the xTUNA module while removing from the scanner head and to replace the U-shaped wire for storage), and close the door.

B.5 C-V Measurement Operating Procedure

B.5.1 Emergency Shutdown Procedure

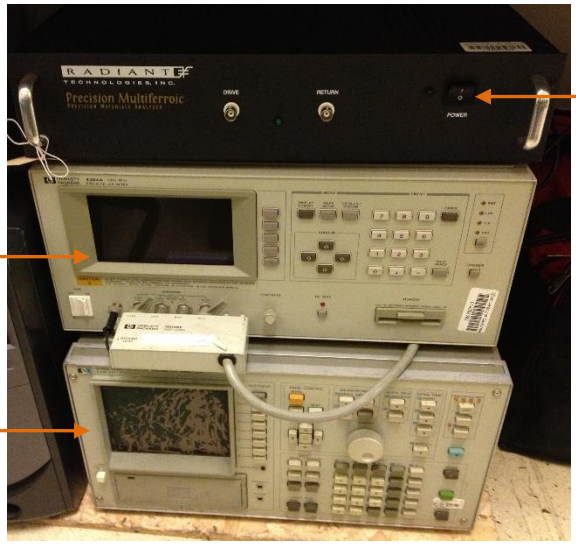

1. Turn off Precision Multiferroic Test System.
2. Turn off HP 4284 A LCR meter.
3. Turn off HP 4145 Semiconductor Parameter Analyzer.
4. Turn off microscope light bulb.

B.5.2 Operating Procedure

Two types of probe tips are available for the micromanipulator: model 7A and model 7B. Model 7A is a fine probe tip with a 0.005” diameter. Model 7B is a heavy duty probe tip with a 0.020” diameter. Choice of tip depends on the size and type of metal electrode used to perform the electrical measurements.

PE Measurement...

1. Turn on Precision Multiferroic Test System.
2. Turn on microscope light bulb.
3. Launch Vision software.
4. Click ok on popup window.
5. Disconnect the probe tip from the sample.

6. Disconnect a cable from “DRIVE” for offset calibration.

7. Click “yes” to calibrate the offset.

8. Wait for 30 seconds to measure ramp offset.

9. Go to *Outlook => Hysteresis*.

10. Edit parameters (voltage, sample area, thickness, and hysteresis period) then press “OK”.

11. Check the test parameters from *Parameter Response* tab.

CV Measurement...

1. Turn on HP 4284 A LCR meter.

2. Turn on microscope light bulb.

3. Launch ICS (Interactive Characterization Software).

4. Go to *Instruments => Select Instrument*.

5. Look for HP 4284, click “Connect” (HP 4145 would be connected now if I-measurements were desired), then click “OK”.

6. Go to *Measure => Edit Setup*, click “New”, provide a name (e.g. C-V).

7. Under *Device*, click “Cap” then “OK”.

8. Click “Source Units” and highlight HP 4284. Then click “Source Units", highlight *CMH*, and click on one end of the capacitor to make the connection. Do the same for *CML* to the other end of the capacitor and click “Done” in the source unit window when finished.

9. Click on the CMH side of the capacitor. A window pops up with the set-up parameters.

    a. Select “C“ in display 1, select “Sweep” for bias mode, and specify the start and stop voltage for CMH relative to CML (typically -2 to 2 V, with 100 points).
    b. In the integration option, select “Long” integration.
    c. Note or change the frequency if desired, then click “OK” in the setup window then “Done” in the setup editor.

10. Click on the graph button and input min and max bias values. Select “C” for y axis.

11. Connect one probe to the top electrode using the microscope (see following section on calibration of HP 4284 A LCR Meter) and the other probe to the chuck, which connects to the substrate via the backside contact.

12. Connect the banana plugs to the appropriate receptacles, labeled "CMH" and "CML".

13. Click "Measure", select the name of the measurement (C-V) and click "Single" to take a single measurement.

IV Measurement...

1. Follow a procedure similar to a CV measurement, except use the HP 4145 A Semiconductor Parameter Analyzer and set up the ICS for I-V measurements. Similarly construct a capacitor, but select HP 4145 as the source unit.

Transistor Measurements...

1. Follow a procedure similar to a I-V measurement. Specify the testing parameter by specifying the sweeping voltages.

Exporting Data...

1. Click "Export" and use the test format file type (Vision software).

2. Go to *File => Export Data* and use the ASCII file type (ICS software).

B.5.3 Calibration of HP 4284 A LCR Meter

1. Click "MEAS SETUP" and select "Correction" on the LCR meter. This loads the correction page.

2. Open Correction...
   (open correction cancels errors due to the stray admittance in parallel with the device)
   a. Move cursor to the *Open* field. "ON", "OFF", and "MEAS OPEN" options comes on display.
   b. Create an open circuit by lifting the two probes out of contact with the chuck.
   c. Press "MEAS OPEN".

3. Short Correction...
   (short correction corrects for residual impedance in serial with the device)
   a. Move cursor to the *Short* field. "ON", "OFF", and "MEAS SHORT" options comes on display.
   b. Create a short circuit by making direct contact between the two probes.
   c. Press "MEAS SHORT".

B.6 e_{31} Measurement Operating Procedure

B.6.1 Operating Procedure

The transverse piezoelectric coefficient, $e_{31,f}$, is typically determined by measuring the generated piezoelectric charge perpendicular to the sample (direction 3) as a function of in-plane strain (direction 1). Based on literature, it has been directly measured with one of the following three methods: *(1)* bending a cantilever (Cattan, Haccart et al. 1999), *(2)* laser interferometers, and *(3)* wafer flexure technique (Shepard, Moses et al. 1998).

In the cantilever method, the PZT thin film sample is first processed into small beams (length of 40 mm, width of 10 mm, and thickness of 0.38 mm) and then clamped at one end to the stage, as shown schematically in Figure B.6.1 (Cattan, Haccart et al. 1999).

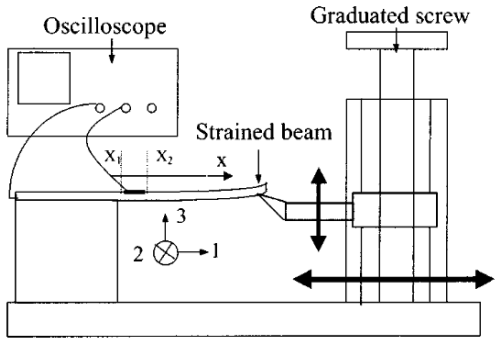

Figure B.6.1. Cantilever method experimental setup (Cattan, Haccart et al. 1999).

PZT films were sputtered over the entire cantilever surface and a platinum top electrode (area of 1 mm^2) was deposited on the top of it. A beam was used to flex the unclamped end of the cantilever perpendicular to the film plane, thus applying an in-plane strain to the film. By suddenly releasing the strained beam, electric charges were generated and the $e_{31,f}$ was directly measured (Cattan, Haccart et al. 1999).

A contact at aixACCT is available to make this type of measurement on PZT films using bars that are 3 mm wide and 25 mm long to be clamped into the measurement apparatus. However, this technique is difficult to implement on thin film materials. The small electrodes (50 μm^2 in area) require the use of very fine probes, which may damage the film significantly. A popular alternative technique is the usage of laser interferometers in either single- or double-beam set-ups. The monochromatic laser light results in a change of its optical path as a response to a piezoelectrically induced strain. However, this technique is limited by displacement unrelated to piezoelectricity (such as sample flexure and drift) and ambient noise (Shepard, Moses et al. 1998).

In comparison to other methods of characterizing the transverse piezoelectric coefficient, the wafer flexure technique is preferable because it does not require much sample preparation for measurement. The $e_{31,f}$ characterization of ALD PZT thin films is performed as a collaboration with Professor Susan Trolier-McKinstry, in the Materials Research Laboratory at The Pennsylvania State University, who's group designed the wafer flexure technique (Shepard, Moses et al. 1998). An advantage to the wafer flexure technique is that a wide variety of

substrate and sample geometry can be characterized. Small samples of $\leq$ 1 cm^2 can be characterized by bonding the small substrate to a Si wafer and relying on the strain transferring through the bonding layer (Maria, Shepard et al. 2005). The ALD PZT thin films deposited on platinized silicon substrate is mounted on a 3-inch Si carrier wafer using Loctite SuperGlue. A commercial strain gauge (~1.5 mm x 4.5 mm) is then mounted directly on top of the sample (Wilke, Moses et al. 2012). The strain gauge consists of a metallic foil pattern and when the foil is deformed, the electrical resistance changes in proportion to the induced strain. The Si carrier wafer is then clamped in a uniform pressure rig, as shown in Figure B.6.2.

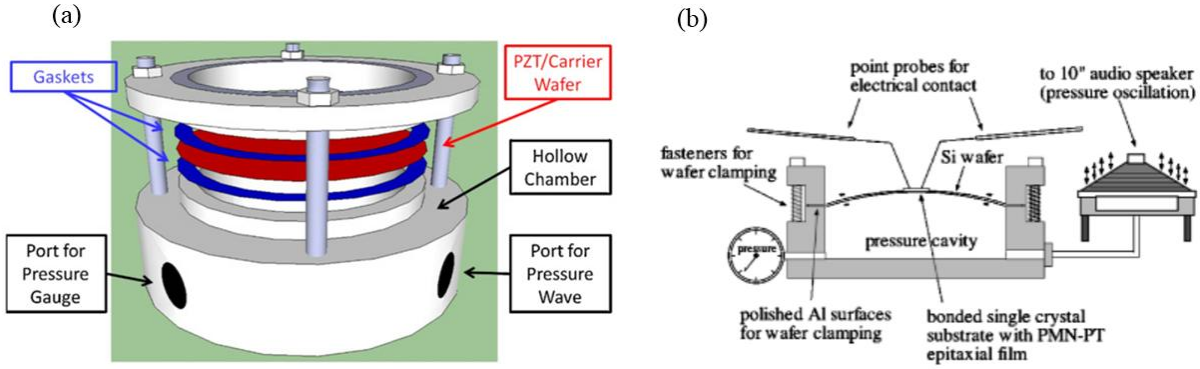

Figure B.6.2. Wafer flexure method experimental setup: (a) 3D rendering of mounting of PZT/carrier wafer for measurement (Wilke, Moses et al. 2012) and (b) modification to measure small size samples of $\leq$ 1 cm^2 (Maria, Shepard et al. 2005).

A high power audio speaker produces an oscillating air pressure inside the housing which flexes the wafer to apply strain to the sample. The pressure transducer is a Wheatstone bridge configuration where the output voltage across the bridge is proportional to the change in pressure in the chamber. As the film is displaced as a function of mechanical stress, the generated charge from the piezoelectric film is collected by an amplifier integrator. A voltage that is proportional to the amount of charge collected is read as the output signal, which is used to obtain the transverse piezoelectric coefficient value of $e_{31,f}$ (Shepard, Moses et al. 1998; Wilke, Moses et al. 2012).

B.7 MOKE Measurement Operating Procedure

B.7.1 Operating Procedure

1. Turn on laser.

2. Turn on amplifier.

3. Mount sample (this step takes the longest).
    a. Rotation holder is the most common option. Control angle from the back.

4. Use nickel reference for calibration.

5. Left polarizer should be at 45˚ (diamond shape).

6. Phase/intensity detector should be slightly off-perpendicular (when viewed from above).

7. Adjust right polarizer so that laser reflection is slightly off-center (reflection onto magnet is good). Ensure that the polarization angle is slightly off the vertical square.

8. Adjust settings on phase box.
    a. Set time constant to 30 ms (or larger for longer field sweep times).
    b. Set sensitivity so that red bar is less than half (to avoid data clipping). If intensity value oscillates, check setup. The ideal intensity is between 1 and 2 mV.
    c. Zero out phase using "Phase" button before each measurement.
    d. Reserve should be set to "High Reserve", but other options may work.
    e. Use 1st harmonic for in-plane measurements and 2nd harmonic for out-of-plane measurements (or use other one if the signal is stronger).

9. PEM-100 controller should always be at 630 nm and 50.073 kHz!

10. Calibrate magnetic field with the gaussmeter.
    a. Set electromagnet power supply to 5 A, read gaussmeter (e.g. 1043 Oe)
    b. Calibrate using your figure's maximum applied field for publication quality.

11. Run MATLAB code at the computer.
    a. Ensure that all necessary m-files are in the same directory.
    b. *clear all; clc;*
    c. *runmoke("NAME", startLoop, numLoops, -maxCurrent, maxCurrent, currentStep)*
    d. In *wplotfitMOKE* use calibrated field (e.g. maxgauss = 1043/5) and change name.
    e. If canceling a run prematurely, switch electromagnet power supply off and back on, and remember to turn knob to 0 A.

12. Remove nickel reference and use your own sample.

B.8 Ex-Situ Electrical Poling Operating Procedure

B.8.1 Operating Procedure

1. Place “ELECTRICAL POLING IN PROGRESS” flag across the entrance to the room.

2. Attach clips to power source. Each line likely requires two clips to be attached end to end in order to reach the sample. Ensure that these lines are electrically separated from one another by placing a wooden block between the lines (at the point where the two sets of clips are attached end to end).

3. Place the sample on the bottom metal cylinder.

4. Lay a single layer of plastic wrap (LDPE) on top of the sample, making sure that the area directly above the sample is not stretched, torn, or wrinkled.

5. Slowly screw in the top metal cylinder until it makes contact with the plastic wrap. Do not overtighten.

6. Turn on the power source. Make sure that the clips are not electrically connected to the sample, as powering on can be accompanied by a large voltage spike.

7. Attach the clips to the poling apparatus (labeled with tape).

8. Slowly ramp the voltage up to the desired level while observing the sample to ensure that there is no arcing (which would indicate that the sample has shorted).

9. Let the sample sit under the electric field for 10 minutes.

10. Slowly ramp the voltage back down to 0 and disconnect the clips from the poling apparatus.

11. Turn off the power supply.

12. Disassemble the poling apparatus by unscrewing the top metal cylinder and removing the sample along with the plastic wrap. Detach the clips from the power source and remove the “ELECTRICAL POLING IN PROGRESS” flag from the entrance.

APPENDIX C. LIST OF EQUIPMENT USED

Vendor	Catalog #	Description
Momentive Performance Materials	HTR-1001	GE advanced ceramics 25 mm boraelectric heater, resistance 10 ohms (stage), accessories
Omega	CN1507TC	7 channel temperature controller
	SSR330DC25	Solid state relay DC 25 amp
Swagelok	SS-HBVV51-C	Stainless steel high-pressure bellows-sealed valve, polyimide stem tip ¼ in. Female Swagelok VCR fitting
National Instruments	USB-9481	USB-based high-voltage relay output
Laminar Technologies		MFCs (rebuilt)
MDC	463000	Sealed-off glass tube (1 1/3" CF)
Process Materials	URS-100	MFC controller (surplus)
Strem Chemicals	82-2100	Bis(2,2,6,6-tetramethyl-3,5-heptanedionato)lead(II), 99% [Pb(TMHD)2], 5g
	40-5000	Tetrakis(2,2,6,6-tetramethyl-3,5-heptanedionato)zirconium(IV), 99% [Zr(TMHD)4], 5g
Sigma Aldrich	494143	$TiC_{28}H_{52}O_6$ (99.99%), Titanium(IV) diisopropoxidebis (2,2,6,6-tetramethyl-3,5-heptanedionate), 5g
Thermal Ceramics	Superwool 607	Insulation blanket for reactors

Vendor	Service
Machine shop	Stands for ALD reactor
MEMS Exchange	Platinized silicon substrates

Collaborator	Company/school	Project
Kang Wang	UCLA	Shadow mask for device fabrication (contact: Kin Wong) VCMA and TMR Characterization for MTJs (contact: Xiang Li)
Sarah Tolbert	UCLA	Mesoporous CFO or PZT (contact: Abraham Buditama)
Susan Trolier-McKinstry	Penn State	e_{31} measurement for PZT/Pt samples

C.1 Baseline of Platinized Silicon Substrates

Platinized silicon substrates were ordered from MEMS and Nanotechnology Exchange. They consisted (from the top down) of 100 nm of sputter-deposited Pt, 20 to 35 nm of sputter-deposited (and furnace annealed) TiO_2, and 500 nm of thermally oxidized SiO_2 on a Si substrate.

The <100>-oriented Si substrate was 150 mm in diameter and approximately 650 um thick. The TiO_2 was <200>-oriented, leaving the Pt layer <111>-oriented with a <111> rocking curve FWHM of less than 5˚ using Cu Kα radiation.

C.2 BFO/PMN-PT for TANMS 1-D Memory Thrust

An opportunity for collaboration exists with Yimei Zhu at Brookhaven National Laboratory for a small group of students to go and perform an in-situ TEM investigation of PMN-PT/BFO composites in a magnetic tunnel junction structure. Measurements could be taken during an applied voltage pulse to observe the strain induced in the junctions. Even more interesting would be to combine this with Lorentz TEM measurements to characterize the magnetization effects induced in the adjacent BFO layer.

BIBLIOGRAPHY

Ahmed, R. and R. H. Victora (2015). "Possible Explanation for Observed Effectiveness of Voltage-Controlled Anisotropy in CoFeB/MgO MTJ." IEEE Transactions on Magnetics **51**(11): 1-4.

Aimon, N. M., H. K. Choi, et al. (2014). "Templated Self-Assembly of Functional Oxide Nanocomposites." Advanced Materials **26**(19): 3063-3067.

Alzate, J. G. (2014). "Voltage-Controlled Magnetic Dynamics in Nanoscale Magnetic Tunnel Junctions." PhD Thesis, University of California, Los Angeles **Electrical Engineering**.

Alzate, J. G., P. K. Amiri, et al. (2012). Voltage-induced switching of nanoscale magnetic tunnel junctions. Electron Devices Meeting (IEDM), 2012 IEEE International.

Alzate, J. G., P. K. Amiri, et al. (2014). "Temperature dependence of the voltage-controlled perpendicular anisotropy in nanoscale MgO vertical bar CoFeB vertical bar Ta magnetic tunnel junctions." Applied Physics Letters **104**(11).

Alzate, J. G., P. Khalili Amiri, et al. (2014). "Temperature dependence of the voltage-controlled perpendicular anisotropy in nanoscale MgO|CoFeB|Ta magnetic tunnel junctions." Applied Physics Letters **104**(11): 112410.

Arblaster, J. W. (2006). "Crystallographic Properties of Platinum NEW METHODOLOGY AND ERRATUM." Platinum Metals Review **50**(3): 118-119.

Astrov, D. N. (1961). "Magnetoelectric Effect in Chromium Oxide." Soviet Physics Jetp-Ussr **13**(4): 729-733.

AVNET. (1999). "Storage Hierarchy." from http://www.ts.avnet.com/uk/products_and_solutions/storage/hierarchy.html.

Bastani, Y., T. Schmitz-Kempen, et al. (2011). "Critical thickness for extrinsic contributions to the dielectric and piezoelectric response in lead zirconate titanate ultrathin films." Journal of Applied Physics **109**(1).

Bharadwaja, S. S. N., F. Griggio, et al. (2011). "Highly textured laser annealed Pb(Zr0.52Ti0.48)O-3 thin films." Applied Physics Letters **99**(4).

Bibes, M., J. E. Villegas, et al. (2011). "Ultrathin oxide films and interfaces for electronics and spintronics." Advances in Physics **60**(1): 5-84.

Brezesinski, T., M. Groenewolt, et al. (2006). "Evaporation-induced self-assembly (EISA) at its limit: Ultrathin, crystalline patterns by templating of micellar monolayers." Advanced Materials **18**(17): 2260-+.

Brinker, C. J., Y. F. Lu, et al. (1999). "Evaporation-induced self-assembly: Nanostructures made easy." Advanced Materials **11**(7): 579-+.

Cattan, E., T. Haccart, et al. (1999). "e(31) piezoelectric constant measurement of lead zirconate titanate thin films." Journal of Applied Physics **86**(12): 7017-7023.

Chen, H. D., K. R. Udayakumar, et al. (1996). "Fabrication and electrical properties of lead zirconate titanate thick films." Journal of the American Ceramic Society **79**(8): 2189-2192.

Chen, W., W. G. Zhu, et al. (2010). "Enhanced Ferroelectric and Dielectric Properties of CoFe2O4-Pb(Zr0.53Ti0.47)O-3 Multiferroic Composite Thick Films." Journal of the American Ceramic Society **93**(3): 796-799.

Choi, J. H., F. Zhang, et al. (2013). "Tailoring the composition of lead zirconate titanate by atomic layer deposition." Journal of Vacuum Science & Technology B **31**(1): 1-7.

Choi, J. H., F. Zhang, et al. (2013). "Tailoring the composition of lead zirconate titanate by atomic layer deposition." Journal of Vacuum Science & Technology B **31**(1).

Crowell, J. E. (2003). "Chemical methods of thin film deposition: Chemical vapor deposition, atomic layer deposition, and related technologies." Journal of Vacuum Science & Technology A **21**(5): S88-S95.

Cullity, B. D. and C. D. Graham (2009). Introduction to magnetic materials. Hoboken, N.J., IEEE/Wiley.

Cullity, B. D. and S. R. Stock (2001). Elements of x-ray diffraction. Upper Saddle River, NJ, Prentice Hall.

Damjanovic, D. (1998). "Ferroelectric, dielectric and piezoelectric properties of ferroelectric thin films and ceramics." Reports on Progress in Physics **61**(9): 1267-1324.

Ding, L. Y., F. X. Wu, et al. (2011). "Controllable microstructures and multiferroic properties of Pb(Zr0.53Ti0.47)O-3-CoFe2O4 composite films." Applied Surface Science **257**(9): 3840-3842.

Dorrance, R., J. G. Alzate, et al. (2013). "Diode-MTJ Crossbar Memory Cell Using Voltage-Induced Unipolar Switching for High-Density MRAM." Ieee Electron Device Letters **34**(6): 753-755.

Eerenstein, W., N. D. Mathur, et al. (2006). "Multiferroic and magnetoelectric materials." Nature **442**(7104): 759-765.

Endo, M., S. Kanai, et al. (2010). "Electric-field effects on thickness dependent magnetic anisotropy of sputtered MgO/Co40Fe40B20/Ta structures." Applied Physics Letters **96**(21).

Endo, M., S. Kanai, et al. (2010). "Electric-field effects on thickness dependent magnetic anisotropy of sputtered MgO/Co[sub 40]Fe[sub 40]B[sub 20]/Ta structures." Applied Physics Letters **96**(21): 212503.

Eom, C. B. and S. Trolier-McKinstry (2012). "Thin-film piezoelectric MEMS." MRS Bulletin **37**(11): 1007-1017.

Fattakhova-Rohfing, D., T. Brezesinski, et al. (2006). "Transparent conducting films of indium tin oxide with 3D mesopore architecture." Advanced Materials **18**(22): 2980-+.

Fiebig, M. (2005). "Revival of the magnetoelectric effect." Journal of Physics D-Applied Physics **38**(8): R123-R152.

Fink, M. (2014). "The End of a Necessary Evil: Collapsing the Memory Hierarchy." hp next, from http://www8.hp.com/hpnext/posts/end-necessary-evil-collapsing-memory-hierarchy#.VhqiKxHBzRY.

Foster, C. M., G. R. Bai, et al. (1997). "Single-crystal Pb(ZrxTi1-x)O-3 thin films prepared by metal-organic chemical vapor deposition: Systematic compositional variation of electronic and optical properties." Journal of Applied Physics **81**(5): 2349-2357.

Garcia, V., M. Bibes, et al. (2010). "Ferroelectric Control of Spin Polarization." Science **327**(5969): 1106-1110.

George, S. M. (2010). "Atomic Layer Deposition: An Overview." Chemical Reviews **110**(1): 111-131.

Gerber, P., U. Bottger, et al. (2006). "Composition influences on the electrical and electromechanical properties of lead zirconate titanate thin films." Journal of Applied Physics **100**(12).

Ghandhi, S. K. (1994). VLSI fabrication principles : silicon and gallium arsenide. New York, Wiley.

Gruska, B. and K. Hinrichs (2011). UV-VIS-IR Ellipsometry (ELL). Surface and Thin Film Analysis, Wiley-VCH Verlag GmbH & Co. KGaA**:** 393-405.

Guo, R., L. E. Cross, et al. (2000). "Origin of the high piezoelectric response in PbZr1-xTixO3." Physical Review Letters **84**(23): 5423-5426.

Gupta, V. and A. Mansingh (1998). Breakdown mechanism in insulating zinc oxide film. Applications of Ferroelectrics, 1998. ISAF 98. Proceedings of the Eleventh IEEE International Symposium on.

Hassen, E. M. J., B. Viala, et al. (2012). "Room temperature magnetoresistance in CoFeB/SrTiO3/CoFeB magnetic tunnel junctions deposited by ion beam sputtering." Journal of Applied Physics **111**(7): 07C727.

He, H. C., J. Ma, et al. (2009). "Enhanced magnetoelectric properties in Pb(Zr,Ti)O-3-CoFe2O4 layered thin films with LaNiO3 as a buffer layer." Journal of Physics D-Applied Physics **42**(9).

He, K. H., J. S. Chen, et al. (2011). "First principles study of the electric field effect on magnetization and magnetic anisotropy of FeCo/MgO(001) thin film." Applied Physics Letters **99**(7).

Hennessy, J. L., D. A. Patterson, et al. (2003). Computer architecture a quantitative approach. San Francisco, CA, Morgan Kaufmann.

Hill, N. A. (2000). "Why are there so few magnetic ferroelectrics?" Journal of Physical Chemistry B **104**(29): 6694-6709.

Horiuchi, S. and Y. Tokura (2008). "Organic ferroelectrics." Nature Materials **7**(5): 357-366.

Hur, N., S. Park, et al. (2004). "Electric polarization reversal and memory in a multiferroic material induced by magnetic fields." Nature **429**(6990): 392-395.

Hwang, H. Y., Y. Iwasa, et al. (2012). "Emergent phenomena at oxide interfaces." Nature Materials **11**(2): 103-113.

Ikeda, S., K. Miura, et al. (2010). "A perpendicular-anisotropy CoFeB-MgO magnetic tunnel junction." Nat Mater **9**(9): 721-724.

Izyumskaya, N., Y. Alivov, et al. (2007). "Processing, structure, properties, and applications of PZT thin films." Critical Reviews in Solid State and Materials Sciences **32**(3-4): 111-202.

Jaffe, B., W. R. Cook, et al. (1971). Piezoelectric ceramics. London, New York,, Academic Press.

Jaffe, B., R. S. Roth, et al. (1955). "Properties of Piezoelectric Ceramics in the Solid-Solution Series Lead Titanate-Lead Zirconate-Lead Oxide - Tin Oxide and Lead Titanate-Lead Hafnate." Journal of Research of the National Bureau of Standards **55**(5): 239-254.

Jona, F., G. Shirane, et al. (1957). "X-Ray and Neutron Diffraction Study of Antiferroelectric Lead Zirconate, Pbzro3." Physical Review **105**(3): 849-856.

Jordan, T. L., Z. Ounaies, et al. (2001). Piezoelectric Ceramics Characterization. Ft. Belvoir, Defense Technical Information Center**:** 25 p.

Kalinin, S. V., N. Setter, et al. (2009). "Electromechanics on the Nanometer Scale: Emerging Phenomena, Devices, and Applications." Mrs Bulletin **34**(9): 634-642.

Kalpat, S. and K. Uchino (2001). "Highly oriented lead zirconium titanate thin films: Growth, control of texture, and its effect on dielectric properties." Journal of Applied Physics **90**(6): 2703-2710.

Kanai, S., M. Yamanouchi, et al. (2012). "Electric field-induced magnetization reversal in a perpendicular-anisotropy CoFeB-MgO magnetic tunnel junction." Applied Physics Letters **101**(12): 122403.

Karthik, S. V., Y. K. Takahashi, et al. (2012). "Transmission electron microscopy study on the effect of various capping layers on CoFeB/MgO/CoFeB pseudo spin valves annealed at different temperatures." Journal of Applied Physics **111**(8).

Khalili Amiri, P., J. Alzate, et al. (2015). "Electric-Field-Controlled Magnetoelectric Random Access Memory: Progress, Challenges, and Scaling." Magnetics, IEEE Transactions on **PP**(99): 1-1.

Khalili Amiri, P., Z. M. Zeng, et al. (2011). "Switching current reduction using perpendicular anisotropy in CoFeB–MgO magnetic tunnel junctions." Applied Physics Letters **98**(11): 112507.

Khalili, P. and K. L. Wang (2015). "The computer chip that never forgets." Spectrum, IEEE **52**(7): 30-56.

Kim, D. M., C. B. Eom, et al. (2006). "Thickness dependence of structural and piezoelectric properties of epitaxial Pb(Zr0.52Ti0.48)O-3 films on Si and SrTiO3 substrates." Applied Physics Letters **88**(14).

Kimura, T., T. Goto, et al. (2003). "Magnetic control of ferroelectric polarization." Nature **426**(6962): 55-58.

Kita, K., D. W. Abraham, et al. (2012). "Electric-field-control of magnetic anisotropy of Co0.6Fe0.2B0.2/oxide stacks using reduced voltage." Journal of Applied Physics **112**(3).

Kita, K., D. W. Abraham, et al. (2012). "Electric-field-control of magnetic anisotropy of Co0.6Fe0.2B0.2/oxide stacks using reduced voltage." Journal of Applied Physics **112**(3): 033919.

Kubota, H., S. Ishibashi, et al. (2012). "Enhancement of perpendicular magnetic anisotropy in FeB free layers using a thin MgO cap layer." Journal of Applied Physics **111**(7): 07C723.

Kumar, N., A. Yanguas-Gil, et al. (2008). "Growth Inhibition to Enhance Conformal Coverage in Thin Film Chemical Vapor Deposition." Journal of the American Chemical Society **130**(52): 17660-+.

Lawes, G. and G. Srinivasan (2011). "Introduction to magnetoelectric coupling and multiferroic films." Journal of Physics D-Applied Physics **44**(24).

Ledermann, N., P. Muralt, et al. (2003). "{100}-textured, piezoelectric Pb(Zr-x Ti1-x)O-3 thin films for MEMS: integration, deposition and properties." Sensors and Actuators a-Physical **105**(2): 162-170.

Lee, J. K., J. M. Ku, et al. (2002). "Metal-Organic Chemical Vapor Deposition of $Pb(Zr_xTi_{1-x})O_3$ Thin Films for High-Density Ferroelectric Random Access Memory Application." Journal of Semiconductor Technology and Science **2**(3): 205-212.

Lefki, K. and G. J. M. Dormans (1994). "Measurement of Piezoelectric Coefficients of Ferroelectric Thin-Films." Journal of Applied Physics **76**(3): 1764-1767.

Li, X., G. Yu, et al. (2015). "Thermally stable voltage-controlled perpendicular magnetic anisotropy in Mo|CoFeB|MgO structures." Applied Physics Letters **107**(14): 142403.

Liu, L., O. J. Lee, et al. (2012). "Current-Induced Switching of Perpendicularly Magnetized Magnetic Layers Using Spin Torque from the Spin Hall Effect." Physical Review Letters **109**(9).

Liu, L., C.-F. Pai, et al. (2012). "Magnetic Oscillations Driven by the Spin Hall Effect in 3-Terminal Magnetic Tunnel Junction Devices." Physical Review Letters **109**(18).

Liu, L., C. F. Pai, et al. (2012). "Magnetic oscillations driven by the spin Hall effect in 3-terminal magnetic tunnel junction devices." Phys Rev Lett **109**(18): 186602.

Liu, M., X. Li, et al. (2007). "A modified sol-gel process for multiferroic nanocomposite films." Journal of Applied Physics **102**(8).

Ltd., C. S. (2006). Peak Fitting in XPS. CasaXPS**:** 1-29.

Ma, Y. G., W. N. Cheng, et al. (2007). "Magnetoelectric effect in epitaxial Pb(Zr0.52Ti0.48)O-3/La0.7Sr0.3MnO3 composite thin film." Applied Physics Letters **90**(15).

Mamak, M., N. Coombs, et al. (2000). "Mesoporousyttria-zirconia and metal-yttria-zirconia solid solutions for fuel cells." Advanced Materials **12**(3): 198-+.

Mao, Y. B. (2012). "Facile molten-salt synthesis of double perovskite La2BMnO6 nanoparticles." Rsc Advances **2**(33): 12675-12678.

Mao, Y. B., J. Parsons, et al. (2013). "Magnetic properties of double perovskite La2BMnO6 (B = Ni or Co) nanoparticles." Nanoscale **5**(11): 4720-4728.

Maria, J. P., J. F. Shepard, et al. (2005). "Characterization of the piezoelectric properties of Pb0.98Ba0.02(Mg1/3Nb2/3)O-3-PbTiO3 epitaxial thin films." International Journal of Applied Ceramic Technology **2**(1): 51-58.

Martin, L., S. P. Crane, et al. (2008). "Multiferroics and magnetoelectrics: thin films and nanostructures." Journal of Physics-Condensed Matter **20**(43).

Martin, L. W., Y. H. Chu, et al. (2010). "Advances in the growth and characterization of magnetic, ferroelectric, and multiferroic oxide thin films." Materials Science & Engineering R-Reports **68**(4-6): Iii-133.

Maruyama, T., Y. Shiota, et al. (2009). "Large voltage-induced magnetic anisotropy change in a few atomic layers of iron." Nat Nanotechnol **4**(3): 158-161.

McElfresh, M. (1994) "Fundamentals of Magnetism and Magnetic Measurements Featuring Quantum Design's Magnetic Property Measurement System."

Mikolajick, T., C. Dehm, et al. (2001). "FeRAM technology for high density applications." Microelectronics Reliability **41**(7): 947-950.

Miron, I. M., K. Garello, et al. (2011). "Perpendicular switching of a single ferromagnetic layer induced by in-plane current injection." Nature **476**(7359): 189-193.

Miyajima, T., T. Ibusuki, et al. (2009). "Transmission electron microscopy study on the crystallization and boron distribution of CoFeB/MgO/CoFeB magnetic tunnel junctions with various capping layers." Applied Physics Letters **94**(12).

Moazzami, R., H. Chenming, et al. (1992). "Electrical characteristics of ferroelectric PZT thin films for DRAM applications." Electron Devices, IEEE Transactions on **39**(9): 2044-2049.

Muralt, P. (1997). "Piezoelectric thin films for MEMS." Integrated Ferroelectrics **17**(1-4): 297-307.

Muralt, P. (2000). "Ferroelectric thin films for micro-sensors and actuators: a review." Journal of Micromechanics and Microengineering **10**(2): 136-146.

Muralt, P. (2000). "PZT thin films for microsensors and actuators: Where do we stand?" Ieee Transactions on Ultrasonics Ferroelectrics and Frequency Control **47**(4): 903-915.

Muralt, P., M. A. Dubois, et al. (1999). "In-plane piezoelectric coefficient of PZT thin films as a function of composition." Ferroelectrics **224**(1-4): 663-670.

Muralt, P., T. Maeder, et al. (1998). "Texture control of PbTiO3 and Pb(Zr,Ti)O-3 thin films with TiO2 seeding." Journal of Applied Physics **83**(7): 3835-3841.

Muralt, P., R. G. Polcawich, et al. (2009). "Piezoelectric Thin Films for Sensors, Actuators, and Energy Harvesting." Mrs Bulletin **34**(9): 658-664.

Myers, E. B., D. C. Ralph, et al. (1999). "Current-induced switching of domains in magnetic multilayer devices." Science **285**(5429): 867-870.

Nan, C. W., M. I. Bichurin, et al. (2008). "Multiferroic magnetoelectric composites: Historical perspective, status, and future directions." Journal of Applied Physics **103**(3).

Nelmes, R. J. and W. F. Kuhs (1985). "The Crystal-Structure of Tetragonal Pbtio3 at Room-Temperature and at 700 K." Solid State Communications **54**(8): 721-723.

Nguyen, M. D., H. Nazeer, et al. (2010). "Characterization of epitaxial Pb(Zr, Ti)O(3) thin films deposited by pulsed laser deposition on silicon cantilevers." Journal of Micromechanics and Microengineering **20**(8).

Niranjan, M. K., C.-G. Duan, et al. (2010). "Electric field effect on magnetization at the Fe/MgO(001) interface." Applied Physics Letters **96**(22): 222504.

Noheda, B., D. E. Cox, et al. (1999). "A monoclinic ferroelectric phase in the Pb(Zr1-xTix)O-3 solid solution." Applied Physics Letters **74**(14): 2059-2061.

Noheda, B., J. A. Gonzalo, et al. (2000). "Tetragonal-to-monoclinic phase transition in a ferroelectric perovskite: The structure of PbZr0.52Ti0.48O3." Physical Review B **61**(13): 8687-8695.

O'Handley, R. C. (2000). Modern magnetic materials : principles and applications. New York, Wiley.

Oakberg, T. C. (2010) "Magneto-Optic Kerr Effect."

Ogawa, M. (1994). "Formation of Novel Oriented Transparent Films of Layered Silica-Surfactant Nanocomposites." Journal of the American Chemical Society **116**(17): 7941-7942.

Okada, A., S. Kanai, et al. (2014). "Electric-field effects on magnetic anisotropy and damping constant in Ta/CoFeB/MgO investigated by ferromagnetic resonance." Applied Physics Letters **105**(5).

Okada, A., S. Kanai, et al. (2014). "Electric-field effects on magnetic anisotropy and damping constant in Ta/CoFeB/MgO investigated by ferromagnetic resonance." Applied Physics Letters **105**(5): 052415.

Ong, P. V., N. Kioussis, et al. (2015). "Giant voltage modulation of magnetic anisotropy in strained heavy metal/magnet/insulator heterostructures." Physical Review B **92**(2): 020407.

Ortega, N., P. Bhattacharya, et al. (2006). "Multiferroic properties of Pb(Zr,Ti)O-3/CoFe2O4 composite thin films." Journal of Applied Physics **100**(12).

Pantel, D., S. Goetze, et al. (2012). "Reversible electrical switching of spin polarization in multiferroic tunnel junctions." Nat Mater **11**(4): 289-293.

Potrepka, D., G. R. Fox, et al. (2011). "Pt/TiO_2 Growth Templates for Enhanced PZT films and MEMS Devices " Material Research Society Symposium Proceedings **1299**: 67-72.

Proksch, R. and S. V. Kalinin "Piezoresponse Force Microscopy with Asylum Research AFMs."

Prume, K., P. Muralt, et al. (2007). "Piezoelectric thin films: Evaluation of electrical and electromechanical characteristics for MEMS devices." Ieee Transactions on Ultrasonics Ferroelectrics and Frequency Control **54**(1): 8-14.

Pulskamp, J. S., R. G. Polcawich, et al. (2012). "Piezoelectric PZT MEMS technologies for small-scale robotics and RF applications." MRS Bulletin **37**(11): 1062-1070.

Puurunen, R. L. (2005). "Surface chemistry of atomic layer deposition: A case study for the trimethylaluminum/water process." Journal of Applied Physics **97**(12).

Qiu, Z. Q. and S. D. Bader (2000). "Surface magneto-optic Kerr effect." Review of Scientific Instruments **71**(3): 1243-1255.

Quickel, T. E., V. H. Le, et al. (2010). "On the Correlation between Nanoscale Structure and Magnetic Properties in Ordered Mesoporous Cobalt Ferrite (CoFe2O4) Thin Films." Nano Letters **10**(8): 2982-2988.

Quickel, T. E., L. T. Schelhas, et al. (2015). "Mesoporous bismuth ferrite with amplified magnetoelectric coupling and electric field-induced ferrimagnetism." Nature Communications **6**.

Rajanikanth, A., T. Hauet, et al. (2013). "Magnetic anisotropy modified by electric field in V/Fe/MgO(001)/Fe epitaxial magnetic tunnel junction." Applied Physics Letters **103**(6): 062402.

Ramesh, R. and N. A. Spaldin (2007). "Multiferroics: progress and prospects in thin films." Nature Materials **6**(1): 21-29.

Robertson, J. (2004). "High dielectric constant oxides." The European Physical Journal Applied Physics **28**(3): 265-291.

Ryu, H., P. Murugavel, et al. (2006). "Magnetoelectric effects of nanoparticulate Pb(Zr0.52Ti0.48)O3–NiFe2O4 composite films." Applied Physics Letters **89**(10): 102907.

Ryu, H., P. Murugavel, et al. (2006). "Magnetoelectric effects of nanoparticulate Pb(Zr0.52Ti0.48)O-3-NiFe2O4 composite films." Applied Physics Letters **89**(10).

Ryu, S., J. H. Park, et al. (2007). "Magnetoelectric coupling of [00l]-oriented Pb(Zr0.4Ti0.6)O-3-Ni0.8Zn0.2Fe2O4 multilayered thin films." Applied Physics Letters **91**(14).

Sakata, M., S. Wakabayashi, et al. (1996). "Sputtered High d_{31} Coefficient PZT Thin Film for Micro Actuators." IEEE: 263-266.

Sanchez, L. M., D. M. Potrepka, et al. (2011). "Improving PZT Thin Film Texture Through Pt Metallization and Seed Layers." Materials Research Society Symp. Proc. **1299**: 53-58.

Schmid, H. (1994). Multi-ferroic magnetoelectrics.

Shen, W., D. Mazumdar, et al. (2006). "Effect of film roughness in MgO-based magnetic tunnel junctions." Applied Physics Letters **88**(18): 182508.

Shepard, J. F., P. J. Moses, et al. (1998). "The wafer flexure technique for the determination of the transverse piezoelectric coefficient (d(31)) of PZT thin films." Sensors and Actuators a-Physical **71**(1-2): 133-138.

Shiota, Y., F. Bonell, et al. (2013). "Opposite signs of voltage-induced perpendicular magnetic anisotropy change in CoFeB vertical bar MgO junctions with different underlayers." Applied Physics Letters **103**(8).

Shiota, Y., F. d. r. Bonell, et al. (2013). "Opposite signs of voltage-induced perpendicular magnetic anisotropy change in CoFeB|MgO junctions with different underlayers." Applied Physics Letters **103**(8): 082410.

Shiota, Y., S. Murakami, et al. (2011). "Quantitative Evaluation of Voltage-Induced Magnetic Anisotropy Change by Magnetoresistance Measurement." Applied Physics Express **4**(4).

Shiota, Y., T. Nozaki, et al. (2012). "Induction of coherent magnetization switching in a few atomic layers of FeCo using voltage pulses." Nat Mater **11**(1): 39-43.

Skowroński, W., T. Nozaki, et al. (2015). "Underlayer material influence on electric-field controlled perpendicular magnetic anisotropy in CoFeB/MgO magnetic tunnel junctions." Physical Review B **91**(18): 184410.

Skowroński, W., T. Nozaki, et al. (2015). "Perpendicular magnetic anisotropy of Ir/CoFeB/MgO trilayer system tuned by electric fields." Applied Physics Express **8**(5): 053003.

Slonczewski, J. C. (1989). "Conductance and Exchange Coupling of 2 Ferromagnets Separated by a Tunneling Barrier." Physical Review B **39**(10): 6995-7002.

Slonczewski, J. C. (1996). "Current-driven excitation of magnetic multilayers." Journal of Magnetism and Magnetic Materials **159**(1-2): L1-L7.

Smith, G. L., J. S. Pulskamp, et al. (2012). "PZT-Based Piezoelectric MEMS Technology." Journal of the American Ceramic Society **95**(6): 1777-1792.

Spaldin, N. A. (2003). Magnetic Materials: Fundamentals and Device Applications, Cambridge University Press.

Spaldin, N. A. and M. Fiebig (2005). "The renaissance of magnetoelectric multiferroics." Science **309**(5733): 391-392.

Szepieniec, J. M. (2012). Self-Assembled Vertical Nanostructured Composites.

Tahmasebi, K., A. Barzegar, et al. (2013). "Multiferroic thin film composite of Pb(Zr0.95Ti0.05)O-3/CoFe2O4 on Si and SrTiO3 substrates." Thin Solid Films **537**: 76-79.

Tang, D. D. and Y. J. Lee (2010). Magnetic Memory: Fundamentals and Technology, Cambridge University Press.

TANMS, C. f. T. A. o. N. M. S. (2014). "TANMS, Center for Translational Applications of Nanoscale Multiferroic Systems." from http://www.tanms-erc.org/.

Trolier-McKinstry, S. (2008). Improved Thin Film Piezoelectrics for Actuator Applications. Ft. Belvoir, Defense Technical Information Center**:** 14 p.

Trolier-McKinstry, S. and P. Muralt (2004). "Thin film piezoelectrics for MEMS." Journal of Electroceramics **12**(1-2): 7-17.

Tsubouchi, K. and N. Mikoshiba (1985). "Zero-Temperature-Coefficient Saw Devices on Aln Epitaxial-Films." Ieee Transactions on Sonics and Ultrasonics **32**(5): 634-644.

Vaz, C. A. F., J. Hoffman, et al. (2010). "Magnetoelectric Coupling Effects in Multiferroic Complex Oxide Composite Structures." Advanced Materials **22**(26-27): 2900-2918.

Wan, J. G., X. W. Wang, et al. (2005). "Magnetoelectric CoFe2O4-Pb(Zr,Ti)O-3 composite thin films derived by a sol-gel process." Applied Physics Letters **86**(12).

Wan, J. G., H. Zhang, et al. (2006). "Magnetoelectric CoFe2O4-lead zirconate titanate thick films prepared by a polyvinylpyrrolidone-assisted sol-gel method." Applied Physics Letters **89**(12).

Wang, J., J. B. Neaton, et al. (2003). "Epitaxial BiFeO3 multiferroic thin film heterostructures." Science **299**(5613): 1719-1722.

Wang, K. L., J. G. Alzate, et al. (2013). "Low-power non-volatile spintronic memory: STT-RAM and beyond." Journal of Physics D: Applied Physics **46**(7): 074003.

WANG, K. L. and P. K. AMIRI (2012). "VOLTAGE-CONTROLLED MAGNETIC ANISOTROPY IN SPINTRONIC DEVICES." SPIN **02**(03): 1240002.

Wang, W. G., M. Li, et al. (2012). "Electric-field-assisted switching in magnetic tunnel junctions." Nat Mater **11**(1): 64-68.

Wang, Y., J. M. Hu, et al. (2010). "Multiferroic magnetoelectric composite nanostructures." Npg Asia Materials **2**(2): 61-68.

Watanabe, T., S. Hoffmann-Eifert, et al. (2008). "Growth behavior of atomic-layer-deposited Pb(Zr, Ti)O(x) thin films on planar substrate and three-dimensional hole structures." Journal of the Electrochemical Society **155**(11): D715-D722.

Watanabe, T., S. Hoffmann-Eifert, et al. (2007). "Growth of ternary PbTiOx films in a combination of binary oxide atomic layer depositions." Journal of Applied Physics **101**(1).

Wilke, R. H. T., P. J. Moses, et al. (2012). "Wafer mapping of the transverse piezoelectric coefficient, e(31,f), using the wafer flexure technique with sputter deposited Pt strain gauges." Sensors and Actuators a-Physical **173**(1): 152-157.

Wolf, R. A. and S. Trolier-McKinstry (2004). "Temperature dependence of the piezoelectric response in lead zirconate titanate films." Journal of Applied Physics **95**(3): 1397-1406.

Woollam Co., J. A., Inc. "Guide to Using WVASE32^{TM}."

Wu, T., M. A. Zurbuchen, et al. (2006). "Observation of magnetoelectric effect in epitaxial ferroelectric film/manganite crystal heterostructures." Physical Review B **73**(13).

Yamazaki, H., T. Tsuyama, et al. (1992). "Preparation of Pb(Zr, Ti)O3 Thin-Films Using All Dipivaloylmethane Source Materials by Metalorganic Chemical Vapor-Deposition." Japanese Journal of Applied Physics Part 1-Regular Papers Short Notes & Review Papers **31**(9B): 2995-2997.

Yang, H. X., M. Chshiev, et al. (2011). "First-principles investigation of the very large perpendicular magnetic anisotropy at Fe vertical bar MgO and Co vertical bar MgO interfaces." Physical Review B **84**(5).

Yang, P. D., T. Deng, et al. (1998). "Hierarchically ordered oxides." Science **282**(5397): 2244-2246.

Yang, S., H. X. Bao, et al. (2010). "Large Magnetostriction from Morphotropic Phase Boundary in Ferromagnets." Physical Review Letters **104**(19).

Yokota, H., N. Zhang, et al. (2009). "Crystal structure of the rhombohedral phase of PbZr(1-x)Ti(x)O(3) ceramics at room temperature." Physical Review B **80**(10).

Zhang, F., Y. C. Perng, et al. (2011). "Atomic layer deposition of Pb(Zr,Ti)O-x on 4H-SiC for metal-ferroelectric-insulator-semiconductor diodes." Journal of Applied Physics **109**(12).

Zhang, F., Y. C. Perng, et al. (2011). "Atomic layer deposition of Pb(Zr,Ti)O(x) on 4H-SiC for metal-ferroelectric-insulator-semiconductor diodes." Journal of Applied Physics **109**(12).

Zhang, J. X., J. Y. Dai, et al. (2010). "Interfacial engineering and coupling of electric and magnetic properties in Pb(Zr0.53Ti0.47)O-3/CoFe2O4 multiferroic epitaxial multilayers." Journal of Applied Physics **107**(10).

Zhang, S. J., R. Xia, et al. (2007). "Lead-free piezoelectric ceramics vs. PZT?" Journal of Electroceramics **19**(4): 251-257.

Zheng, H., J. Wang, et al. (2004). "Multiferroic BaTiO3-CoFe2O4 nanostructures." Science **303**(5658): 661-663.

Zhong, X. L., J. B. Wang, et al. (2007). "Multiferroic nanoparticulate Bi3.15Nd0.85Ti3O12–CoFe2O4 composite thin films prepared by a chemical solution deposition technique." Applied Physics Letters **90**(15): 152903.

Zhu, J., J. A. Katine, et al. (2012). "Voltage-Induced Ferromagnetic Resonance in Magnetic Tunnel Junctions." Physical Review Letters **108**(19): 197203.

Zhu, J., J. A. Katine, et al. (2012). "Voltage-Induced Ferromagnetic Resonance in Magnetic Tunnel Junctions." Physical Review Letters **108**(19).